TECHNISCHE UNIVERSITÄT WIEN
Vienna | Austria

PhD Thesis

# Dielectric Material Characterization for Inhomogeneous Transmission Lines up to 110 GHz

unter der Leitung von

em. O.Univ.-Prof. Dipl.-Ing. Dr.techn. Gottfried Magerl
Institute of Electrodynamics, Microwave, and Circuit Engineering
TU Wien, Austria

eingereicht an der Technischen Universität Wien
Fakultät für Elektrotechnik und Informationstechnik

von

Dipl.-Ing. Oliver Huber, BSc
Matr.Nr. 0526803
Gassergasse 2-8/1/15
1050 Wien, Austria

Vienna, September 2018 ______________________________

# KURZFASSUNG

Verschiedenste elektronische Geräte sind in unserem Tagesablauf nicht mehr wegzudenken. Obwohl die Anwendungen sehr vielfältig sind, haben kleine Gadgets bis hin zu komplexen Smartphones eines gemeinsam: die Leiterplatte. Mikrochips werden auf der Leiterplatte angeordnet und miteinander verbunden, um die gewünschte Aufgabe auszuführen. Im aktuellen Stand der Technik sind die Signale, mit denen die Mikrochips kommunizieren, nicht mehr im Kilohertz-Bereich, sondern bereits im zweistelligen Gigahertz-Bereich angelangt. Für Mikrochip zu Mikrochip Übertragungen bei diesen Frequenzen ist es essentiell, sich auf verlässliche Materialparameter für das verwendete Leiterplattenmaterial zu stützen. Für dielektrische Materialien sind die relative Permittivität (auch Dielektrizitätskonstante $Dk$) und der Verlustfaktor (oder Tangens des Verlustwinkels $LT$) von herausragender Bedeutung. Sobald Impedanzen im Schaltungsdesign aufeinander abgestimmt werden müssen, spielt $Dk$ eine wichtige Rolle. Beispiele für Applikationen in denen Impedanzanpassung einen hohen Stellenwert einnimmt, sind Anpassnetzwerke für Leistungsverstärker und Antennen, als auch Digitalübertragungen mit hohen Datenraten. Jegliche Fehlanpassung führt zu ungewollter Reflexion von Energie die daraufhin nicht mehr für die gewünschte Anwendung zur Verfügung steht. Dielektrische Verluste werden mittels $LT$ quantifiziert. In dieser Dissertation wird dafür ein leicht anzuwendendes Verfahren vorgestellt, um die weitläufig verbreiteten Übertragungsleitungen, die Streifenleitung (MS) und die Koplanarleitung mit Massefläche (CBCPW), zur dielektrischen Charakterisierung bis zu 110 GHz zu verwenden.

Der vorgestellte Charakterisierungsprozess berücksichtigt und beseitigt viele Effekte die in diesem sehr weit gefassten Frequenzbereich auftreten. Bei den vermessenen Teststrukturen wurde speziell bei Frequenzen bis ca. 20 GHz ein signifikanter Einfluss des Skin-Effekts beobachtet. Für Frequenzen über 20 GHz ist der Einfluss von Oberflächenwellen zu berücksichtigen. Obwohl beide Effekte in einem nicht-trivialen Zusammenhang mit den Messergebnissen stehen, konnten trotzdem im Zuge des Charakterisierungsprozesses einfach anzuwendende analytische Formeln vorgestellt werden, die diese Effekte berücksichtigten. MS und CBCPW sind sehr weit verbreitete Übertragungsleitungen die nun auch mit der

vorgestellten Methode zur Materialcharakterisierung bis zu 110 GHz verwendet werden können.

Spezieller Fokus wird auch auf die Unsicherheiten gelegt, die bei der Anwendung der vorgestellten Methode zu berücksichtigen sind. Die Analyse der Unsicherheiten wird mittels Monte-Carlo-Simulation mit jeweils 25000 Durchläufen pro Analyse durchgeführt. In der Simulation werden die Ergebnisse auf den Einfluss von drei Unsicherheitsquellen untersucht: das Messequipment, die Herstellungstoleranzen und den Versatz der Sonden beim Kontaktieren der Strukturen.

Im letzten Kapitel der Arbeit wird die vorgestellte Methode auf zwei Substratmaterialien angewendet (Panasonic Megtron 6 und Pyralux TK), wobei die Ergebnisse sowohl mit Datenblattwerten als auch mit Resultaten von zwei separat durchgeführten Messmethoden verglichen werden. Die alternativen Vergleichsmethoden sind eine auf Resonanz basierende Methode mittels Ringresonatoren und eine nicht resonante Methode mit Substrate Integrated Waveguides (SIW). Die Resultate des vorgestellten Charakterisierungsprozesses liegen bei einer maximalen Abweichung von 2% für Pyralux TK und 0.6% für Megtron 6 im Vergleich mit den sehr frequenzlimitierten Datenblattwerten der Hersteller.

# ABSTRACT

Electronic equipment has nowadays an omnipresent status in everyday life. From little gadgets to more complex systems like a smartphone, they all have one common denominator: the printed circuit board (PCB). On a PCB all the utilized microchips are placed and interconnected to each other to fulfill the designated task. In a state-of-the-art PCB, these microchips are not communicating with frequencies of a few kilohertz anymore, they already operate with up to double digit gigahertz frequencies. For inter-chip communication with frequencies in that range, it is crucial to have reliable data for the used substrate material. For dielectric materials the relative permittivity (or dielectric constant $Dk$) and the dissipation factor (or loss tangent $LT$) play an important role. The $Dk$ is crucial for applications when wave impedances have to be matched. Prominent examples are matching circuits for power amplifiers or antennas, as well as high-speed digital communication systems. A mismatch in impedance causes energy to be reflected, and therefore being unavailable for the desired application. The $LT$ provides information about the dielectric losses that occur by using the selected material. Within this thesis, a straight forward method is introduced for transmission lines with inhomogeneous stack-ups, i.e. microstrip (MS) and conductor-backed coplanar waveguide (CBCPW), to be used for dielectric characterization up to 110 GHz.

The characterization method tackles many effects occurring due to the increased frequency range. For the investigated structures, the skin effect had a significant impact for frequencies up to approximately 20 GHz. For frequencies above 20 GHz, plane-trapped surface waves were affecting the results. Although both effects have a non-trivial relation to the measurements, the proposed method introduces analytic formulas which can be easily computed and integrated in computer-aided design (CAD). The main benefit of this characterization method is that MS and CBCPW are already widely used transmission lines and by using the proposed method these lines can serve also for reliable characterization of the substrate material for future applications.

Special focus is also laid on the overall uncertainties of the introduced method. The investigation is carried out with Monte Carlo simulations with 25000 runs

each. Within the simulations three sources of uncertainty are investigated: the measurement equipment, the manufacturing tolerances, and the probing offsets. All of them contribute their share to the overall uncertainty involved with the proposed method.

In the last chapter of the thesis, the determined dielectric constant of two substrate materials (Panasonic Megtron 6 and Pyralux TK) is compared with data sheet values and with two additional characterization methods. The additional methods are a resonant-method based on ring resonators, and a non-resonant method utilizing substrate integrated waveguides (SIWs). The results for the proposed method lie within a maximum deviation of 2% for Pyralux TK and 0.6% for Megtron 6 when compared with the frequency-limited data provided in the manufacturer's data sheets.

# CONTENTS

# Chapter 1

# Motivation

How a material reacts when exposed to electromagnetic fields is closely related to the response of free and bound electrons to the applied electric field and the response of atomic moments to the magnetic field [1]. Knowing how materials behave when exposed to electromagnetic fields aids in a meaningful selection of materials for specific tasks and applications. As this represents an extremely broad research area, the focus of this thesis narrows down to dielectric material characterization.

The range of applications for dielectric materials is still vast, so the focus is further narrowed to dielectric materials utilized for printed circuit boards (PCB). In the twenty-first century, PCBs are omnipresent, as they are utilized in basically every electronic equipment that has moderate complexity. The market for consumer electronics is expanding and the applications are getting more versatile. Electronic equipment started with simple direct current (DC) applications with some infrequent and slow switching cycles. Now applications have already reached the upper two-digit gigahertz range (e.g. automotive radar). Data rates are increasing in a continuous manner. So not only for a few selected frequencies, but rather for a continuous frequency range an accurate broadband dielectric characterization gains importance. This raises many questions which materials can keep up with these high requirements, and the knowledge about the dielectric properties of PCB materials over a wide frequency range is crucial.

Within this thesis the dielectric properties are investigated up to 110 GHz for two different PCB materials. Different characterization methods are evaluated and their results are compared. It should be emphasized already at this point that the focus lies not only on the eventual dielectric constant ($Dk$) of the investigated substrate material, but also on wave propagation effects that may impair accurate measurements of $Dk$ with the proposed methods (see Cha. 2).

(a) (b)

Figure 1.1: Precursors of PCBs: (a) 1920s wall mount intercom [2], (b) Commercial PCB at about 1942 [3]

## 1.1 History

Before PCBs were invented, bulky and error prone point to point constructions were used to wire electronic equipment (see Fig. 1.1a). In the 1920s, basically anything was used as substrate material as long as it was an insulator. Materials like Masonite, Bakelite, but also plain wood was utilized. The conductive tracks were initially made of brass, which was riveted onto the boards. Fig. 1.1b shows a picture of a commercially manufactured PCB for a radio around 1942. The next breakthroughs were in a chronological order: double sided PCBs (1950s), multilayer PCBs (1960s), liquid photoimageable soldermask for surface mount technology (1980s). Some more recent milestones in the PCB manufacturing are the laser drilled microvias for high density interconnects (1995) and Every Layer Interconnect (ELIC), which provides a way of interconnecting any layers within the PCB itself (2000s). Recently there was the integration of passives in between the PCB layers to reduce parasitic effects as e.g. capacitors can be positioned even closer to integrated circuits (2010s). Currently the research is going towards the evaluation of high frequency capabilities of PCB materials.

## 1.2 Microwave theory for dielectric material characterization of PCBs

This section is dedicated to give the reader a short introduction to compound of materials used for PCBs and the physical effects to be encountered in measurements.

### 1.2.1 PCB - the basic setup

A PCB is simply a compound of an insulator and a metal. According to Bohr's atomic model, an atom has discrete energy levels. By bringing together several atoms (i.e. solids), the discrete energy levels are cramping together and energy bands are the result, namely the valence band and conduction band. Depending on how many electrons are in the valence band bound to the nuclei, and how many can freely move around in the solid compound, serves as classification for the electrical properties. The band gap is used to group solid materials into the following manner: metals, semiconductors, and insulators [4]. Typical band gap values for an insulator are more than 5 eV, which represent a significant barrier for electrons. This barrier cannot be crossed, not even at high temperatures. Semiconductors show a band gap of about 1 eV. Such a band gap can be bridged by electrons already at room temperature to act as free charges. Metals do not have any energy gap at all and so for temperatures above absolute zero free charges are available. The PCBs measured within this thesis consist of two metallic layers separated by a dielectric material (the insulator). Such a compound is usually referred to as the core layer of the PCB.

### 1.2.2 Dielectric materials

As long as an insulator can be considered nonmagnetic, it is called dielectric. By applying an electric field to dielectric materials, three main polarization effects can be observed: orientation, ionic, and electric polarization. The polarization mechanisms are additive in nature, however, each polarization has a different frequency range on which its impact is highest. Fig. 1.2a shows the three polarization mechanisms occurring from lowest to highest frequency. The cause of electric polarization is the displacement of the negatively charged electrons towards or away from the positively charged nucleus. As the mass of the electrons is minuscule, this polarization can follow even very fast oscillations (close to the visible frequency range). The cause for the ionic polarization is a deformation of ionic bonds. The involved masses are higher than for electric polarization so the cut-off frequency reaches only the infrared range. The third one, and for frequencies up to 110 GHz most important polarization mechanism, is the orientation polarization. The requirement for this polarization is a permanent electric dipole moment and a rotational degree of freedom for the ions of the dielectric material. These dipoles are oriented according to the applied electric field and add in this manner some impact to the dielectric behavior of the material. The cutoff frequency for orientation polarization is in the microwave-, for the ionic polarization in the terahertz-, and the electric polarization in the petahertz range ($10^{15}$ Hz).

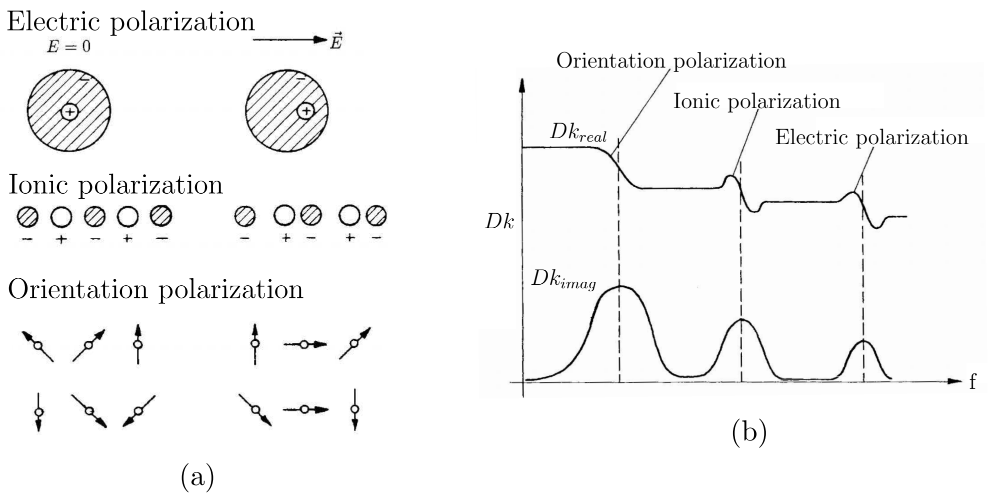


Figure 1.2: Polarization mechanisms: (a) Atomic and ionic behavior (b) Frequency dependence (both taken from [4])

All of the described polarization mechanisms can be formulated mathematically by the following relation (with the electric field $\vec{E}$ and the electric flux density $\vec{D}$):

$$\vec{D} = \boldsymbol{\epsilon}(f)\vec{E} \tag{1.1}$$

The permittivity $\boldsymbol{\epsilon}(f)$, or the dielectric constant $Dk$, is in the most general representation a tensor of order two (i.e. a matrix with nine components) and is the product of the free-space permittivity $\epsilon_0$ ($Dk_0$) as a scalar and the relative permittivity of the material $\boldsymbol{\epsilon_r}(f)$ ($Dk_r$). In common practice the term $Dk$ is more widely used than the rather scientifically connoted $\epsilon$. Within this thesis, the $Dk$ term is preferred and the investigated materials are considered isotropic, which reduces the permittivity tensor of order two to a tensor of order zero, a scalar.

Fig. 1.2b shows the real and the imaginary part of the dielectric constant over frequency for a generic material. The real value of $Dk$ is decreasing for increasing frequencies. Even though the ionic and electric polarization show a resonant behavior, there is a significant drop of $Dk_{real}$ after each polarization mechanism. Every polarization mechanism has its impact on the imaginary part of $Dk$ ($Dk_{imag}$) as well. The imaginary part covers dissipative losses due to the polarization process.

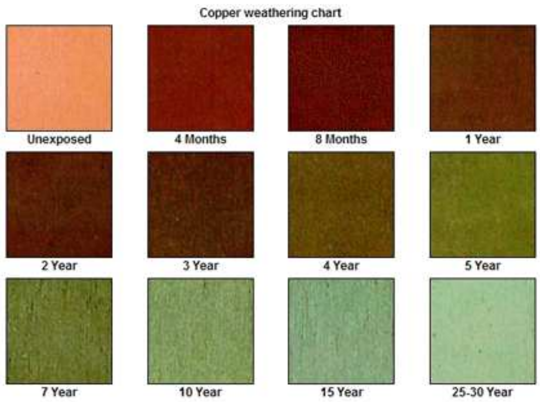


Figure 1.3: Copper corrosion over time [6]

### 1.2.3 Conductors

Several elements of the periodic table show good properties for using them as a conductive material on a PCB. The conductivity $\sigma$ of a metal is an important criterion to find a valid candidate. Usually copper is used for conducting currents on a PCB. Although copper is not the metal with the highest conductivity (silver would be approximately 6% better), it belongs to the group of non-precious metals what makes it much more cost effective than silver. Copper shows high softness that partly explains the high conductivity and thermal conductivity, as conductivity mainly is affected by scattering of electrons due to thermal vibrations of the atomic lattice [5]. The biggest drawback about copper is its inherent corrosion when exposed to atmospheric conditions. This causes copper to tarnish, which changes gradually over a few years from dark brown or black to green (patina). Fig. 1.3 shows copper corrosion for natural weathering conditions over a period of time up to 30 years.

For tackling this corrosion and tarnishing issues, a wide range of surface finishes is available that are used for covering the exposed bare copper traces. A wide range of surface finishes and their detrimental impact on the circuit will be discussed in theory in Sec. 1.5 and by measurements in Sec. A.2.

### 1.2.4 Skin effect

The resistance of an alternating current (AC) is significantly different from DC because the behavior how the fields interact with the conductor changes. For non-DC currents according to Faraday's law and the Maxwell-Ampère equation, there is an increasing opposing force for an electric current flow in the center of the conductor. The result is that a thick, near-perfect conductor (e.g. copper, silver) conducts the AC current only up to a certain skin depth $\delta$ [7]. This skin depth is inversely proportional to the square root of the excitation frequency. Mathematically the skin effect can be expressed as follows (with the conductivity $\sigma$, the excitation frequency $f$, and the permeability $\mu$):

$$\delta = \frac{1}{\sqrt{\pi f \mu \sigma}} \tag{1.2}$$

The skin depth is defined at what extent the current density falls to a certain level ($1/e$ with the Euler number $e$), which covers about 63% of the current within one skin depth. Values of this relation are for copper: $\delta(10\,\mathrm{MHz}) = 20.62\,\mu\mathrm{m}$, $\delta(1\,\mathrm{GHz}) = 2.1\,\mu\mathrm{m}$, $\delta(10\,\mathrm{GHz}) = 0.65\,\mu\mathrm{m}$, $\delta(100\,\mathrm{GHz}) = 0.21\,\mu\mathrm{m}$. Typical metal thicknesses of a commercially manufactured PCB are ranging in between several micrometers (e.g. the samples investigated in this thesis have $30\,\mu\mathrm{m}$ nominal copper thickness). This shows that already for frequencies slightly above 10 MHz the skin effect is impacting the measurements, as the skin depth of the top current is separated from the skin depth of the bottom current, which makes a frequency dependent investigation necessary.

### 1.2.5 Surface roughness

Surface roughness is an important component of surface texture. It is defined by the deviations of the normal vector of a surface from its ideal direction. The surface is considered rough if these deviations are high and smooth if the ideal normal vector is almost equivalent to the real normal vector. The benefit of a rough surface is that it has a higher friction coefficient than a smooth one. For PCB manufacturing this is an important figure of merit as the roughness is an indicator for the peel strength of the metallic cladding. For applications up to a few megahertz, a rougher surface of the metal can be considered as better as higher peel strength guarantees better reworkability of the PCB in the case of failure. However, for higher frequencies, roughness can be a limiting factor in terms of losses. As discussed in the previous section (Sec. 1.2.4), the conductivity has an important role for conduction losses, but also the distance that a current has to travel until it reaches its destination is important. For increasing frequency, the skin effect is pushing the current more and more into the rough surface and so the current must closely follow the topology of the surface. For rough surfaces this can be more than the double of path length and so the resistance is also more than doubled.

Fig. 1.4 depicts a surface at three different zoom factors. At the top, miniature flaws and the direction of lay can still be observed that both do not add much or negligible increase of surface area. At the second zoom factor, a certain waviness is shown which is mainly due to the mechanical manufacturing process or glass

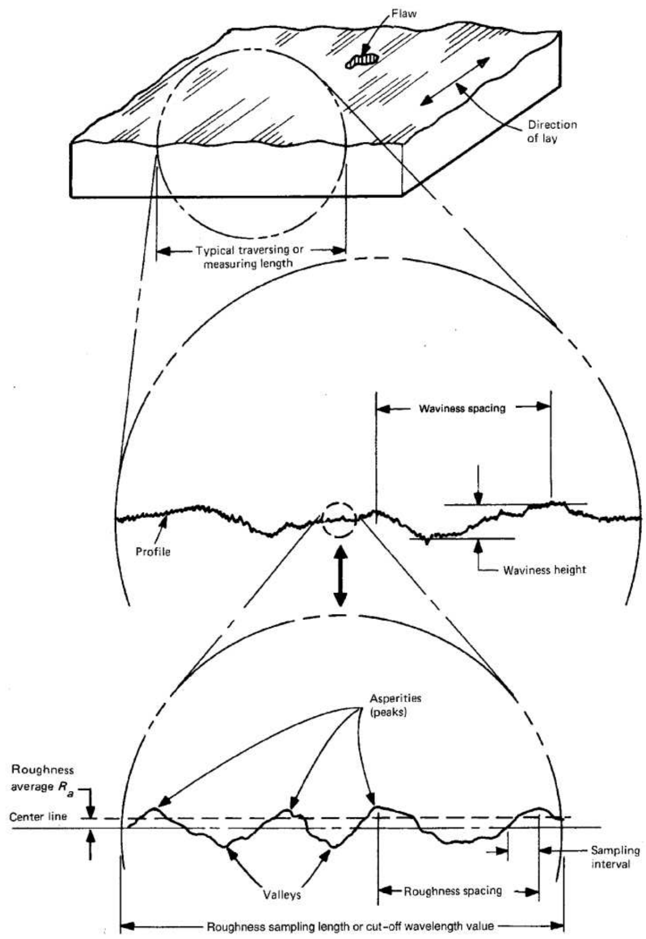


Figure 1.4: Surface roughness [8]

weave impressions from an underlying mat. This waviness is sometimes referred to as the low frequency component of the surface. The third zoom factor shows the roughness (in a stricter sense) that contributes mostly to the aforementioned peel off strength as it augments significantly to the total surface area.

## 1.3 Planar dielectric characterization methods and test board description

Microwave methods for material characterization can be divided into non-resonant methods and resonant methods [1]. These two methods are based on two microwave phenomena: microwave propagation and microwave resonance, respectively. Non-resonant methods are often considered to get a general knowledge of the dielectric materials over a continuous and wide frequency range. Resonant methods are usually taken to obtain accurate measurements of the dielectric properties at a single or at least a few frequency points. Both methods show good results for low conductivity (low substrate loss) materials.

### 1.3.1 Non-resonant method: Transmission lines

Non-resonant methods are fundamentally deducing the properties of the material from their impedance and wave velocities. Although there are also pure reflection methods, the focus here lies on non-resonant transmission/reflection methods. Especially for the transmission component of the characterization, any transmission line can be used to allow the wave to propagate (e.g. coaxial lines, hollow metallic waveguides, dielectric waveguides, and planar structures). An important aspect is also if the wave propagates in a homogeneous dielectric (e.g. a coaxial line) or a mixture of materials with different dielectric properties.

The basic approach for a transmission/reflection method is measuring transmission lines with different lengths to extract the complex propagation constant $\gamma$ (with the attenuation constant $\alpha$ and the phase constant $\beta$):

$$\gamma = \alpha + j\beta \tag{1.3}$$

One way is by investigating the measured difference of two lines with unequal lengths but same characteristic impedance, e.g. [9][10]. The main drawback of this concept is that for e.g. two lines only one measurement can be evaluated. This drawback can be overcome with an ABCD-parameter based approach [11]. This allows to evaluate each measured line on its own and not only as a difference in between two of them. This can be carried out when the discontinuities of the probe-to-PCB-transition are compensated by a TRL-calibration (see Sec. 1.6).

Typical transmission lines used for interconnecting circuitry are microstrip (MS) and conductor-backed coplanar waveguide (CBCPW). One further transmission line mode that should be discussed as well is the substrate integrated waveguide (SIW). The range of applications utilizing higher frequencies is steadily increasing and by that, the SIW gains more importance. A crucial benefit for all three transmission lines is that the they can easily be manufactured on a PCB with just one substrate layer and double sided copper cladding.

The characteristic impedance $Z_0$ of any lossless transmission line can be mathematically expressed as (using expressions per unit length (pul) for the inductance L' and the capacitance C'):

$$Z_0 = \sqrt{\frac{L'}{C'}} \tag{1.4}$$

MS just needs one trace separated by one layer of substrate material and an electric reference plane to operate (see Fig. 1.5a). A circuit designer using MS has several design parameters to change $Z_0$ according to requirements: the dielectric constant of the substrate $Dk$, the substrate thickness $h$, and the line width $w_{MS}$. How one of these parameters changes the impedance can easily be comprehended by thinking about the capacitance pul $C'$ of the transmission line. For increasing $Dk$ or $w$, the capacitance increases and $Z_0$ drops. For increasing $h$, $C'$ drops and $Z_0$ rises. Except for changing $Dk$, the same discussion could be carried out for $L'$ too. Important is to keep in mind the field pattern of an MS line as well as some part of the electromagnetic field propagates in air (Fig. 1.5a shows the electric field as dashed lines), which make these transmission lines dependent on objects that may be placed in the air region.

CBCPW has a slightly more complex cross-section than MS as the reference plane is additionally brought to the upper surface by plated through holes (PTH). This gives an designer even one more design parameter to adjust $Z_0$ according to requirements: the dielectric constant of the substrate $Dk$, the substrate thickness $h$, the line width $w_{CBCPW}$, and the gap width $g_{CBCPW}$. By narrowing the gap, $C'$ increases as some capacitance pul is added to the trace sides and this reduces $Z_0$. CBCPW lines are more robust to objects in the upper air region as some electric field is now confined in the gap region in between the top trace and the upper reference plane (see Fig. 1.5b).

SIW is like a classical waveguide (e.g. WG15), only that it is built into a PCB and so the electromagnetic wave is propagating in the dielectric of the PCB. The PTHs on both sides represent the sidewalls of the waveguide (see Fig. 1.5c). For a classical waveguide the most important parameter is the cutoff frequency $f_{cutoff}$. This frequency occurs when half of the wavelength fits into the longer side of the waveguide (for SIW in most cases it's the horizontal length $w_{SIW}$ which is defined by the PTH spacing). This narrows the design parameters down to: $w_{SIW}$ and the dielectric constant of the substrate $Dk$. The vertical confinement, the thickness $h$ should be small enough so that the operation frequency stays well below any parasitic modes that could be excited by field components in that orientation.

As SIW parasitic higher order modes (like $TE_{1x}$ and $TM_{xx}$) could propagate for frequencies beyond $f_{cutoff}$, MS and CBCPW show a similar behavior when operated at higher gigahertz frequencies. For MS and CBCPW the higher order waves are usually not the problem as they only propagate when the substrate thickness reaches half wavelengths, the surface waves [12] are the bigger problems. These waves need to be specially taken into account during the characterization method (see Sec. 2.1 for more details).

Fig. 1.6 shows top views of the investigated test structures for MS- and CBCPW with a targeted $50\,\Omega$ characteristic impedance. The designed line widths are for the substrate materials “Megtron 6” and “Pyralux TK”, $260\,\mu$m and

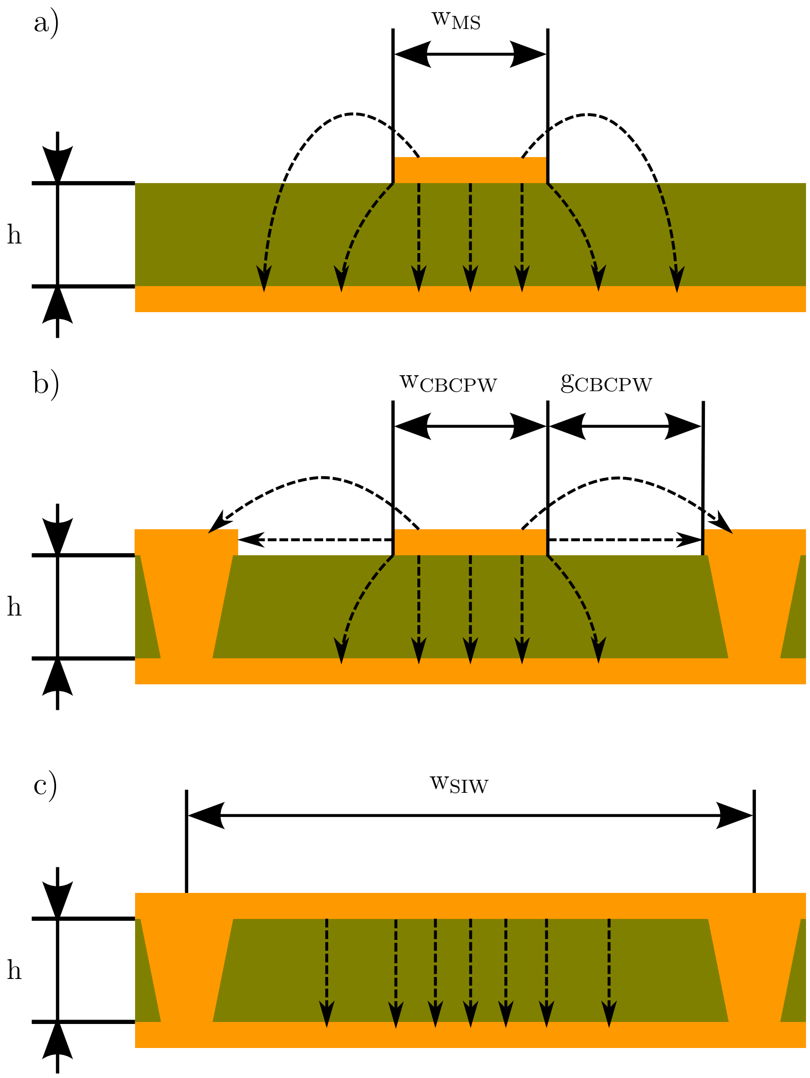


Figure 1.5: MS, CBCPW, and SIW transmission line modes with dimensions with the electric field in dashed lines

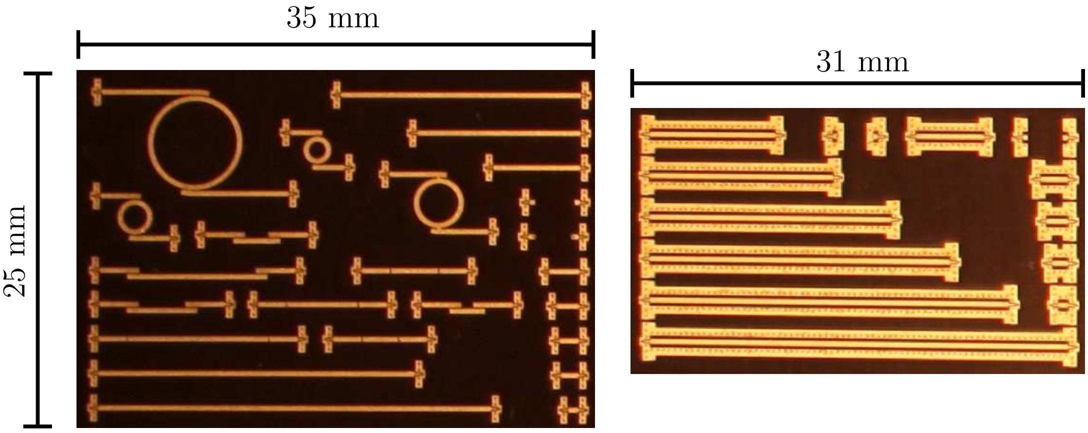


Figure 1.6: MS and CBCPW test boards

320 $\mu$m for MS, 250 $\mu$m and 320 $\mu$m with 250 $\mu$m gap for CBCPW. Both materials have a substrate thickness of 125 $\mu$m. TRL calibration standards have been included to correct for systematic errors during measurements (see Sec. 1.6 for more details).

### 1.3.2 Resonant methods: MS resonators

Resonant methods usually have higher sensitivities and accuracies than their non-resonant counterpart. The basic principle is that a resonator with fixed dimensions changes its resonance frequency and quality factor depending on materials brought into its proximity. Within this work, MS resonators of different kinds, different feedings, and different resonant frequencies were designed and manufactured. A crucial advantage of custom-made MS resonators for material characterization is that the measured test sample mimics closely the actual application, as all involved materials had the same treatment as the finished PCB will have.

The materials under test (MUTs) for the resonators are also “Megtron 6” and “Pyralux TK”. All devices under tests (DUTs) are designed with a MS-based 50 $\Omega$ wave impedance for the resonators and the feed lines (Fig. 1.6). The design contains four ring resonators and four ribbon resonators with fundamental resonance frequencies of 10, 20, 30, and 40 GHz. The designed line widths are 260 $\mu$m and 320 $\mu$m, and the resonator coupling gap is 90 $\mu$m for both MUTs. The substrate thickness is 125 $\mu$m. For the ring and the ribbon resonators, the capacitive couplings to the resonators is done by parallel-line coupling (side-coupling) for lowering insertion loss but still having high quality factors. The most important design parameters for these ring resonators were the circumference for the fundamental resonance frequency, as well as the coupling line length and coupling gap for modeling the quality factor and insertion loss.

## 1.4 Tolerances for PCB manufacturing processes

One of the big challenges for getting reliable measurements is the significant tolerance for the commercial wet-etching process that is used for fabricating the test structures. To the author's knowledge comparable investigations up to 110 GHz were conducted with samples manufactured with a semiconductor process [13]. Although these results are scientifically highly interesting, these test structures can only be manufactured in very small samples at a high cost. Within this thesis the test structures were manufactured by a commercially widely used, high volume, panel plating process. Not only is the manufacturing difficult for achieving dimensions within several micrometers, but also there is a high etching tolerance of $\pm$ 20% for the minimal structure sizes tied to this process. Because of this high tolerances, several considerations had to be taken into account to achieve reliable and reproducible measurement for this extended frequency range.

## 1.5 Surface finishes techniques for PCBs

As shown in Sec. 1.2.3, the prominent conductor for PCBs is copper due to its high conductivity and comparably low price as non-precious metal. However, if raw copper is exposed to atmospheric conditions an oxide layer forms on the surface that degrades the performance. To overcome this shortcoming, the usual approach is plating copper with materials that on one hand serve as a diffusion barrier and on the other do not oxidize when exposed to atmospheric conditions. Generally this is achieved with a compound of at least two different materials. The outermost material in direct contact with the atmosphere should be low reactive with high conductivity (especially for higher frequency applications). Two auspicious (precious) metals are silver (Ag) and gold (Au). Both metals have favorable valence electron configurations with only a half full s-orbital leading to high conductivity. Actually also copper belongs to the same group 11 of chemical elements like silver and gold, but unfortunately copper tarnishes with oxygen.

Silver would have the highest conductivity of any metal surface, however, it tends to tarnish as well. The tarnish process is not as fast as for copper, because silver does not react with the abundant oxygen, but the least common hydrogen sulfide. Although the tarnish process is slowed down compared with copper, the shelf life of electronic products is still significantly decreased and thus the more expensive gold is preferred.

Nickel (Ni) is used in most cases as an additional corrosion inhibitor as well as diffusion barrier. The diffusion barrier is important to prevent copper atoms from diffusing into the gold surface what would lead to the aforementioned tarnishing again. The nickel layer should be as thin as possible depending on the application. Typical nickel layer thicknesses are ranging from several hundreds of nanometer up to several micrometers. Nickel plating can also harden the surface to decrease wear resistance. Especially for high frequency applications it should be kept in mind that nickel is a ferromagnetic material which has significant impact on the skin effect behavior of the measured samples.

The surface finishes investigated within this thesis are: electroless nickel immersion gold (ENIG), electroless nickel electroless palladium immersion gold (ENEPIG), tin, and hard gold.

### 1.5.1 ENIG

This finish is made by an auto-catalytic chemical technique to deposit nickel-phosphorus or a nickel-boron alloy on the copper surfaces, without passing an electric current through the solution [14]. For ENIG, nickel is not only the diffusion barrier but is also the layer where the soldering occurs. The comparable thin gold layer protects the nickel from oxidation during storage. For ENIG, the nickel layer is about 30 times thicker than the gold layer (typical values are for the gold layer below $0.2\,\mu$m and nickel layer below $6\,\mu$m). ENIG surfaces have good bonding capabilities for aluminum wires but not gold wires.

### 1.5.2 ENEPIG

For this finish, a third layer is added to the compound which is palladium (Pd). The palladium thickness is usually smaller than $0.5\,\mu$m by keeping the nickel and gold at the same thicknesses as for ENIG. The benefit of this compound is that it forms a superior solder joint with lead-free solder. Another benefit of ENEPIG is that it offers good bonding capabilities for gold wires. Thinking about high frequency application the palladium layer will increase losses as its conductivity is even below nickel.

### 1.5.3 Immersion tin

For high frequency applications, tin should have better performance than nickel as it is only paramagnetic and thus eases the impact losses caused due to the skin effect. The immersion tin finish forms a intermetallic joint with copper. This strong affinity can cause over time a noticeable diffusion of copper into tin and vice versa and thus lowers the shelf life of the PCBs. A significant problem for this finish are tin whiskers which could cause short circuits.

### 1.5.4 Hard gold

The main difference between ENIG and the hard gold finish is that the gold thickness is much thicker. The nickel to gold ratios of about 2-3 emphasize this considerable increase of gold compared with a ratio of 30 for e.g. ENIG. The hard gold surface is very durable. For that reason it is most commonly applied to high-wear areas. This finish has poor solderability so it is usually not applied to solderable areas on a PCB. The price is also an important factor as it is by far the most expensive finish on the market. Additionally, the shelf life of gold plated PCBs is excellent.

## 1.6 Probe selection and calibration methods

All designed test structures are MS- or CBCPW-based with a targeted 50 Ω characteristic impedance. Due to mechanical limitations of the wafer prober, the length of lines was limited to a maximum of 25 mm. There are many different probes available on the market, however, the desired frequency range from DC up to 110 GHz narrows down the selection to three probes (from two manufacturers). Additionally to the extended frequency range, there are height variations for each pad of the GSG-pads for probing commercially manufactured PCBs. Usually probes are designed to contact extremely flat surfaces (e.g. wafers), however, for the test structures measured in this thesis a height variation of several micrometers is unavoidable. So the probes needed to be spring loaded to overcome this height difference without taking damage. This constraint further narrows down the available probes to two probes that offer reliable contacts for height variations up to 20 $\mu$m. The material of the probe tips has also an important impact on measurements. There are several materials that show auspicious behavior for wafer probes due to their hardness (elasticity) and low contact resistance. The most prominent ones are: tungsten and beryllium copper (BeCu). Tungsten has superior hardness over BeCu, but inferior contact quality for repeatable contacts with low resistance, especially for probing precious metals. In this case a tungsten probe was chosen as several hundreds of manual contacts had to be made and the risk of damaging the BeCu probe would have been high. As only one of the two probes could be manufactured with a reduced contact area (RC), the Cascade ACP110-A-GSG-RC tungsten probe with a pitch of 100 $\mu$m was chosen.

By touching the measurement samples with the probes, an unavoidable discontinuity occurs as probing pads with the same pitch as the probe tips (but

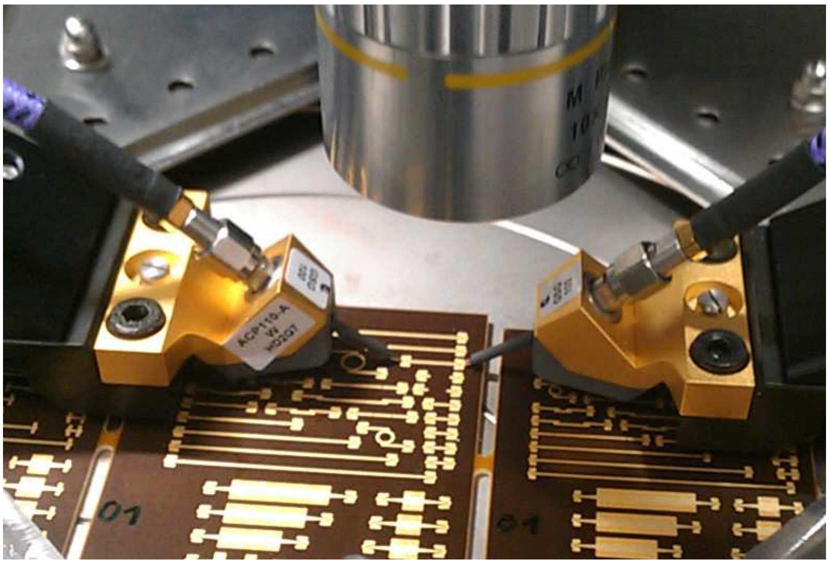

Figure 1.7: Probing of MS line

obviously different substrate) were needed. The MUTs have a different $Dk$ than the probes which leads to an impedance mismatch ranging from $70\,\Omega$ to $90\,\Omega$ of characteristic impedance depending on the selected MUT. Although this transition from the probing pad to the $50\,\Omega$ DUTs is designed to achieve the least reflection loss possible (see Sec. 1.6.2 for an in-depth investigation of the launching structures), this unavoidable discontinuity is still removed from measurements by an custom-designed TRL calibration kit.

In this investigation two calibration methods were applied: an LRRM calibration to the probe tips, and a custom made TRL calibration to move the reference plane directly to the DUTs themselves.

### 1.6.1 Wafer prober calibration: LRRM

A calibration substrate provided by the probe manufacturer was used to carry out an LRRM calibration to shift the reference plane to the probe tips. The LRRM calibration method was used because it has an uncertainty as low as a multiline TRL calibration, however, with the benefit of not measuring line elements with different lengths. This approach speeds up the calibration process as the probing distance has not to be adjusted during calibration. Another benefit is that the utilized match calibration standard needs to achieve a perfect $50\,\Omega$ characteristic impedance only at low frequencies. This is possible because the calibration method internally models the match standard with an added series inductance and thus achieves broadband behavior for this standard [15]. The reason why

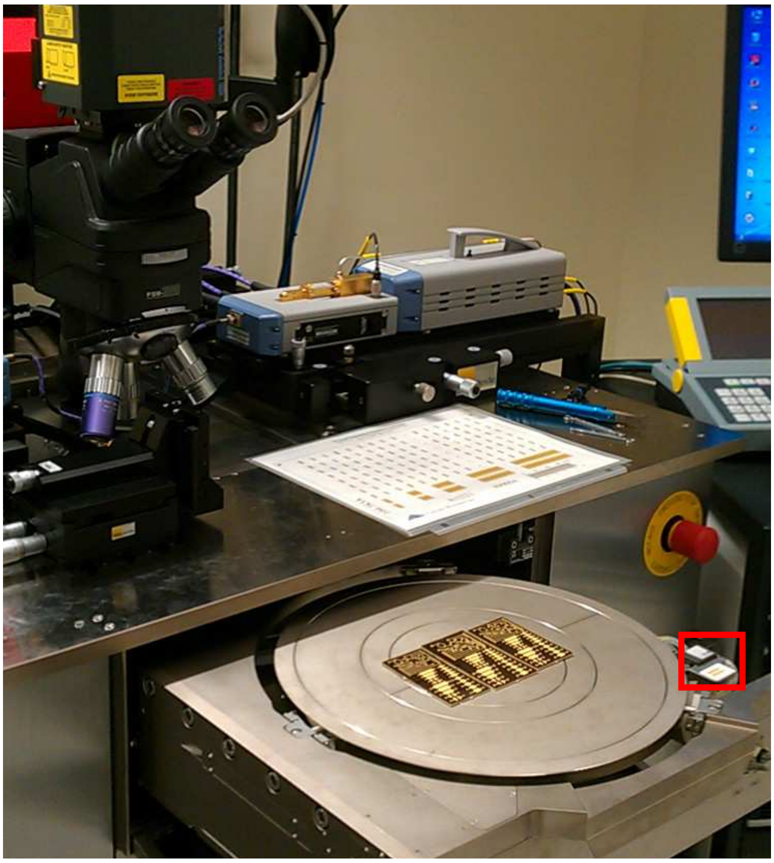

Figure 1.8: Wafer prober with DUTs and calibration substrate (red rectangle)

the LRRM calibration was carried out before a subsequent TRL calibration is to spot easily and instantaneously contacting issues during measurements and thus being able to resolve them readily.

### 1.6.2 Launching pad investigation

From the probe pads with a pitch of $100\,\mu$m to the dimensions of a $50\,\Omega$ line (depending on the MUT), an electromagnetically smooth transition is desired [16]. Three launching pads for wafer prober measurements were evaluated (see Fig. 1.9): one step- and two tapered-transitions. Two tapered transitions were considered with different lengths (limited by positive integer multiples of the minimum via diameter). As the maximum length for a measurable DUT was limited to 25 mm and the lines should take advantage of most of the available length, the tapered designs were limited to a one via and a two via approach. For the tapered transitions, the gap between the tapered signal line and the angled

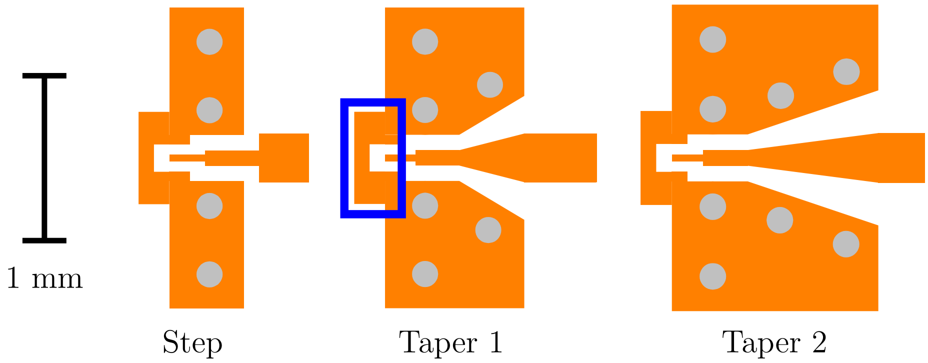


Figure 1.9: Investigated launching pads with shorting paths (blue)

top ground planes was TDT-simulated and optimized for a smooth transition. Every unnecessary over- and/or undershoot in impedance would increase the reflected energy and so the reflection loss. On the left side of each launcher an additional shorting path in between the two top ground pads was added. These were necessary for locally reducing the fabrication process limits and therefore being able to manufacture the minute launching pads.

The results for the TDT simulation with varying gap width ($\text{Taper}_{gap}$) are shown in Fig. 1.10. The transition with the smoothest impedance response is for $\text{Taper}_{gap} = 200\,\mu\text{m}$. The same result could be observed in the frequency domain with S-parameter simulations for $\text{Taper}_{gap} = 200\,\mu\text{m}$ as the reflection loss and the transmission loss show concordant results.

The measurement results $S_{21}$(dB) for two 50 Ω MS-lines with length l = 5 mm and l = 10 mm and a "Taper 2"-pad at each side is shown in Fig. 1.11a. Investigating this measurement closely, it can be seen that there is an additional resonance effect superimposed on top of the typical mismatch error. A time-gated version of the measurements was added to the figure in a solid color to stress the slight resonance. It can be concluded that this resonance occurs independently of the line length at roughly 80 GHz. The $S_{21}$ measurements for all launching pads for a l = 5 mm line are shown in Fig. 1.11b. The superimposed resonance has less impact on the "Taper 1"-pad and basically no impact on the "Step"-pad. A resonance in the transmission loss of S-parameter measurements gives rise to a nonlinear phase behavior at that frequencies. As the main characterization technique within this thesis relies on phase measurements, the "Step"-pad was taken as it shows the best linear phase response of the three investigated launching pads.

The designed launching pads should also show high robustness with respect to manufacturing tolerances within a set of TRL-calibration standards. A thru, a reflect, and a line standard with applied "Step"-pads were 3D-simulated to assess

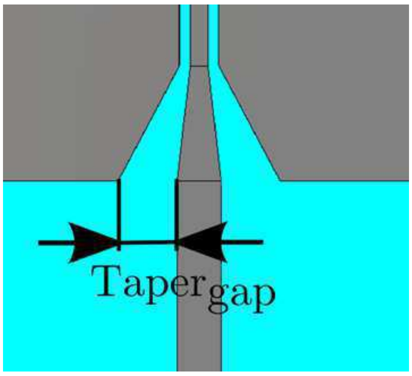


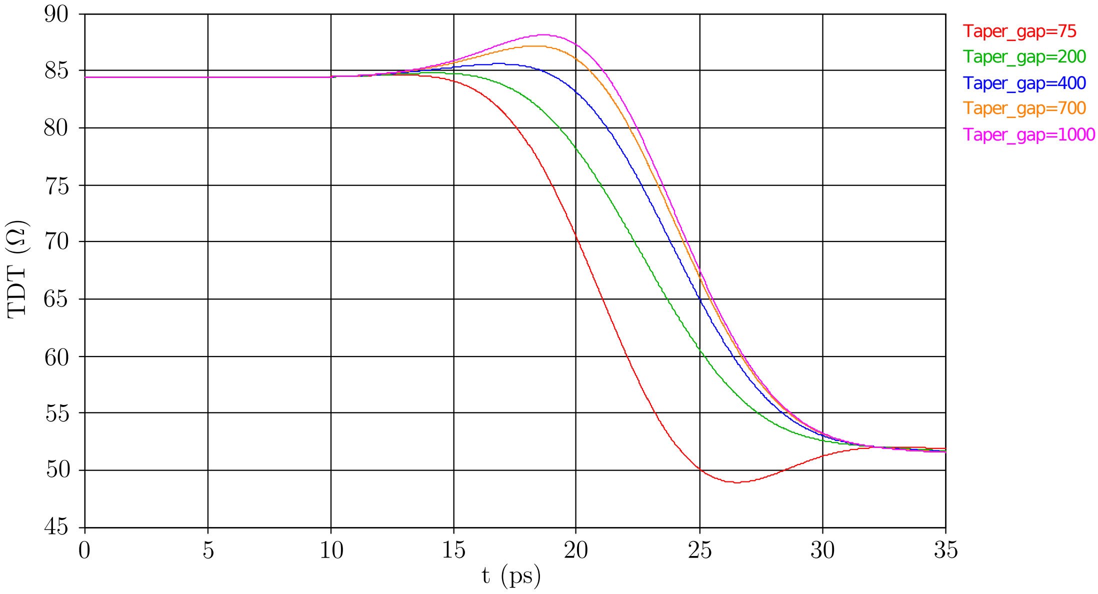


Figure 1.10: TDT simulation of tapered launch pad

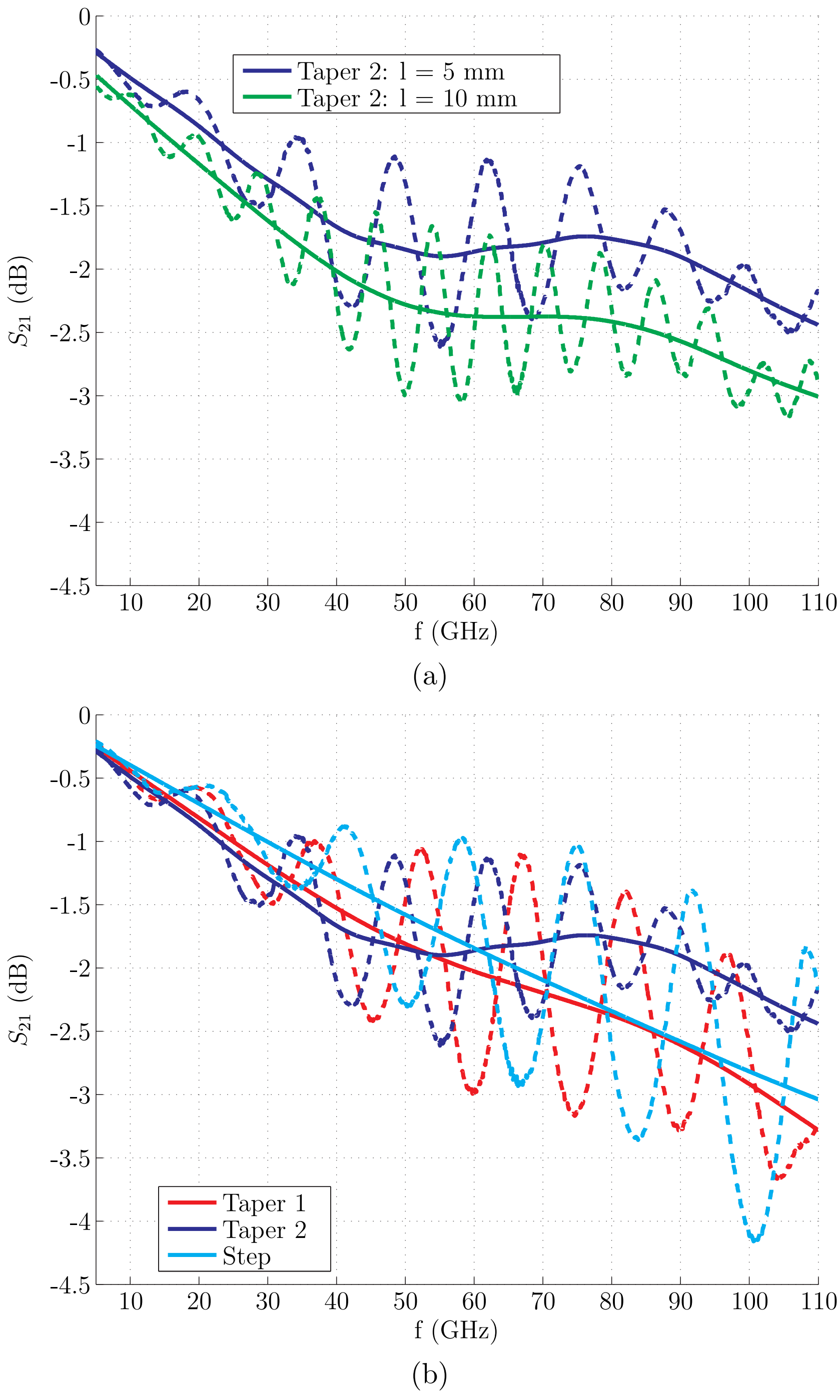


Figure 1.11: Launching pad investigation: (a) Measurements and time-gated version for “Taper 2”-pads (b) Measurements of all three launching pad designs

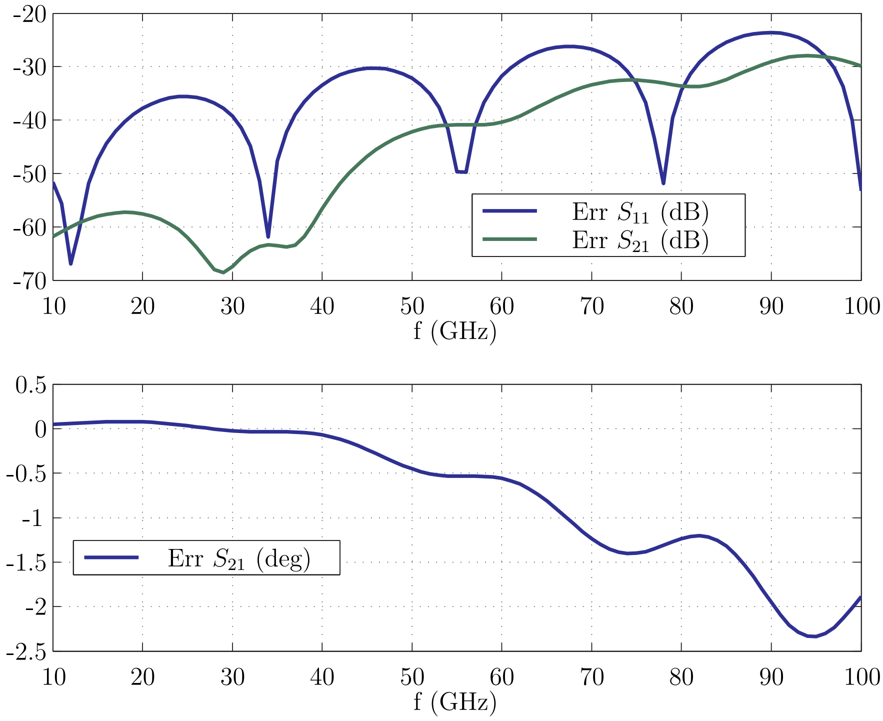


Figure 1.12: Impact of tolerances on TRL-analysis

the variation of the calibration with respect to manufacturing tolerances. The nominal dimensions, as well as dimensions with deviations within ±10% were simulated for each calibration standard. These simulation results with the nominal and the deviating dimensions were randomly permuted and processed within a TRL calibration routine to find the worst-case impact on the scattering parameters. The maximum calibration error is defined as the highest reflection loss and the lowest insertion loss for all permutations. Fig. 1.12 depicts this worst-case results compared with simulation results for nominal launching pads. The maximum systematic errors for $S_{11}$, $S_{21}$, and Phase($S_{21}$) is occurring for the highest simulated frequencies and is $-25$ dB, $-30$ dB, and $-2.5$ deg, respectively. It can be concluded that for the measurements the process tolerances do not deteriorate the TRL calibration significantly as the error lies within the measurement uncertainty of a commercial VNA.

### 1.6.3 TRL-calibration

For an evaluation of the TRL-calibration, the measurements before and after the computed TRL calibration are presented. Fig. 1.13a depicts the reflection loss for all manufactured and measured MS lines with calibration to the probe tips and Fig. 1.13b with subsequently applied TRL calibration. After the TRL calibration the MS reflection loss drops below −24 dB, which is an improvement of about 20 dB.

Fig. 1.14a shows the insertion loss for the same samples as for the reflection loss with a calibration to the probe tips and in Fig. 1.14b with TRL calibration. In the comparison of transmission loss, the additional losses of the launching pads were corrected and are about −1.5 dB. Although the absolute loss correction seems not very high, it makes a significant impact as the overall losses are only in the one digit dB-range. It can be clearly seen that the impedance mismatch due to the probe to board connection was removed from the measurements in the deembedded plot.

The measurement results for the CBCPW lines before and after TRL calibration show similar improvements like in the MS case, and thus are not plotted explicitly.

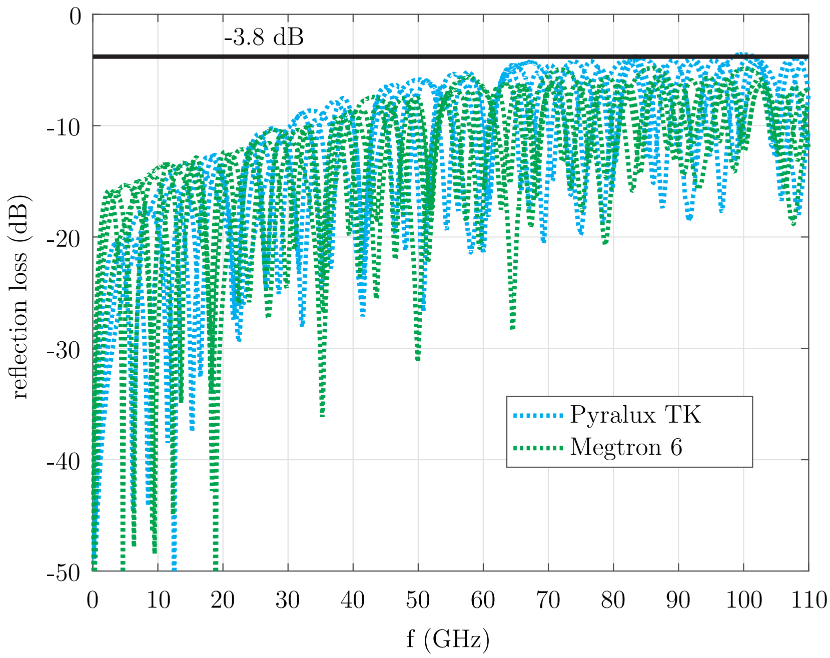


(a)

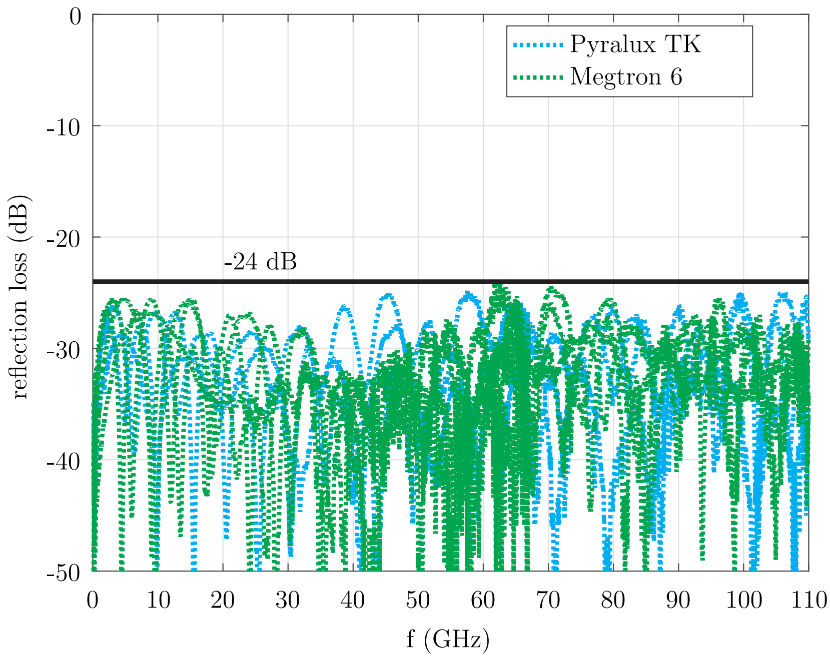


(b)

Figure 1.13: Reflection loss of MS: (a) without TRL calibration (b) with applied TRL calibration

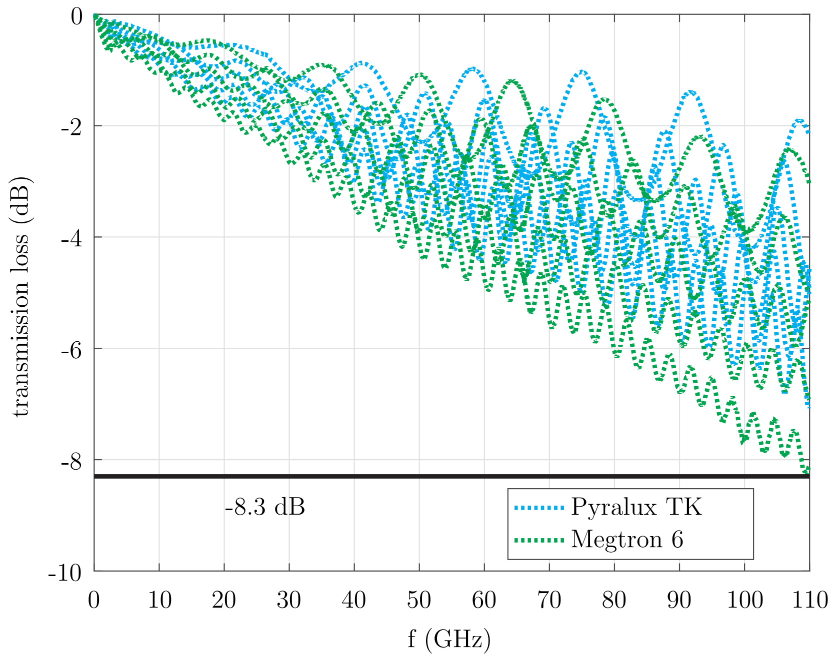


(a)

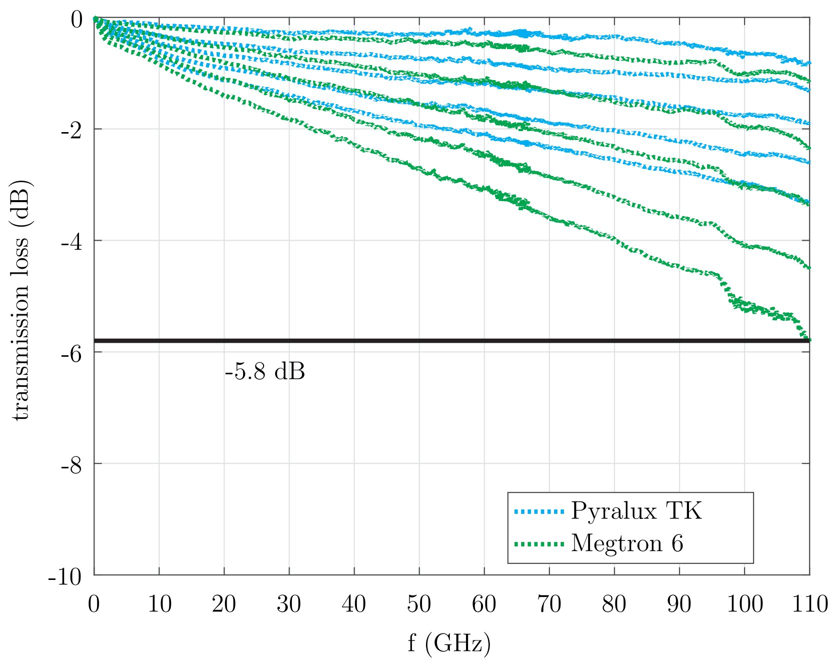


(b)

Figure 1.14: Transmission loss of MS: (a) without TRL calibration (b) with applied TRL calibration

## 1.7 Measurements of $\gamma$ and $Z_0$

As shown in Fig. 1.6, there are redundant DUTs on each test board (i.e. transmission lines with the same cross sections but different lengths). This allows an analysis of the variances within all measurements. The dielectric properties and substrate height are considered constant for all measured lines for each test board. These two parameters depend on the process adjustments at the fabrication of the substrate materials and tend to be constant for panel sizes much bigger than the size of the investigated test structures. Possible measurement variations originate from manufacturing tolerances of the MS line width and CBCPW line- and gap-width (Fig. 1.5).

Fig. 1.15 and Fig. 1.16 display measurements of the complex propagation constant. At certain frequencies, box plots were computed to depict the distribution of the measurements over frequency. It can be noted that the distribution for $\alpha$ (normalized by line length) widens towards higher frequencies. Generally, the attenuation constant $\alpha$ is a superposition of three different loss effects: the radiation loss $\alpha_r$, the dielectric loss $\alpha_d$, and the conductor loss $\alpha_c$. As both substrates have very low losses and these losses are assumed to be the similar for each line on one manufactured test board, $\alpha_d$ should stay constant. For straight transmission lines, $\alpha_r$ can also be assumed negligible. In this case the main loss contributor, and also the only one that depends directly on the line width, is the conductor loss. The conductor loss decreases for wider lines and increases for narrow lines which also depends on frequency [17], and thus has impact on the measured distribution. This is not the case for the normalized phase constant $\beta_{norm} = \beta/\beta_0$ (with the free space phase constant $\beta_0 = 2\pi/\lambda$) whose distribution remains almost constant up to 110 GHz. The phase constant depends mainly on the ratio substrate height to conductor width without frequency dependence [18].

By comparing MS and CBCPW, it can be noticed that CBCPW features higher attenuation due to additional $\alpha_c$ (in contrast to [19]). This conclusion is drawn by evaluating the normalized phase constant and attenuation constant at the same time. $\beta_{norm}$ shows a slightly lower value for CBCPW. This is caused by the wave propagating more in air compared to MS, resulting in lower dielectric losses. However, CBCPW still has a higher attenuation constant than MS which leaves $\alpha_c$ as the loss source [20]. For the CBCPW lines, a resonance at 80 GHz for Megtron 6 and 90 GHz for Pyralux TK is observed. This resonance is considered to be caused by the cross-sectional via spacing of approximately 1000 $\mu$m. By computing $\lambda/2$ for the stated via spacing at 90 GHz with data sheet values of Megtron 6 and at 100 GHz for Pyralux TK, the resonance frequencies are closely obtained.

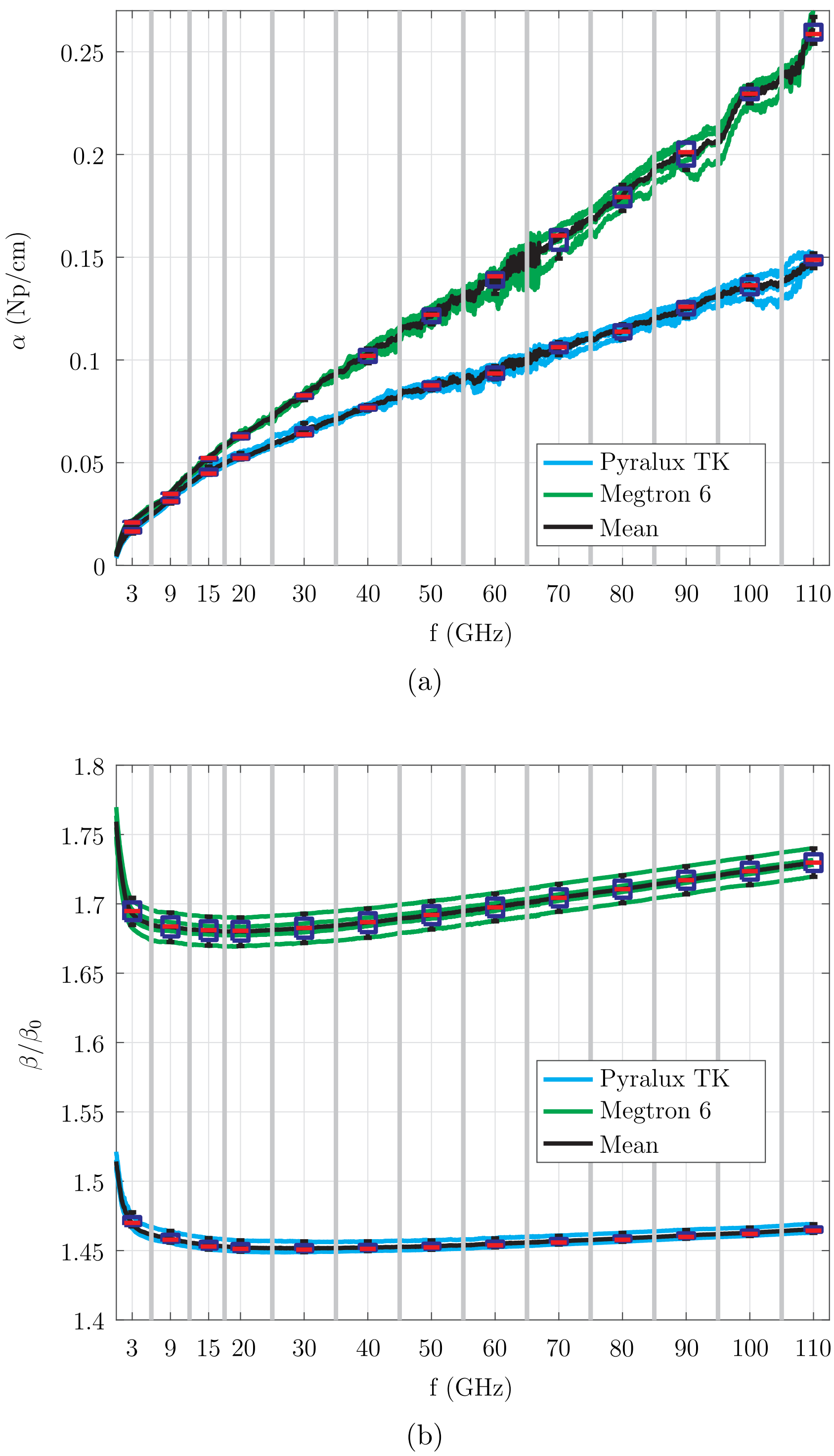


Figure 1.15: Measured complex propagation constant $\gamma$ for both materials MS: (a) attenuation constant $\alpha$ (b) normalized phase constant $\beta_{norm}$

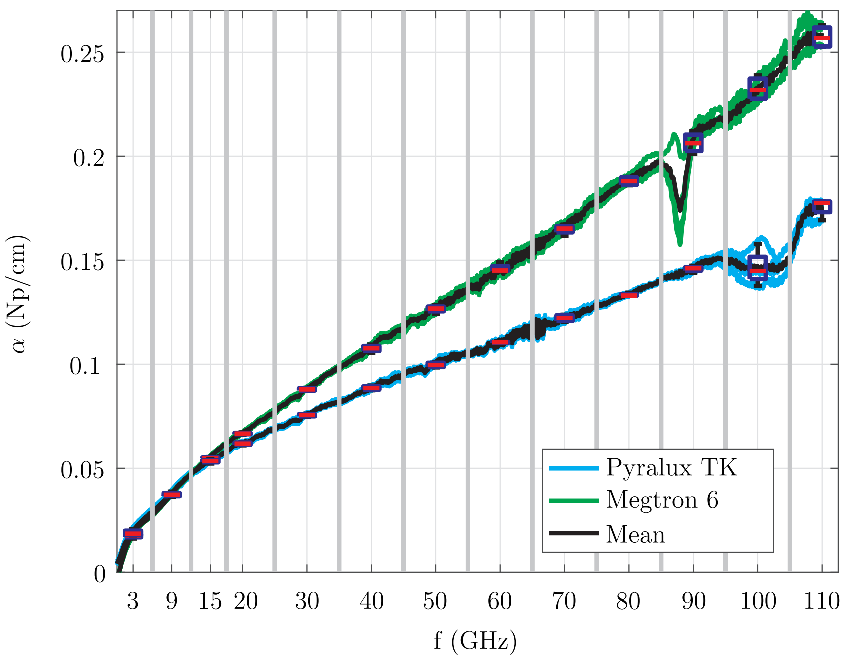


(a)

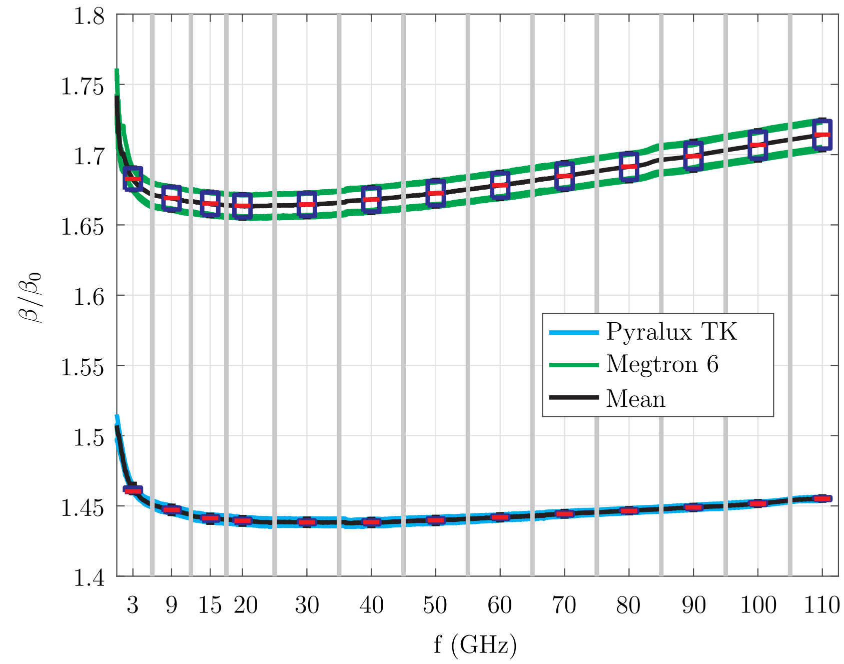


(b)

Figure 1.16: Measured complex propagation constant $\gamma$ for both materials CBCPW: (a) attenuation constant $\alpha$ (b) normalized phase constant $\beta_{norm}$

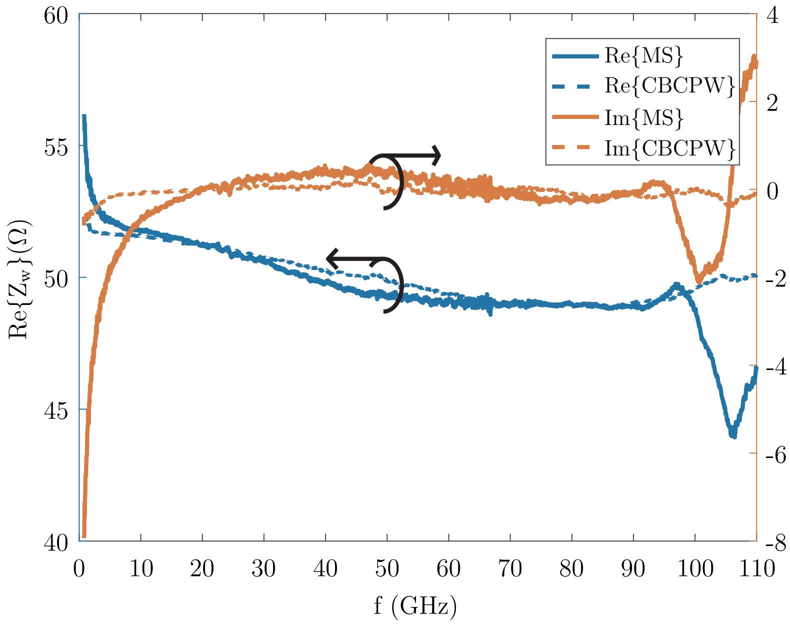


Figure 1.17: Wave impedance $Z_w$ for Pyralux TK

Fig. 1.17 shows the imaginary and real part of the wave impedance $Z_0(f)$ of MS and CBCPW for Pyralux TK. The utilized method for computing $Z_0(f)$ is taken from [11]. The impact of the aforementioned resonance for CBCPW can clearly be recognized in $Z_0(f)$ as well. By investigation of the real part of $Z_0(f)$, it can be concluded that the targeted impedance of $50\,\Omega$ was reached for approximately $\pm 5\%$ within most of the bandwidth (except for CBCPW at the resonance and lower frequency range).

## 1.8 Conclusion and thesis outline

Within this introductory chapter the broad field of material characterization was tailored to the designated task, a broadband dielectric material characterization for PCB substrate materials. Emphasis was put on the challenge to get reliable and reproducible measurements. For that reason many different aspects were mentioned: the fundamental definitions of a multi-layered compound of metals and isolator (known as PCB), the effects that may impair a reliable characterization for broadband measurements, the design of the launching pads to achieve linear phase behavior, the applied two-tier calibration, the redundant DUTs for coming to grips with manufacturing tolerances, and an evaluation with two different methods (resonant and non-resonant). The measurement results for $\alpha$ and $\beta/\beta_0$ shown in Sec. 1.7 are used as a foundation for the following chapters to deduce the material properties of the MUTs for a broad frequency range up to 110 GHz.

The next chapter (Cha. 2) will focus on the dispersion behavior of MS and CBCPW lines, representative for transmission lines with inhomogeneous stack-ups.

# Chapter 2

# Dispersion behavior for dielectric measurements of planar inhomogeneous stack-ups

If materials are characterized for a broad frequency range it is important to take into account dispersion effects. Any dispersion that is not taken into account may impair the results up to a significant degree. The focus of this chapter lies on inhomogeneous stack-ups because well-known representatives like MS and CBCPW do not only have one dispersive effect but two. For these two transmission line modes it would make a difference of approximately 10% of overall accuracy if the dispersion behavior would not be taken into account. As different effects are causing these two dispersive behaviors, the chapter starts with a description of the causes and the terminology to make a distinction easier.

## 2.1 Terminology of $Dk$

Two noticeable dispersive regions can be observed in the measurements (see Fig. 2.1). Firstly, the measured $Dk$ is decreasing for frequencies up to approximately 20 GHz. This is due to the frequency dependent skin effect. The skin effect causes on the one hand the internal inductance of the line to diminish, so that only the outer inductance, the inductance occurring in air and substrate, is present in the measurements from a certain frequency on. On the other hand, due to the decreasing skin depth the resistance increases crucially, especially as the surface roughness also adds extra losses (see 1.2.4). Secondly, for frequencies above 20 GHz, the measured Dk is steadily increasing up to the maximum measured frequency as more and more of the wave is forced to propagate in the

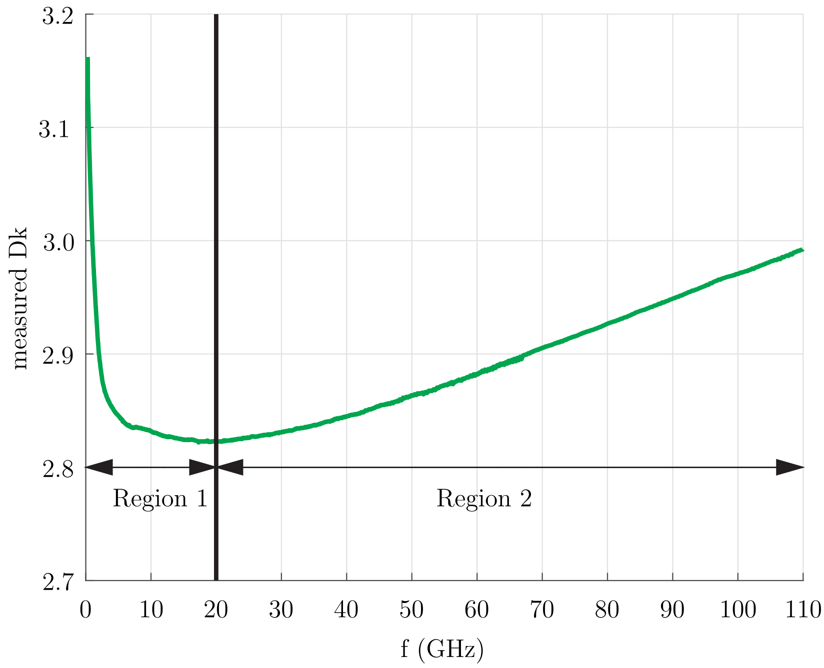

Figure 2.1: Measurements of Dk for MS with Megtron 6

substrate.

For easier referencing, different terms and suffixes for $Dk$ are used. If conductor properties are included in measurements, the decreasing $Dk$ behavior, the term apparent dielectric constant ($Dk_{app}$) is used.

The effect of increasing $Dk$ happens because of the inhomogeneous stack-up. However, the impact of the inhomogeneity has to be split into a frequency dependent and a frequency independent part. As long as any of these two components is present, the term effective dielectric constant ($Dk_{eff}$) is used. For the frequency dependent part, more and more electromagnetic field is drawn into the area in between the line and the GND plane, and thus the measured $Dk$ increases for higher frequencies. Even after the compensation of this increasing behavior there is still a bias present in the measurements. This is also caused by the inhomogeneity of $Dk$ which is present already at low frequencies. This bias can readily be taken care of by formulas utilizing the dimensions of the line to end up with the $Dk$ of the substrate itself.

Fig. 2.2 shows all of these introduced terms for an MS cross section. The frequency dependent impact on the measured dielectric constant is emphasized in the top part wherein the crowding of the electric field below the line for an increasing frequency and the skin effect is shown. The mapping of the partly in air propagating wave is emphasized in the middle section, and the lower section shows the desired field within the substrate only. For each part of the plot, the

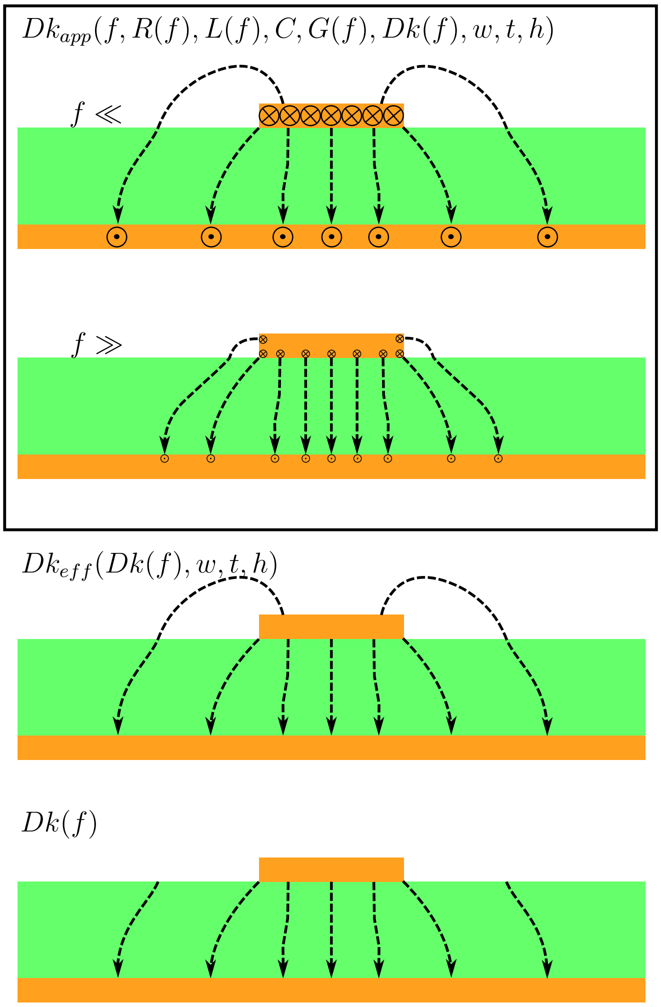


Figure 2.2: Different terms for the dielectric constant

dependent parameters are shown within parentheses (with frequency f, resistance R, inductance L, capacitance C, conductance G, line width w, line thickness t, and substrate height h).

The first dispersion to be discussed in detail is the positive dispersion within the next section (Sec. 2.2).

## 2.2 Positive dispersion of the measured $Dk$

By bringing two electrical conductors into close proximity it can be imagined that the changing magnetic field of each conductor induces an electric field into the other conductor. This electric field causes, for finite conductivity materials,

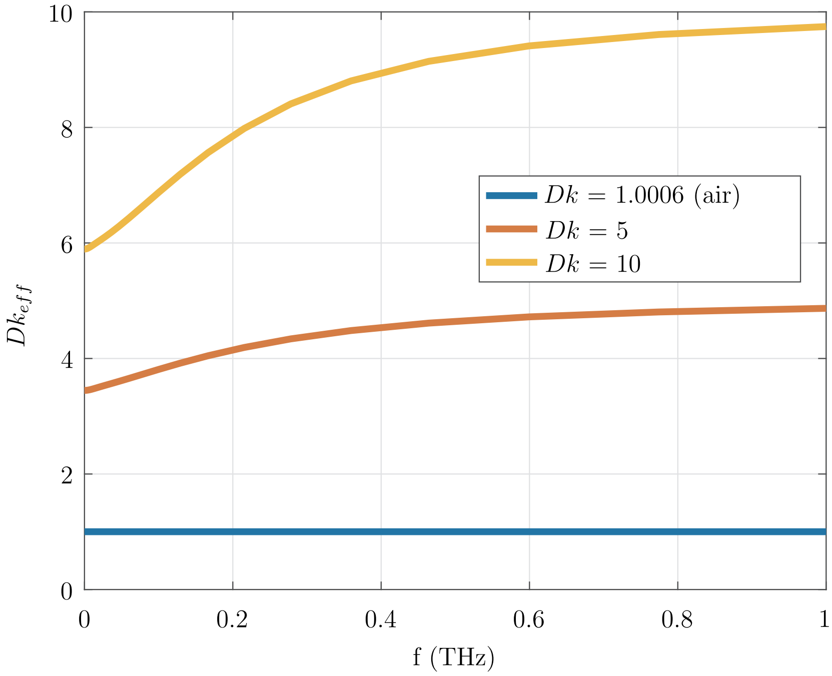


Figure 2.3: Simulations of $Dk$ for MS with Megtron 6

a current in the other conductor. In the case of transmission lines the currents in each conductor have opposite polarity, which causes the currents to be drawn to the surfaces facing each other. For increasing frequencies, this behavior, with a significant skin effect present, is enhanced so that only little current is conducted on the surfaces facing away from the other conductor. This effect also known as proximity effect is very important for transformer designs, as it causes even more losses than the skin effect. The proximity effect is more intricate than the skin effect, because it needs at least two conductors close-by that influence each other.

Fig. 2.3 shows simulations for the dimensions of the manufactured samples up to a frequency of 1 THz. The simulations were carried out for four different $Dk$s of the substrate: 1.0006 (air), 5, and 10. It can be seen that for increasing frequencies there is an asymptotic behavior of the measured $Dk$ reaching the $Dk$ of the substrate only. This shows that for increasing frequencies less and less electromagnetic field (EM-field) is propagating on the top surface of the line i.e. towards the surrounding air. One simulation shows results for a $Dk$ same as air. Within that simulation it makes no difference on which edge of the line most of the current is conducted, which can be verified by a totally flat frequency behavior. It should be noted that for the simulations the substrate height was kept constant at 125 $\mu$m but the line width was adjusted appropriately to achieve 50 $\Omega$ wave impedance.

### 2.2.1 Surface waves

MS and CBCPW lines exhibit an inhomogeneous dielectric stack-up by design. Hence, no perfect TEM mode, but rather an inherent quasi-TEM propagation is tied to it, which may facilitate the propagation of parasitic waves, too. These plane-trapped surface waves are basically comprised of the TM0 and the TE1 mode [12]. While the TM0 mode is possible at every frequency, the TE1 has a cut-off frequency which depends on $Dk$ of the substrate and the line geometry (approximately 20 GHz in the test structures).

### 2.2.2 Analytic approaches for the positive dispersion

In the literature two analytical expressions for the positive dispersion can be found. Both expressions are only valid for MS as CBCPW contains another degree of freedom for the top gap width, which would make an analytical approximation very cumbersome.

The formula proposed in [21] with an accuracy better than 0.6% with parameters in the range of: $0.1 \leq \mathrm{w/h} \leq 100$, $1 \leq Dk \leq 20$, and $0 \leq \mathrm{h}/\lambda_0 \leq 0.13$. The analytical expression is as follows:

$$Dk_{\mathrm{eff,MS}}(f) = Dk - \frac{Dk - Dk_{\mathrm{eff,MS}}(0)}{1 + P(f)} \tag{2.1}$$

This formula uses the following frequency dependent function $P(f)$ to mimic the frequency dependent behavior:

$$P(f) = P_1 P_2[(0.1844 + P_3 P_4) 10 f h]^{1.5763} \tag{2.2}$$

$$\text{with :}$$

$$P_1 = 0.27488 + \left[0.6315 + \frac{0.525}{(1 + 0.157 f h)^{20}}\right] u - 0.065683 \exp(-8.7513 u) \tag{2.3}$$

$$P_2 = 0.33622[1 + \exp(-0.03442 Dk)] \tag{2.4}$$

$$P_3 = 0.0363 \exp(-4.6u)(1 - \exp[-(fh/3.87)^{4.97}]) \tag{2.5}$$

$$P_4 = 1 + 2.751\{1 - \exp[-(Dk/15.916)^8]\} \tag{2.6}$$

$$\tag{2.7}$$

In [22] the author uses a different approach for his dispersion formula to achieve an accuracy better than 0.6% for an even wider range of parameters, i.e. $0.1 \leq \mathrm{w/h} \leq 10$, $1 \leq Dk \leq 128$, and any $\mathrm{h}/\lambda_0$. Although in this case the w/h ratio is narrowed to 10, only very low wave impedances for transmission lines are affected by this constraint. The proposed formula by the author in [22] is as follows:

$$Dk_{\text{eff,MS}}(f) = Dk - \frac{Dk - Dk_{\text{eff,MS}}(0)}{1 + (f/f_{50})^m} \tag{2.8}$$

$$f_{50} = \frac{f_{K,\ TM_0}}{0.75 + \left(0.75 - \frac{0.332}{Dk^{1.73}}\right)\frac{w}{h}} \tag{2.9}$$

$$f_{K,\ TM_0} = \frac{c\ \arctan\left(Dk\sqrt{\frac{Dk_{\text{eff,MS}}(0)-1}{Dk-Dk_{\text{eff,MS}}(0)}}\right)}{2\pi h\sqrt{Dk - Dk_{\text{eff,MS}}(0)}} \tag{2.10}$$

All of these conditions are fulfilled by the manufactured samples and are used for the frequency dependent compensation of $Dk_{\text{eff,MS}}$ in Cha. 4.

### 2.2.3 Visualization of the wave pattern for MS and CBCPW

The electric field patterns for dispersive 50 Ω MS and CBCPW lines on Megtron 6 were simulated for two frequencies (10 MHz and 110 GHz)[1] and 1 W incident power. In these simulations all metals are perfect electrical conductors (PEC) to neglect the decreasing dispersion of $Dk_{app}$. These two frequencies were selected as for low frequencies (e.g. 10 MHz) the positive dispersion is still negligible, however, at 110 GHz it has a significant impact on $Dk_{eff}$. For minimizing errors due to adaptive meshing, for each investigated frequency an optimized mesh was generated. This allows the meshing algorithm to solve as accurate as possible as the field pattern changes significantly for these frequencies.

Fig. 2.4 depicts the two simulations for both frequencies (10 MHz and 110 GHz in Fig. 2.4a and Fig. 2.4b, respectively). It can be noted that for 110 GHz the E-field magnitude rises in the substrate, most prominently below the transmission line and the GND plane. By closer investigation, it can also be seen that the E-field is mainly displaced from the top surface of the line. For in detail investigation of this effect the E-field difference is computed.

Fig. 2.5a shows the difference of the 10 MHz and 110 GHz electric field patterns $E_{abs}$ (see (2.11)) for MS. By this subtraction only the frequency dependent part of the electric field remains. Now it is obvious that the dispersion stimulates mainly by decreasing the electric field at the two top edges of the line, but also at the top surface and displacing it into the substrate, especially right below the line. By observing the equipotential lines (dashed lines), it can be observed that there is a steep field change from a local maximum to a local minimum right on the substrate to air boundary next to the line, displacing the electric field from

[1] utilizing HFSS, Ansys Corporation, Canonsburgh, PA.

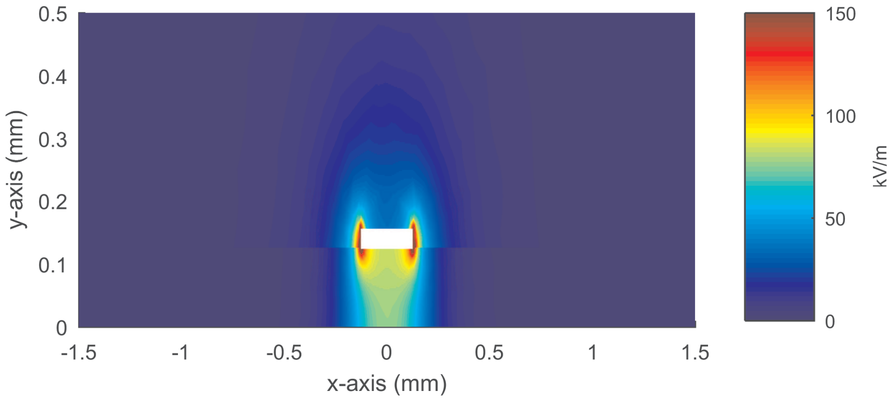


(a)

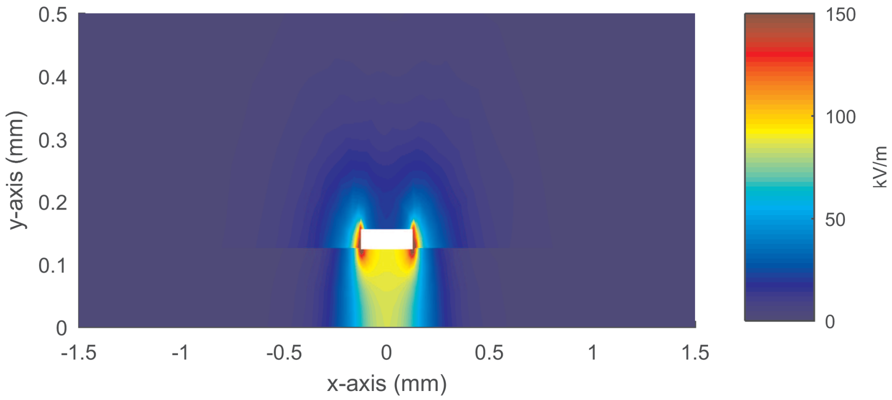


(b)

Figure 2.4: Electric field of MS: (a) Magnitude of electric field at 10 MHz, (b) Magnitude of electric field at 110 GHz

the substrate into the air (contrary to the aforementioned decrease of the electric field above the line). This surprising behavior shows that not only an increase of $Dk_{eff}$ over frequency happens but also a slight decrease. However, the overall trend suppresses this decrease and it is not noticeable for the overall $Dk_{eff}$. The relative changes of the electric field $E_{rel}$ (see (2.12)) in Fig. 2.5b exhibit that the electric field has the highest relative changes several line widths away from the line, in the substrate and at the substrate to air boundary.

$$E_{abs} = |E|_{110\text{ GHz}} - |E|_{10\text{ MHz}} \tag{2.11}$$

$$E_{rel} = \frac{|E|_{110\text{ GHz}} - |E|_{10\text{ MHz}}}{|E|_{10\text{ MHz}}} \tag{2.12}$$

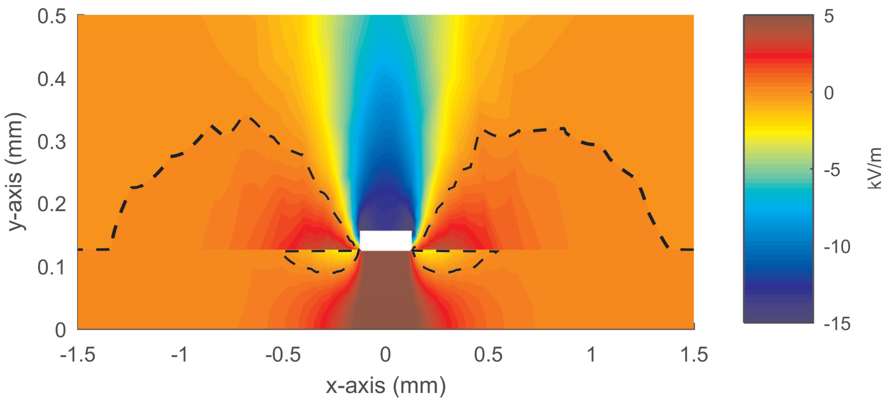


(a)

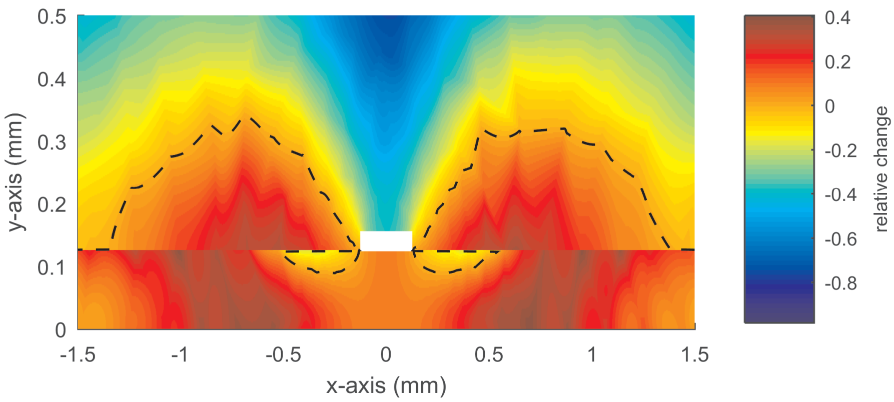


(b)

Figure 2.5: Electric field of MS: (a) Absolute difference of electric field magnitude, (b) Relative difference of electric field magnitude

Fig. 2.6a and Fig. 2.6b display the simulation results for the dispersive electric field behavior for CBCPW. The simulations were carried out in a similar manner as for MS (PEC metals simulated at 10 MHz and 110 GHz). On first sight the the same behavior can be observed as for MS with the main displacement of the E-field into the substrate and the main conclusions drawn for MS are valid for CBCPW as well. However, for CBCPW the field in the gap between line and top ground is decreased considerably as can be seen for the absolute and the relative change of the electric field (Fig. 2.7a and Fig. 2.7b). In contrast to MS where the electric field of the dispersive behavior extends to several line widths apart from the actual line, in CBCPW the highest relative increase of the field occurs at the bottom corner of the ground plane and the via.

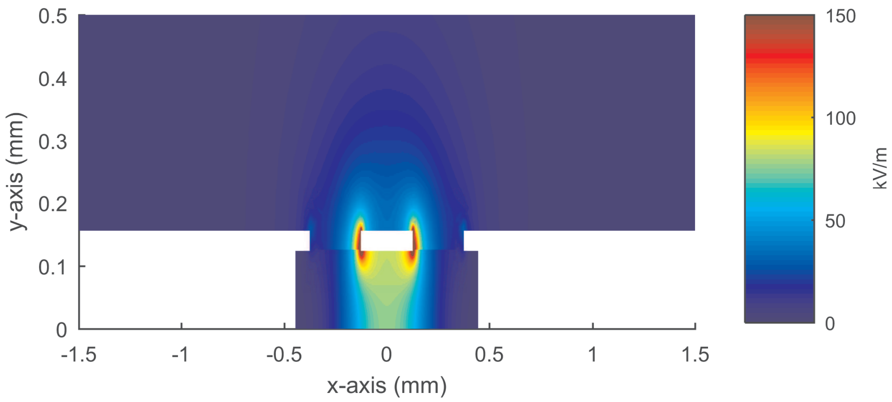


(a)

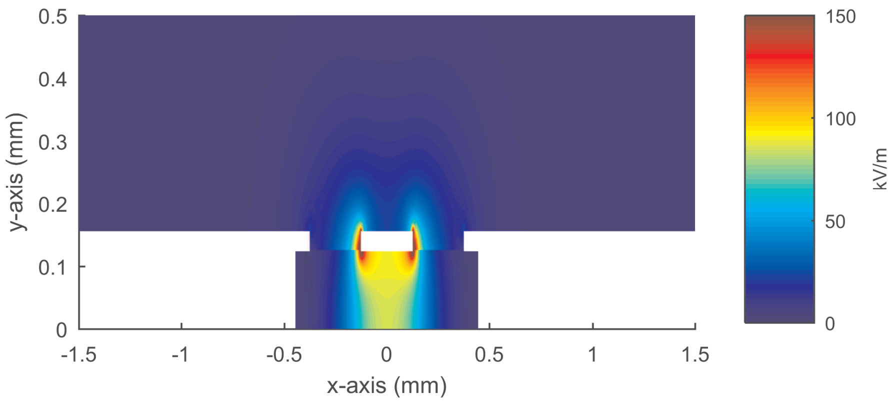


(b)

Figure 2.6: Electric field of CBCPW: (a) Magnitude of electric field at 10 MHz, (b) Magnitude of electric field at 110 GHz

### 2.2.4 Conclusions

Within this section the physical causes of the positive dispersion behavior for MS and CBCPW were discussed and backed by simulations. These simulations have shown that the electric field for increasing frequencies of MS and CBCPW do not only crowd within the substrate, as widely assumed, but also on top of the substrate next to the lateral faces of the line in air. This contrary reaction of displacing E-field into the air does not alter the overall increasing dispersive behavior of $Dk_{eff}$. The major part of electric field is in both cases displaced from the top surface of the line to the surfaces facing the conductor of different polarity.

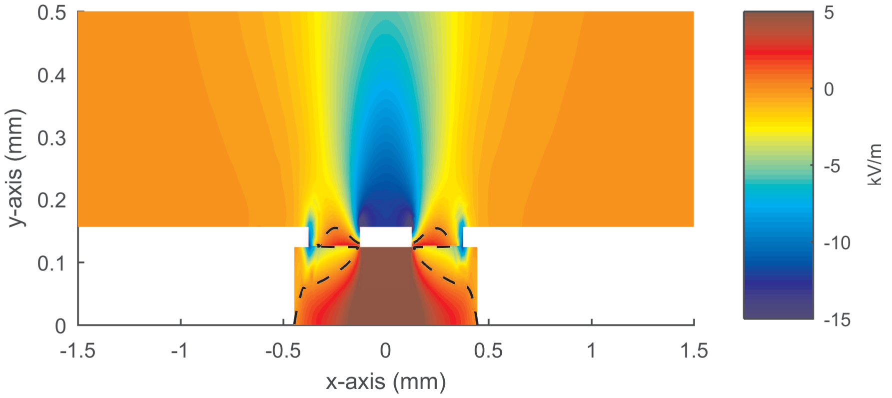


(a)

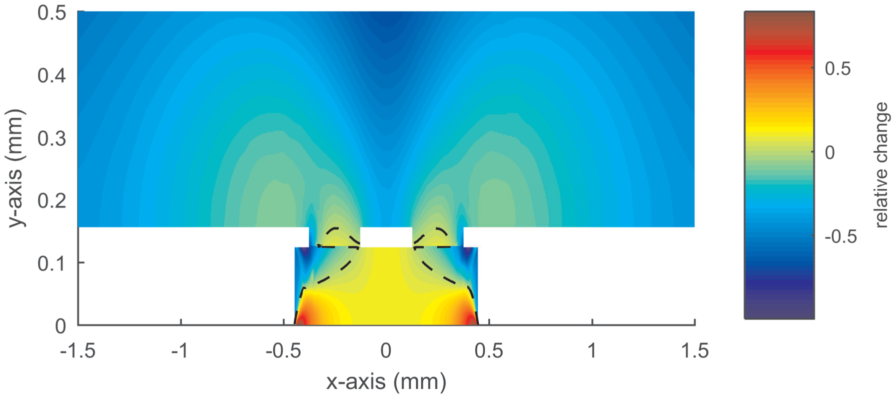


(b)

Figure 2.7: Electric field of CBCPW: (a) Absolute difference of electric field magnitude, (b) Relative difference of electric field magnitude

## 2.3 Negative dispersion of the measured $Dk$

Within this section the negative dispersion behavior is discussed in detail, for a brief summary of these findings refer to [23]. For explaining the negative dispersion behavior of the measurements up to approximately 20 GHz it is necessary to take a step back and focus on the complex propagation constant $\gamma$ first (please refer also to Sec. 1.3.1). The real part or the attenuation constant $\alpha$ contains the loss of the transmission line. The imaginary part of $\gamma$, or the phase factor $\beta$, includes the underlying dielectric behavior that contains the permittivity of the applied substrate. The complex propagation constant can be described by a lumped element transmission line RLCG-model for every transmission line. In this work the RLCG model is introduced with a per unit length (pul) representation i.e. the resistance pul R', the inductance pul L', the capacitance pul C', and conductivity pul G'. It is important to mention that the lossy elements of the RLCG-model (R' and G') contribute to the behavior of $\alpha$ and $\beta$, and not only to $\alpha$. This will be clearer after the subsequent mathematical derivations.

For $\gamma$, a clever factorization by using and RLCG model can be carried out as follows (with $\omega = 2\pi f$):

$$\begin{aligned}\gamma = \alpha + j\beta &= \sqrt{(R' + j\omega L')(G' + j\omega C')}\\ &= \sqrt{(j\omega L')(j\omega C')(1 + \frac{R'}{j\omega L'})(1 + \frac{G'}{j\omega C'})}\\ &= j\omega\sqrt{L'C'}\sqrt{1 + \frac{R'}{j\omega L'}}\sqrt{1 + \frac{G'}{j\omega C'}}\end{aligned} \tag{2.13}$$

Noticeable is already that a real $\sqrt{L'C'}$-factor impacts all real and imaginary factors, which can be interpreted as changing the magnitude of the complex vector. This factorization will be taken as a starting point for a frequency independent and a frequency dependent investigation.

### 2.3.1 Derivation of $\gamma$ for frequency independent RLCG

In this section a frequency independent RLCG-model is assumed, which facilitates quick results for a first glimpse if there is an inherent frequency dependency for $\gamma$ that would explain the decreasing behavior.

If we focus on low loss transmission lines, by assuming $R \leq \omega L$ and $G \leq \omega C$, the square root behavior in (2.13) can be approximated by a Taylor series at 0 (i.e. a Maclaurin series) in the following manner:

$$\gamma = j\omega\sqrt{(L'C')}\Big(1 + \frac{1}{2}\frac{R'}{j\omega L'} + \frac{1}{8}\frac{R'^2}{\omega^2 L'^2} + \dots\Big)\Big(1 + \frac{1}{2}\frac{G'}{j\omega C'} + \frac{1}{8}\frac{G'^2}{\omega^2 C'^2} + \dots\Big) \tag{2.14}$$

Eqn. 2.14 can be easily split into a real and a imaginary part:

$$\alpha_{LowLoss} \approx \frac{1}{2}\Bigg[\sqrt{\frac{L'}{C'}}G' + \sqrt{\frac{C'}{L'}}R' + \frac{1}{8\omega^2\sqrt{LC}}\Big(\frac{RG^2}{LC} + \frac{R^2G}{L}\Big)\Bigg] \tag{2.15}$$

$$= \hat{A}_\alpha + \frac{\hat{B}_\alpha}{\omega^2} \tag{2.16}$$

$$\beta_{LowLoss} \approx \omega\sqrt{(L'C')}\Bigg[1 + \frac{1}{8\omega^2}\Bigg(\Big(\frac{G'}{C'} - \frac{R'}{L'}\Big)^2 + \frac{1}{8}\Big(\frac{R'G'}{\omega L'C'}\Big)^2\Bigg)\Bigg] \tag{2.17}$$

$$= \omega\hat{A}_\beta \pm \frac{\hat{B}_\beta}{\omega} + \frac{\hat{C}_\beta}{\omega^3} \tag{2.18}$$

It can be seen that $\alpha_{LowLoss}$ for a frequency independent RLCG would have a decreasing behavior, what can be considered as an unphysical behavior which is not observed in measurements (cmp. Fig. 1.15a and Fig. 1.16a).

For $\beta_{LowLoss}$, it is more intricate to approximate the frequency behavior as it depends on the values of RLCG. Interesting to note is that for the Heaviside condition (G'/C' = R'/L'), the second factor $\hat{B}_\beta$ would be zero but the frequency dependence remains. For the case when G' < C' and R' < L' is assumed (only focusing on the order of magnitude not the units), a low loss assumption in a stricter sense, $\beta_{LowLoss}$ would only have a linearly increasing behavior. This would match to some point the behavior of Sec. 2.2, however, it should be kept in mind that this represents only a special case for close to superconductive metals. Additionally, none of the effects (proximity effect and surface waves) are included in this representation and thus it is unphysical again.

It can be summed up that for a frequency independent RLCG model, none of the measured behavior can be explained. The next section extends the model to a frequency dependent RLCG model.

### 2.3.2 Frequency behavior of extended RLCG-model

In this section each element of the RLCG-model will be extended by a physically backed frequency dependence. The inductance can be described as the sum of internal and external inductance $\mathrm{L}' = \mathrm{L}'_{\mathrm{int}} + \mathrm{L}'_{\mathrm{ext}}$ [24]. Whereby only $\mathrm{L}'_{\mathrm{int}}$ has a frequency dependence $\mathrm{L}'_{\mathrm{int}} \approx R'/\omega$. $\mathrm{L}'_{\mathrm{ext}}$ is assumed constant because any frequency dependence caused by the proximity effect (see [25]) is taken care of by the formulas introduced in Sec. 2.2.2. The resistance $R'$ increases by $\sqrt{f/f_0}$ for $f > f_0$ which is based on the "break-point" method [26]. For frequencies below $f_0$ ($\delta \gg w, t$), $R'$ shows a constant value $R'_{DC}$ (with skin depth $\delta$, conductor width $w$, and conductor thickness $t$). For frequencies above $f_0$ ($\delta \ll w, t$) the typical $\sqrt{f}$-behavior is assumed. The conductance $G'$ is supposed to increase linearly

[17]. It should be pointed out that the surface roughness is not explicitly taken into account within this model. The overall frequency dependent RLCG-model looks as follows:

$$R'(f) = \begin{cases} R'_{DC}, & f < f_0 \\ R'_{DC}\sqrt{f/f_0}, & f > f_0 \end{cases} \tag{2.19a}$$

$$L'(f) = L_{int}(f)' + L'_{ext}, \qquad L_{int}(f)' \approx \frac{R'(f)}{\omega} \tag{2.19b}$$

$$C'(f) = C' \tag{2.19c}$$

$$G'(f) = G'_{DC} + k'_G f \tag{2.19d}$$

### 2.3.3 Derivation of $\gamma$ for frequency dependent RLCG

Let's start again with (2.13), however, this time the frequency dependent RLCG-model is used:

$$\gamma = \alpha + j\beta = j\omega \underbrace{\sqrt{L'(f)C'}}_{I} \underbrace{\sqrt{1 + \frac{G'(f)}{j\omega C'}}}_{II} \underbrace{\sqrt{1 + \frac{R'(f)}{j\omega L'(f)}}}_{III} \tag{2.20}$$

Eqn. 2.20 was split into three factors *I-III* for easier investigation. By inserting (2.19a)-(2.19d) into (2.20), the frequency dependence of each factor can be computed (for $f > f_0$):

$$\begin{aligned} I: \quad \sqrt{L'(f)C'} &= \sqrt{\frac{R'_{DC}C'}{2\pi\sqrt{f_0}} \frac{1}{\sqrt{f}} + L'_{ext}C'} \\ &= \sqrt{L'_{ext}C'} \sqrt{1 + \frac{R'_{DC}}{2\pi L'_{ext}\sqrt{f_0}} \frac{1}{\sqrt{f}}} \end{aligned} \tag{2.21}$$

For the second factor a low loss assumption for the capacitance and the dielectric loss is introduced as $G'_{DC} + k'_G f < \omega C'$. For $f \gg 0$, $G'_{DC}$ should be negligible and the assumption simplifies to $k'_G < C'$. Now a Taylor approximation can be expressed as:

$$\begin{aligned} II: \quad \sqrt{1 + \frac{G'(f)}{j\omega C'}} &= \sqrt{1 + \frac{G'_{DC} + k'_G f}{j\omega C'}} \\ = 1 + \frac{1}{2j} \frac{G'_{DC} + k'_G f}{\omega C'} &+ \frac{1}{8} \Big( \frac{G'_{DC} + k'_G f}{\omega C'} \Big)^2 + \dots \end{aligned} \tag{2.22}$$

The third factor, containing the resistance and the inductance, has a slightly more intricate frequency behavior (shown for $III^2$ and $f > f_0$):

$$
\begin{aligned}
III^2: \quad 1+\frac{R'(f)}{j\omega L'(f)} &= 1+\frac{R'_{DC}\sqrt{\frac{\omega}{\omega_0}}}{j\omega\left(\frac{R'_{DC}}{\omega}\sqrt{\frac{\omega}{\omega_0}}+L'_{ext}\right)} \\
&= 1+\frac{R'_{DC}\sqrt{\frac{\omega}{\omega_0}}}{j\sqrt{\omega}\frac{R'_{DC}}{\sqrt{\omega_0}}+j\omega L'_{ext}} = 1+\frac{R'_{DC}\sqrt{\omega}}{j(R'_{DC}\sqrt{\omega}+\omega\sqrt{\omega_0}L'_{ext})} \\
&= 1+\frac{1}{j(1+\frac{2\pi\sqrt{f_0}L'_{ext}}{R'_{DC}}\sqrt{f})} = 1+\frac{1}{j(1+K\sqrt{f})} \qquad (2.23)
\end{aligned}
$$

It can be comprehended that $\mathrm{III}^2$ is a complex rational function. For providing easier readability a frequency independent factor K is introduced. As only positive definite variables are multiplied, K is also positive definite.

A common definition for $R'_{DC}$ is $1/(\sigma w t)$ for a rectangular cross section of the line (with line width $w$, conductivity $\sigma$, and line thickness t). $f_0$ can be represented for a rectangular line as $4/(\pi\mu\sigma t^2)$. At that frequency the skin depth equals half of the line thickness (with the permeability of the line material $\mu$). By combining these geometric simplifications, the range of $K$ for rectangular lines can be expressed as follows:

$$
K = \frac{2\pi\sqrt{f_0}L'_{ext}}{R'_{DC}} \qquad (2.24)
$$

$$
= \sqrt{\frac{4}{\pi\mu\sigma t^2}}2\pi L'_{ext}\sigma w t = \frac{4\pi L'_{ext}\sigma w t}{\sqrt{\pi\mu\sigma t^2}} = \sqrt{\frac{\pi\sigma}{\mu}}4L'_{ext}w \qquad (2.25)
$$

For an MS line with $u = w/h$ varying within 0.1 to 10, $L'_{ext}$ varies approximately in between 0.1 H/m to 1 H/m. For the lines shown in this paper, assuming pure copper, $K$ varies in between $0\,\mathrm{s}^{-0.5}$ to $0.005\,\mathrm{s}^{-0.5}$. Even for such a small $K$ the frequency dependent part of the denominator in (2.23) starts to dominate already for frequencies above 40 kHz.

The third factor only needs to fulfill $0 \leq K\sqrt{f}$ (which is true in any case), to be approximated by a Taylor series as follows:

$$
\begin{aligned}
III: \sqrt{1+\frac{R'(f)}{j\omega L'(f)}} &= \sqrt{1+\frac{1}{j(1+K\sqrt{f})}} \\
&= 1+\frac{1}{2j}\frac{1}{1+K\sqrt{f}}+\frac{1}{8}\frac{1}{(1+K\sqrt{f})^2}+\dots \qquad (2.26)
\end{aligned}
$$

By combining (2.21), (2.22), and (2.26) an approximation for the complex $\gamma$ can be expressed as follows:

$$\gamma(f)_{LowLoss} = j\omega\sqrt{L'_{ext}C'}\sqrt{1+\frac{1}{K\sqrt{f}}}$$
$$\left(1+\frac{1}{2j}\frac{G'_{DC}+k'_G f}{\omega C'}+\dots\right)\left(1+\frac{1}{2j}\frac{1}{1+K\sqrt{f}}+\dots\right) \tag{2.27}$$

### 2.3.4 Expressions for the attenuation and phase constant

Closed form expressions for $\alpha(f)_{LowLoss}$ and $\beta(f)_{LowLoss}$ can now be stated as:

$$\alpha(f)_{LowLoss} = \Re\{\gamma\}$$
$$\approx \frac{\omega}{2}\sqrt{L'_{ext}C'}\sqrt{1+\frac{1}{K\sqrt{f}}}\left(\frac{G'_{DC}+k'_G f}{\omega C'}+\frac{1}{1+K\sqrt{f}}\right) \tag{2.28}$$
$$\beta(f)_{LowLoss} = \Im\{\gamma\}$$
$$\approx \omega\sqrt{L'_{ext}C'}\sqrt{1+\frac{1}{K\sqrt{f}}}\left(1-\frac{1}{4}\frac{G'_{DC}+k'_G f}{(1+K\sqrt{f})\omega C'}\right) \tag{2.29}$$

Another Taylor approximation is applied to the first factor (real function) of $\alpha(f)_{LowLoss}$ to continue the evaluation:

$$\alpha(f)_{LowLoss} \approx \pi f\sqrt{L'_{ext}C'}$$
$$\left(1+\frac{1}{2}\frac{1}{K\sqrt{f}}-\frac{1}{8}\frac{1}{K^2 f}+\dots\right)\left(\frac{G'_{DC}+k'_G f}{\omega C'}+\frac{1}{1+K\sqrt{f}}\right)$$
$$\approx \pi\sqrt{L'_{ext}C'}\left(\frac{G_{DC}{}'}{2\pi C'}+\frac{1}{K^2}+\frac{1}{K}\left(1+\frac{k'_G}{4\pi C'}\right)\sqrt{f}+\frac{k'_G}{2\pi C'}f\right)$$
$$\Rightarrow \alpha(f)_{LowLoss} \overset{!}{\approx} \hat{X}_\alpha\sqrt{f}+\hat{Y}_\alpha f \tag{2.30}$$

Eqn. 2.30 shows that any attenuation constant $\alpha(f)$ for low loss lines can be LS-fitted by just two terms, a linearly increasing term and a square root term. Applying these results to the measurements shown in Fig. 1.15a and Fig. 1.16a, (2.30) has a coefficient of determination of better than 0.99 for all measurements.

The frequency behavior of the phase constant $\beta(f)$ for low loss lines can also be expressed by two coefficients $\hat{X}_\beta$ and $\hat{Y}_\beta$ (utilizing $\beta_0 = \omega/c_0$):

$$\begin{aligned}
Dk_{app} &= \left(\frac{\beta(f)_{LowLoss}}{\beta_0}\right)^2 \\
&\approx c_0^2 L'_{ext} C' \left(1 + \frac{1}{K\sqrt{f}}\right)\left(1 - \frac{1}{4}\frac{G'_{DC} + k'_G f}{(1+K\sqrt{f})\omega C'}\right)^2 \\
&= c_0^2 L'_{ext} C' \left(1 + \frac{1}{K\sqrt{f}}\right)\left[1 - \frac{k'_G}{4\pi C'}\frac{1}{1+K\sqrt{f}} + \mathcal{O}\left(\frac{1}{f}\right)\right] \\
&= c_0^2 L'_{ext} C' \left(1 + \frac{1}{K\sqrt{f}} - \frac{k'_G}{4\pi C'}\frac{1}{1+K\sqrt{f}} + \mathcal{O}\left(\frac{1}{f}\right)\right] \\
&\approx c_0^2 L'_{ext} C' \left(1 + \left[1 - \frac{k'_G}{4\pi C'}\right]\frac{1}{K\sqrt{f}}\right) \qquad (2.31)
\end{aligned}$$

$$\Rightarrow Dk_{app} \overset{!}{\approx} \frac{\hat{X}_\beta}{\sqrt{f}} + \hat{Y}_\beta \qquad (2.32)$$

The low loss assumption used for (2.22) is once more of importance in (2.31) as otherwise $Dk_{app}$ would converge to $c_0^2 L'_{ext} C'$ by an increasing $1/\sqrt{f}$-behavior over frequency. For low loss materials, it is interesting to note that the starting value of the $1/\sqrt{f}$-term mainly depends on $1/K$. So it tends to be higher for lines made of materials with smaller conductivities and higher permeabilities (2.25).

One fit for actual MS measurements with Megtron 6 is depicted in Fig. 2.8. The largest deviation from the fit occurs at the highest frequencies of $Dk_{app}$, however, in general excellent agreement is achieved by the proposed fitting. Although the surface roughness was not taken into account explicitly in the RLCG-model, it seems that the proposed approximation models it sufficiently well. This leads to the conclusion that the surface roughness can be mimicked in this case also by a $1/\sqrt{f}$-behavior.

## 2.4 Simulations of positive and negative dispersion

After an in detail discussion of the positive and negative dispersion behavior separately, in this section the full dispersion will be simulated at once and compared with measurements. The measured mean values of $Dk_{app}$ for MS and CBCPW and simulation results are shown in Fig. 2.9a and Fig. 2.9b. Within these plots the simulation results from the previous section (Sec. 2.2.3) are termed "simulated with PEC". For frequencies > 20 GHz the simulations have close agreement with measurements. The PEC simulations show a flat behavior for f < 20 GHz

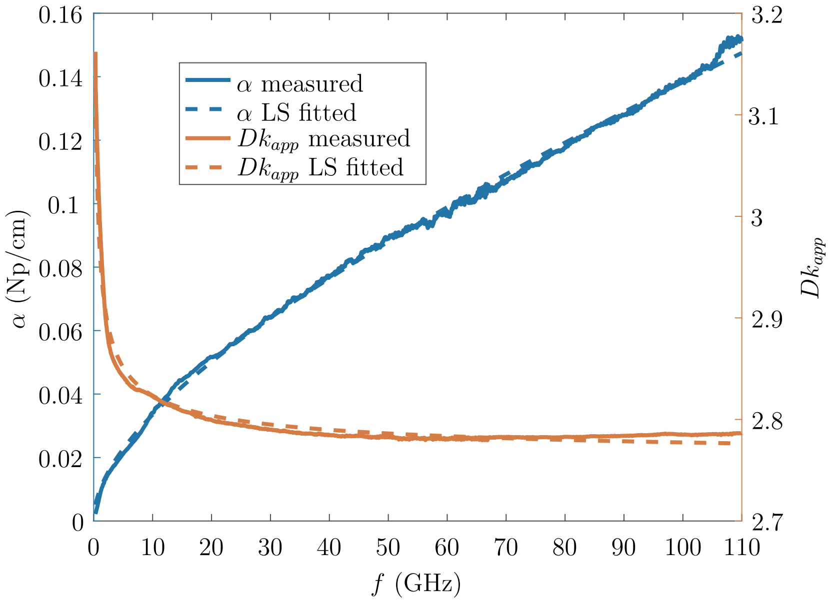


Figure 2.8: Least-Squares fit of Megtron 6 MS measurements with (2.30) and (2.32)

as any impact of the skin effect is neglected as the interior of the PEC line is free of any electromagnetic field.

When the material of the line is changed to copper, the decreasing internal inductance as well as the increasing resistance over frequency is included in simulations which shows a steep decreasing behavior at low frequencies. By decreasing the conductivity $\sigma$ of copper, an increased impact of the skin effect can be noticed. A valid assumption is that the applied copper in PCB manufacturing shows less conductivity than chemically pure copper. Further improvements in approaching the measurements are achieved, by adding in the simulation a layered impedance boundary. This impedance boundary tries to mimic the impact of surface roughness. The thickness is set at $3\,\mu$m as the manufacturer states a surface roughness approximately at that value. These variations were carried out for MS and CBCPW.

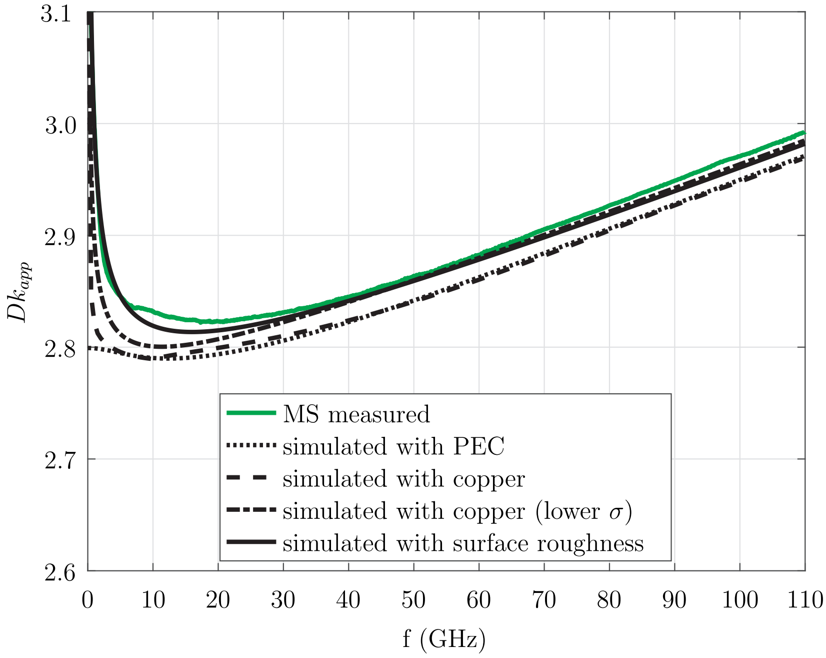


(a)

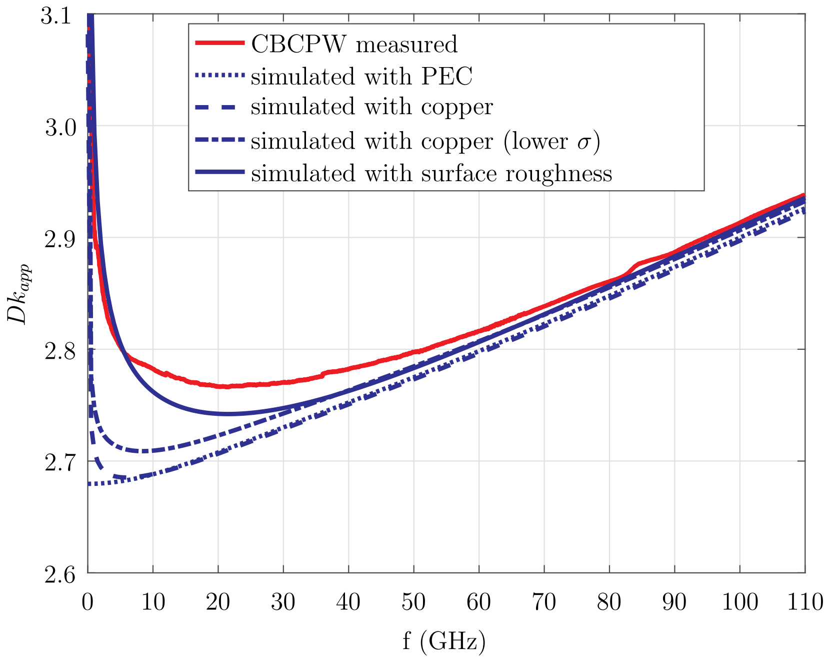


(b)

Figure 2.9: Comparison of measured and simulated $Dk_{app}$: (a) MS, (b) CBCPW

## 2.5 Conclusion

This chapter has shown and explained the positive and negative dispersion effects occurring in the measurement. For broadband characterization it is essential to take into account dispersive effects. The introduced analytic closed-form expression for the negative dispersion is applicable to any low loss dielectric characterization with transmission lines and is not limited to MS or CBCPW. It avoids highly meshed simulations which are otherwise necessary to mimic EM-behavior in the conductors itself. With the introduced formula for negative dispersion and the formulas taken from literature for positive dispersion it is possible to compensate the dispersive behavior for the prominent MS transmission line easily.

# Chapter 3

# Measurement uncertainties

Within this section the uncertainties of the proposed measurement method for determining the dielectric parameters for MS and CBCPW transmission lines are computed. The measurement procedure contains two sources of uncertainty. There is on the one hand the uncertainty of the measurement equipment and on the other the uncertainty of the manufacturing process which relates to all the samples.

These uncertainty sources affect directly the S-parameter measurements for the TRL-calibration and so all subsequent computations. As the uncertainties propagate in a non-trivial manner through the whole measurement procedure and calculations, a Monte Carlo simulation is implemented for computing the overall uncertainty. Fig. 3.1 shows all stages of the Monte Carlo simulation. The left side of Fig. 3.1 shows the two sources of uncertainty that deteriorate already the measurements carried out for the TRL-calibration, and thus all subsequent stages. The S-parameters after the TRL-calibration are processed to obtain the measured $Dk$ or $Dk_{app}$. The next step is the compensation of the positive dispersion by means of the introduced analytic formulas of Sec. 2.2.2. The next step in the Monte Carlo chain compensates the conductor properties (the negative dispersion) with the closed-form expression (2.32) derived and introduced in Sec. 2.3. The last step of the simulation computes the $Dk$ of the substrate material. The utilized formulas in the last step are explained in this chapter in Sec. 3.6.

This chapter investigates each step of the Monte Carlo simulation in detail and provides information about the underlying assumptions. All of the presented statistics are based on 25000 runs.

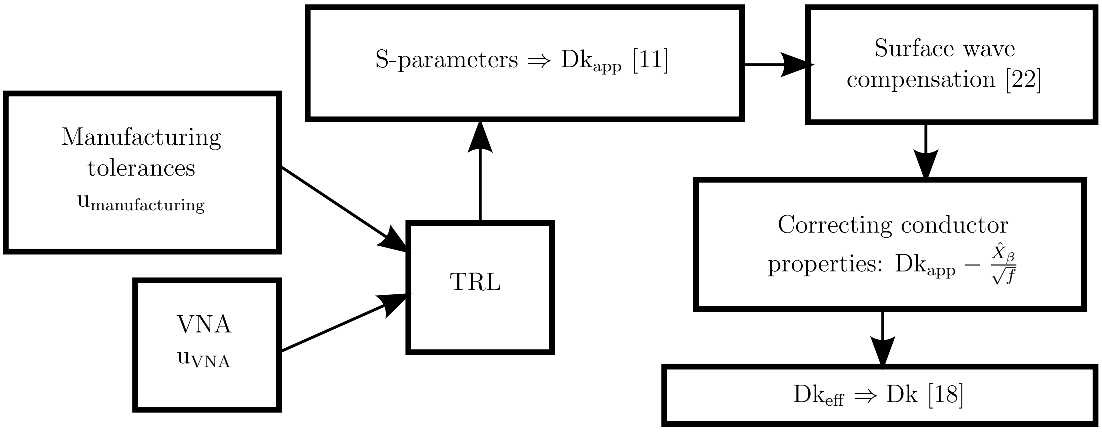


Figure 3.1: Monte Carlo simulation chain

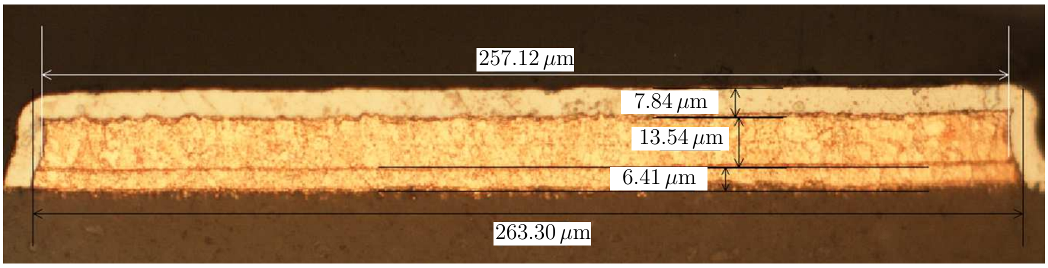


Figure 3.2: Microsection

## 3.1 Manufacturing process uncertainties

The measurement samples were manufactured with a commercial wet-etch process (see also Sec. 1.4). The benefit of this process is that huge patches can be manufactured at relatively low cost. On the downside, there are tolerances of up to ± 20% tied to this process for the smallest dimensions of a few micrometers. For getting an estimate of how much the dimensions of the measured samples were actually deviating from the nominal dimensions, several microsections were processed. An example for a microsection is shown in Fig. 3.2. In total eleven microsections are used to compute the first moment and the second central moment, the mean and the variance, respectively. The microsections were carried out subsequently to the measurements as it represents a destruction of the samples.

The etch rate of the underlying wet etch process is assumed to be normally distributed, which leads to normally distributed manufacturing deviations. The mean values and variances $u_{manufacturing}$ of the manufacturing process are determined by evaluating the microsections of the test boards on different cut planes. The dimensions that are taken into account for the simulation are: the transmission line width, the substrate thickness, the copper thickness, and deviations of the launching pad dimensions (two line widths).

There is one more important deviation that has to be taken into account which is the probing offset. Each time the probes conduct a measurement they are not placed perfectly at the same absolute distance to each other, not even for the very same test structure. This deviation does directly impact the measurements of the $Dk$ as the measured phase depends on the line length. For the probing offset the distribution is assumed to be uniform. The probe placement along the launching pad has no overall salient spot that tends to be probed with a higher probability. Depending on small debris on the surface, the probe was placed closer to the end or to the beginning of the launching pad. There is in total a length of $120\,\mu$m for the probe to make contact to the test board. However, the first $20\,\mu$m are negligible because the probe needs a certain over-travel to achieve good connection which narrows the probing length down to $100\,\mu$m.

The distributions of these parameters for the Monte Carlo simulation are shown in Fig. 3.3a to Fig. 3.3f. Due to the high number of runs for the simulation, each parameter shows close agreement to the proposed statistical distribution. Within the plotted histograms, the number of bins was taken in a way to show the distribution over the whole range of the x-axis. This consequently leads to the same probabilities in each plot, except for the uniformly distributed probing offset.

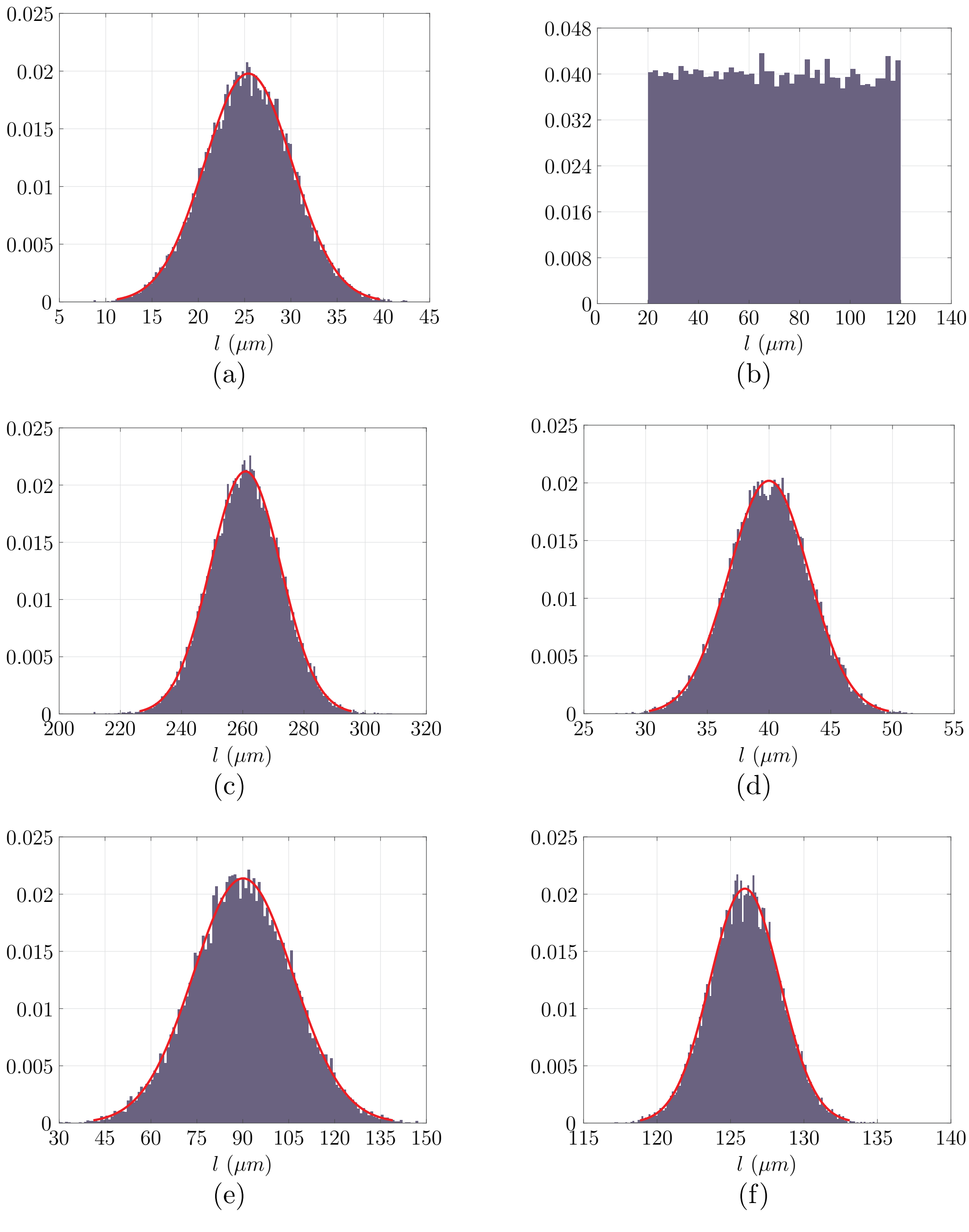


Figure 3.3: Evaluated manufacturing uncertainties for Monte Carlo investigation: (a) copper thickness (b) probing offset (c) line width (d) launching pad line width 1 (e) launching pad line width 2 (f) substrate thickness

## 3.2 VNA uncertainties

The VNA manufacturer provides uncertainties $\mathrm{u_{VNA}}$ of each specific VNA with a coverage factor $k$ of 2 and in compliance with [27]. In this case $\mathrm{u_{VNA}}$ is called the expanded uncertainty (with the random variable $X$ and the combined standard uncertainty or estimated standard deviation $u_c(X)$):

$$u_{VNA} = ku_c(X) \tag{3.1}$$

The coverage factor has to be taken into account for all evaluations to avoid overestimating the uncertainties of the VNA.

Although this information suffices for estimating the uncertainties of the basic VNA, no information can be obtained for the uncertainties in combination with the external down converters that are used to reach 110 GHz. As the converters are increasing the frequency range of the basic VNA from 67 GHz up to 110 GHz (i.e. a maximum of 43 GHz), the worst-case VNA uncertainty could be taken from the frequency range 24 GHz to 50 GHz. Although the added uncertainty of the external down converter is unknown, it is certain that it increases the overall measurement uncertainty. For that reason, the uncertainties stated by the manufacturer in the 50 GHz to 67 GHz frequency range are taken for all measured frequencies. This should take care of the added uncertainty of the converter and state an overall worst-case uncertainty for the proposed measurement method.

Fig. 3.4a depicts the uncertainty of VNA measurements for the reflection loss. It can be noticed that in the center of the Smith chart the magnitude error is the smallest, however, the phase error reaches up to 20°. This behavior changes when moving towards the circumference of the Smith chart where the magnitude error increases steadily and the phase error drops to values close to 1°. By recalling Fig. 1.13a, it can be comprehended that certain measurement points reach reflection losses as low as 0.003 (linear) which leads to high phase uncertainty at these frequencies.

In Fig. 3.4b the uncertainty of the transmission loss is presented (note that this plot is as usual in dB). The transmission loss shows steeply increasing uncertainty for very high losses in magnitude and phase. As the investigation within this thesis is based on low loss transmission lines, this uncertainty should not have much impact on the overall uncertainty (compare Fig. 1.14a wherein the worst-case loss is $-8.3$ dB for the uncalibrated measurements).

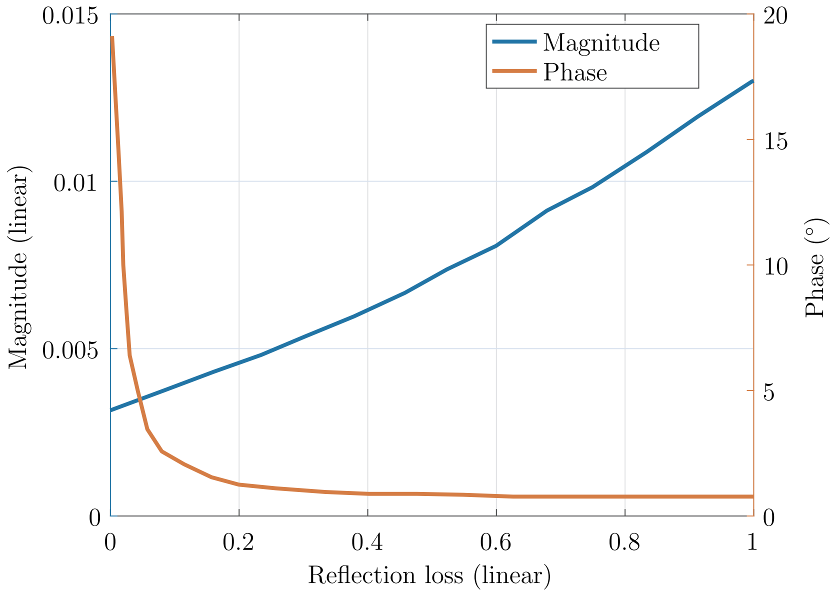


(a)

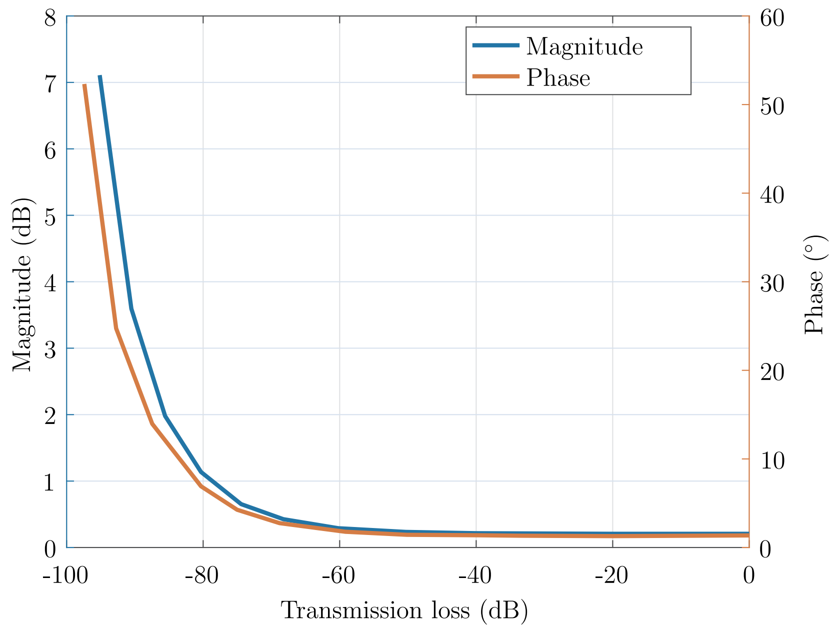


(b)

Figure 3.4: VNA uncertainties (for a frequency range of 50 GHz to 67 GHz): (a) Reflection loss (b) Transmission loss

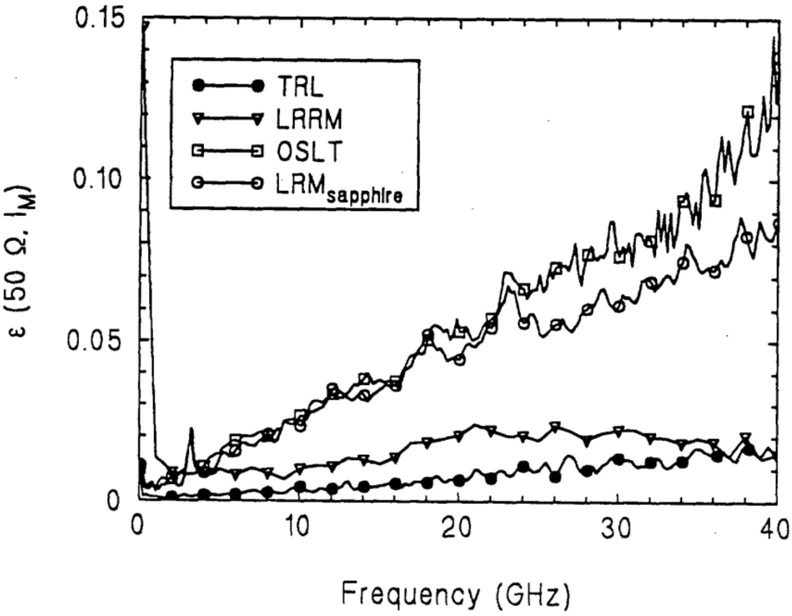


Figure 3.5: LRRM uncertainties [15]

## 3.3 LRRM-calibration errors

The advantages of the LRRM calibration over any other wafer prober calibration was already outlined in Sec. 1.6.1. In Fig. 3.5 the results of a study of the National Institute of Standards and Technology (NIST) is shown. Within this study four different calibration methods were evaluated and it can be seen that TRL and LRRM show similar performance. This figure plots the worst case deviation in the absence of measurement errors. The deviation plot uses the measurement of the proposed calibration method (e.g. TRL) in difference with the actual S-parameters of an passive device measured with respect to a $50\,\Omega$ calibration at the reference plane position $l_m$. This comparison shows the highest deviation for LRRM at approximately 26 GHz of about 0.02. Within the following Monte Carlo simulation the maximum deviation of the LRRM calibration is taken and extended over the whole measured frequency range. This approach was taken to achieve worst case results with the simulation.

## 3.4 TRL-calibration

The modeling and simulation of the TRL calibration standards was done in NI AWR Design Environment. The model contains a simplified version of the launching pads. For the simplified model each line section is treated independently, i.e.

the coupling between elements are not taken into account. By neglecting the couplings of the elements the run time of the Monte Carlo simulation was sped up significantly. The model contains now only closed-form line elements. This kind of element needs the length of the line and the cross-sectional dimensions. The computation of the S-parameters is carried out with an algebraic formula. Utilizing this model in a scripted manner allows the Monte Carlo simulation to finish 25000 runs within a reasonable time. This makes a crucial difference compared to the initial discussion in Sec. 1.6.2 where for each set of parameters a 3D-simulation was carried out. Although not all effects of the actual launching pads are mimicked perfectly with this approach, the modeled TRL calibration standards achieve good agreement with the corresponding measurements as will be shown shortly. The TRL calibration is computed with two different line elements with different lengths. The lengths are selected in a manner to match the investigated frequency range.

Fig. 3.6a to Fig. 3.6d show the simulation results of the reflection loss for each TRL calibration standard compared with measurements. For the simulated model, the mean value dimensions are taken from microsections. The dimensions are all kept constant within the modeling of all calibration standards, only the probing offset was adjusted independently. It can be noted that in the measurements there is an impedance mismatch superimposed on the reflection loss measurement. This curly behavior in the Smith chart can be computed to have a resonance frequency of about 600 MHz. This resonance can be attributed to a small calibration residual of the LRRM calibration as the wavelength computes to about the distance in between the two down-converters.

Fig. 3.7a to Fig. 3.7d depict the results for the insertion loss. It can be noted that there is again good agreement of the simulated model with the measurements.

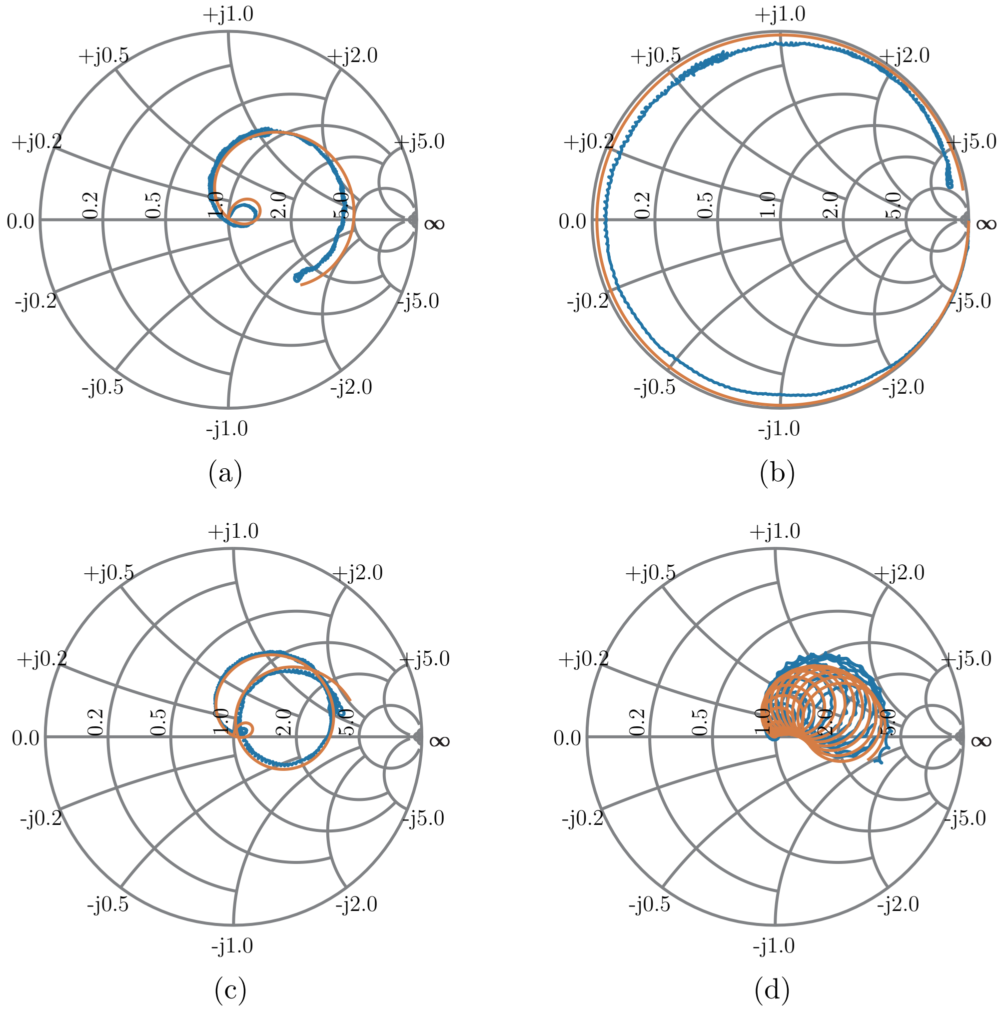


Figure 3.6: Comparing measured reflection loss (blue) with simulated one (orange) for Monte Carlo simulation: (a) thru (b) open (c) line 1 (d) line 2

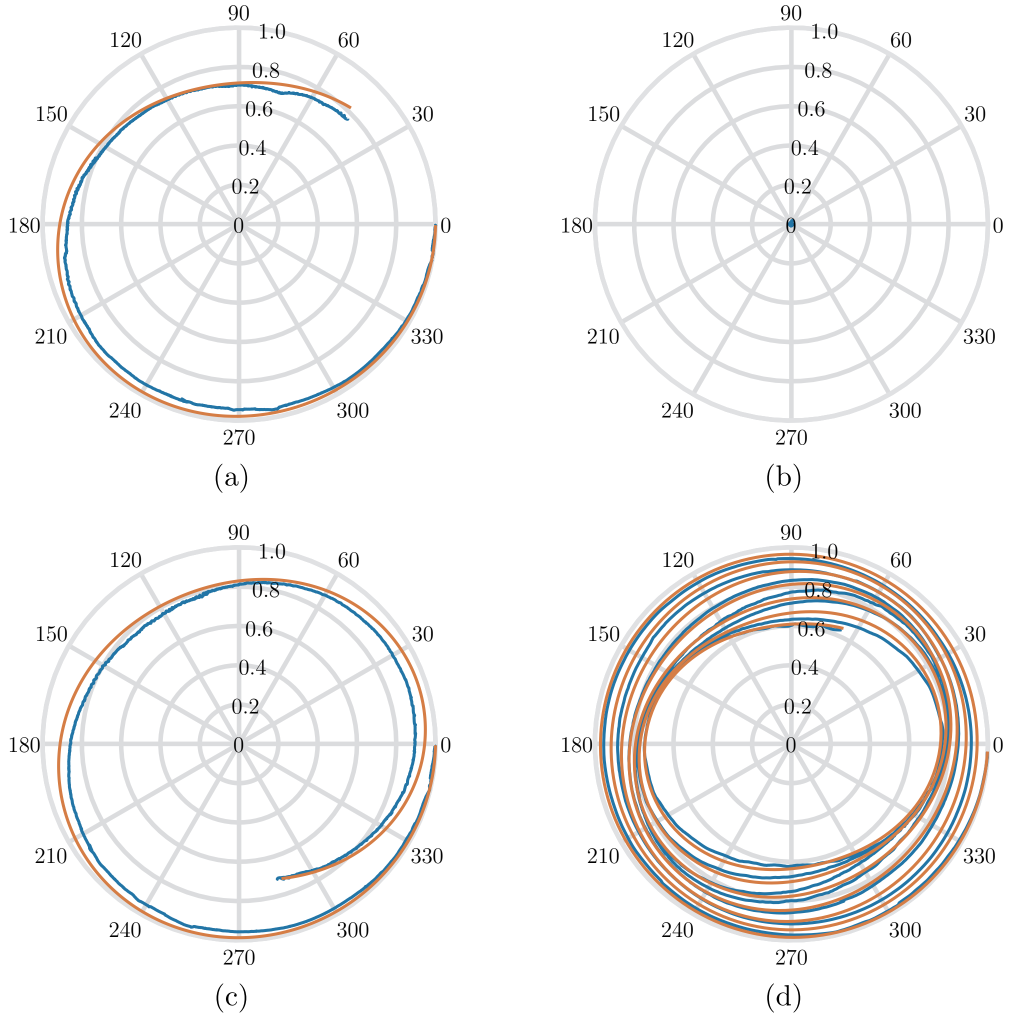


Figure 3.7: Comparing measured transmission loss (blue) with simulated one (orange) for Monte Carlo simulation: (a) thru (b) open (c) line 1 (d) line 2

## 3.5 Apparent dielectric constant to dispersionless effective dielectric constant

The positive and negative dispersion was already discussed in detail in Cha.2. The positive dispersions is compensated with (2.8) to (2.10). For the compensation of the negative dispersion a fully automated least-squares fit is computed (cmp. Fig. 2.8) according to (2.32) and is subsequently compensated.

## 3.6 Dispersionless effective dielectric constant to dielectric constant of substrate

For mapping the dispersionless $Dk_{\text{eff MS}}$ to the $Dk$ of the substrate two formulas taken from literature are utilized. The formula used for MS is taken from [18]. The formula uses the $Dk$ and all available dimensions (substrate height $h$, line width $w$, and copper thickness $t$). The expression looks as follows:

$$\begin{aligned} Dk_{\text{eff MS}} = & \frac{Dk+1}{2} + \frac{Dk-1}{2}\left(1+\frac{12h}{w}\right)^{-1/2} \\ & + F(Dk,h) - 0.217(Dk-1)\frac{t}{\sqrt{wh}} \end{aligned} \tag{3.2}$$

where $F(Dk,h) = 0.02(Dk-1)(1-w/h)^2$ for $w/h < 1$ and $F(Dk,h) = 0$ for $w/h > 1$. This formula has a stated accuracy of better than 1% compared with results obtained by solving an integral equation for $0.25 \leq w/h \leq 6$ and $1 \leq Dk \leq 16$ which contains the dimensions of the measured samples (i.e. $w/h < 3$ and $Dk < 4$). The basic formula expresses the dispersionless $Dk_{\text{eff MS}}$, however, this can easily be rewritten to solve for $Dk$ instead of $Dk_{\text{eff MS}}$.

For CBCPW, the elliptical integral of the first kind as proposed in [28] is computed (with the additional dimension of the gap $g$ between line and top ground):

$$Dk_{\text{eff CBCPW}} = \frac{1 + Dk\frac{K(k')}{K(k)}\frac{K(k_1)}{K(k_1')}}{1 + \frac{K(k')}{K(k)}\frac{K(k_1)}{K(k_1')}} \tag{3.3}$$

$$k = w/(w+2g) \quad k_1 = \frac{tanh(\frac{\pi w}{4h})}{tanh(\frac{\pi(w+2g)}{4h})}$$

$$k' = \sqrt{1-k^2} \quad k_1' = \sqrt{1-k_1^2}$$

Eqn. 3.3 needs also to be rearranged for readily computation of $Dk$ instead of $Dk_{\text{eff CBCPW}}$. Solving (3.3) with an elliptical integral presents no noticeable delay in the computations compared to MS.

## 3.7 Total uncertainty over frequency

This section presents the overall results of the Monte Carlo method. The Monte Carlo approach was taken because the uncertainties propagate in a non-trivial manner through the introduced stages. No closed-form results are presented in this section, however, it is still possible to evaluate the impact of each input uncertainty on the total uncertainties. For that reason four cases are taken into consideration to investigate the importance of some input uncertainties specifically.

The first case takes into account all manufacturing uncertainties as presented in Sec. 3.1 as well as the uncertainties of the VNA. The second case extends the first case by taking into account independent and unequal probing offsets for each calibration element of the TRL. In the third case the substrate thickness and the copper thickness are kept constant to evaluate any changes of uncertainties compared with the second case. The fourth case investigates the impact of the VNA uncertainties on the overall measurement uncertainty only, i.e. the dimensions of the samples are kept constant.

### 3.7.1 Case 1: Equal deviations of the probing offset

In this simulation run the uncertainties are exactly taken as described within the previous sections. Fig. 3.8a to Fig. 3.8d shows the deviation of $Dk$ for four different frequencies from their mean values. The selected frequencies are 2 GHz, 20 GHz, 70 GHz, and 110 GHz. The deviations show a very broad behavior for the lowest frequency 2 GHz and show close agreement to a normal distribution. Interesting to note is that at 20 GHz the distribution shows a much narrower behavior with significantly smaller standard deviation. At 20 GHz the distribution shows also a very slight negative skew, but for the other two frequencies 70 GHz and 110 GHz the skew is gone. For frequencies higher than 2 GHz, the distribution starts to widen up again to the maximum frequency.

Fig. 3.9 outlines the results for the overall Monte Carlo simulation for case 1 over frequency. In this representation it is not possible to evaluate the underlying distribution, however, it can be seen that the highest deviation occurs for the very lowest frequencies, for some runs even up to $\pm 1$. After this initial peak, the results narrow down quickly to the overall lowest deviations in between 20 GHz and 40 GHz. For frequencies above 40 GHz the deviations are continuously rising again up to $\pm 0.1$.

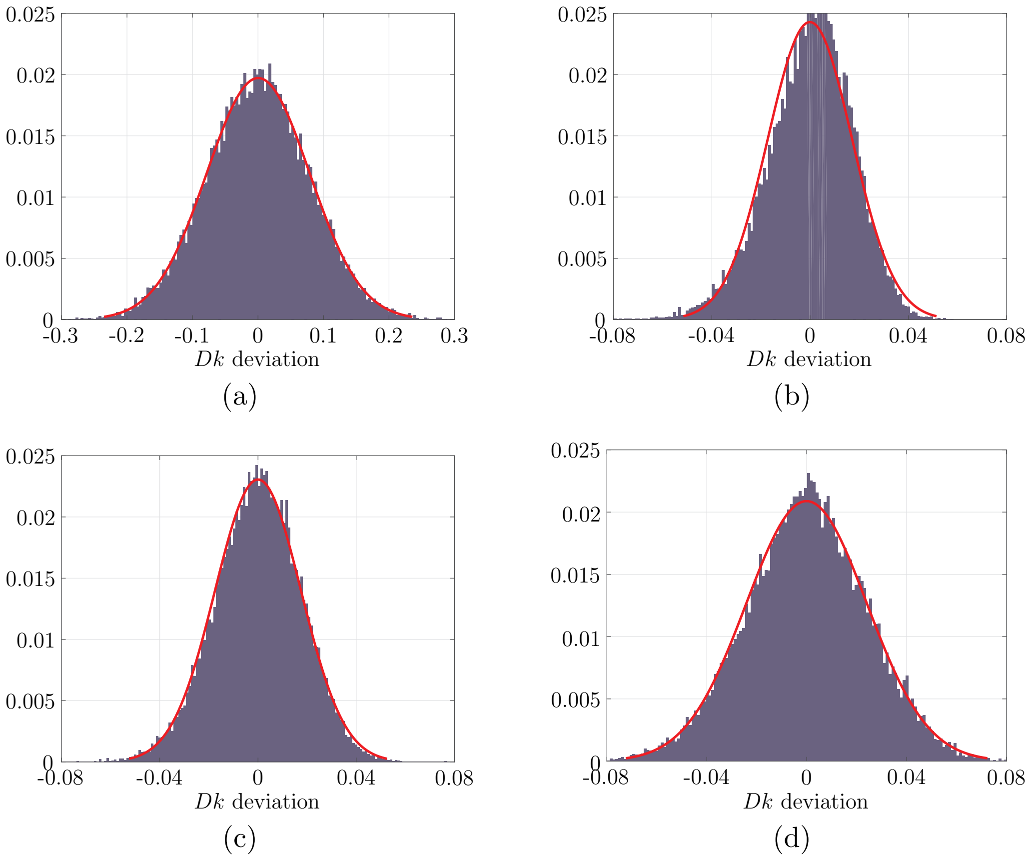


Figure 3.8: Evaluated uncertainties of $Dk$ for case 1: (a) 2 GHz (b) 20 GHz (c) 70 GHz (d) 110 GHz

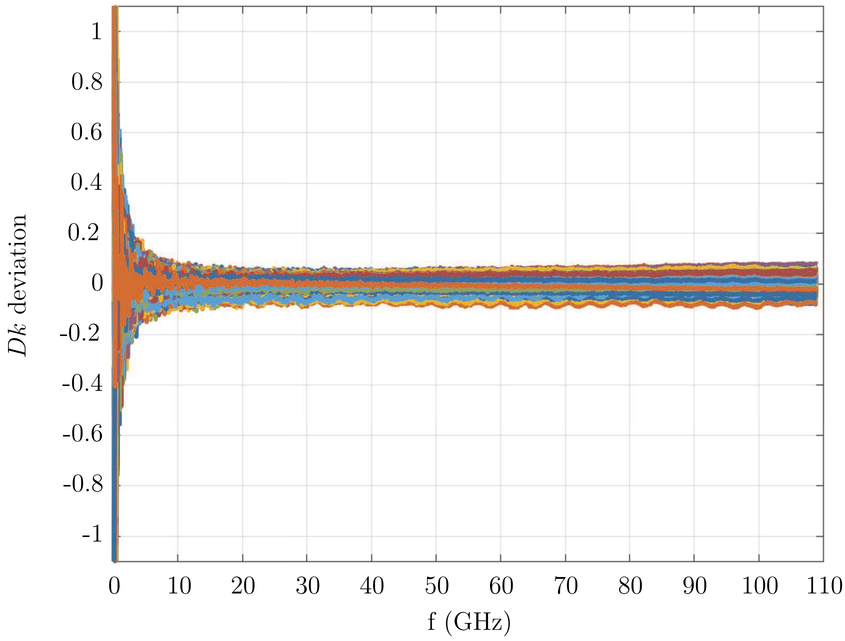


Figure 3.9: Evaluated uncertainty over frequency

### 3.7.2 Case 2: Unequal deviations of the probing offset

This case increases significantly the degrees of freedom. The probing offset is now modeled with four statistically independent random variables, all varying in the manner represented in Fig. 3.3b. The results of this simulation run are shown in Fig. 3.10a to Fig. 3.10d. It can be noticed that the distributions at 70 GHz and 110 GHz have slightly increased their width, and thus their standard deviation. This shows that the positioning of the probes is another contributor to the overall measurement deviations, especially for higher frequencies.

Fig. 3.11 shows the results over the whole frequency range. Compared with the results of case 1, here a slight resonance seem to occur close to 10 GHz which causes an increase of the deviations at this frequency.

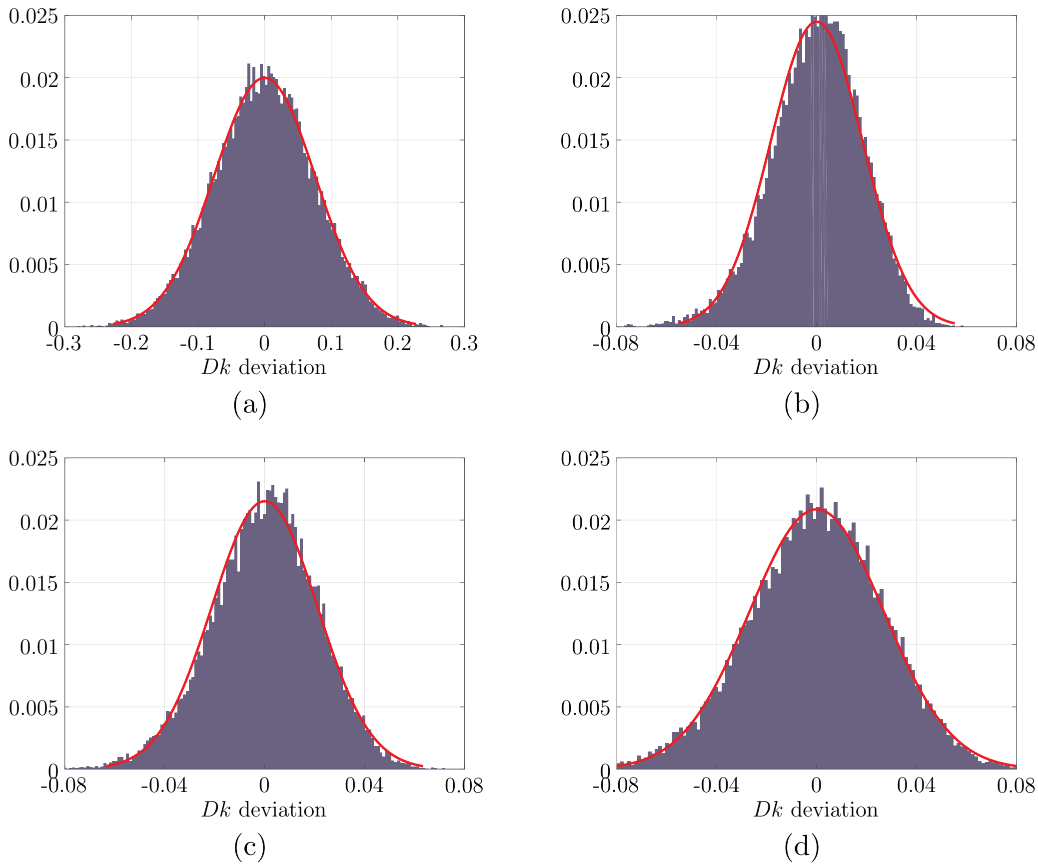


Figure 3.10: Evaluated uncertainties of $Dk$ for case 2: (a) 2 GHz (b) 20 GHz (c) 70 GHz (d) 110 GHz

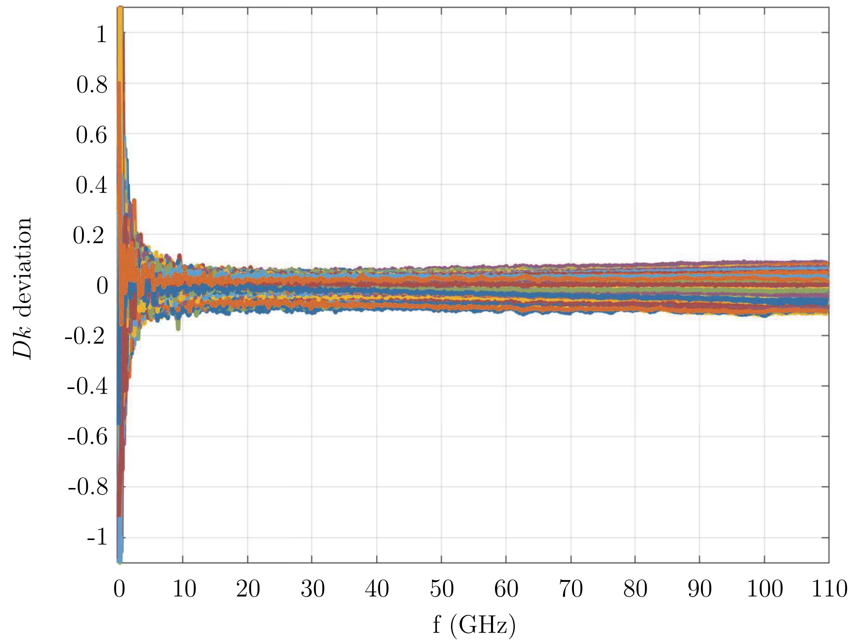


Figure 3.11: Evaluated uncertainty over frequency for independent probe offsets

### 3.7.3 Case 3: Unequal deviations of the probing offset and constant substrate height and copper thickness

The objective of the third case is to justify the assumption taken in Sec. 1.7. The assumption for the measured test structures was that all have an equal substrate thickness. Even when the substrate thickness may not be perfectly equal within a measurement series of test structures manufactured on the same batch, the impact on the measured values may be negligible. The results are presented in Fig. 3.12a to Fig. 3.12d.

Fig. 3.13a and Fig. 3.13b depict a direct comparison of the results of case 3 and case 2 for 2 GHz and 20 GHz. It can be noticed that there is barely no change within the results. The minute change of the standard deviation within the comparison, in relation to the overall standard deviation it is of negligible impact. For the measured test structures the aforementioned assumption is thus valid.

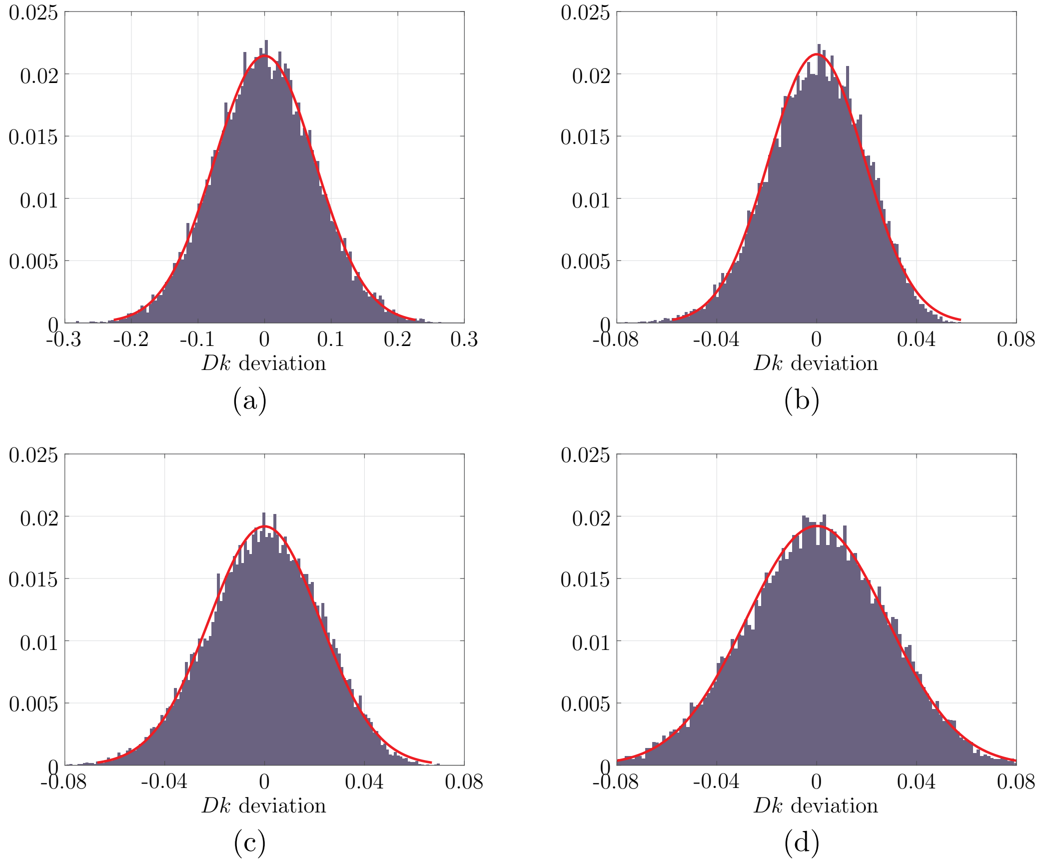


Figure 3.12: Evaluated uncertainties of $Dk$ for neglected substrate and copper thickness uncertainties (case 3): (a) 2 GHz (b) 20 GHz (c) 70 GHz (d) 110 GHz

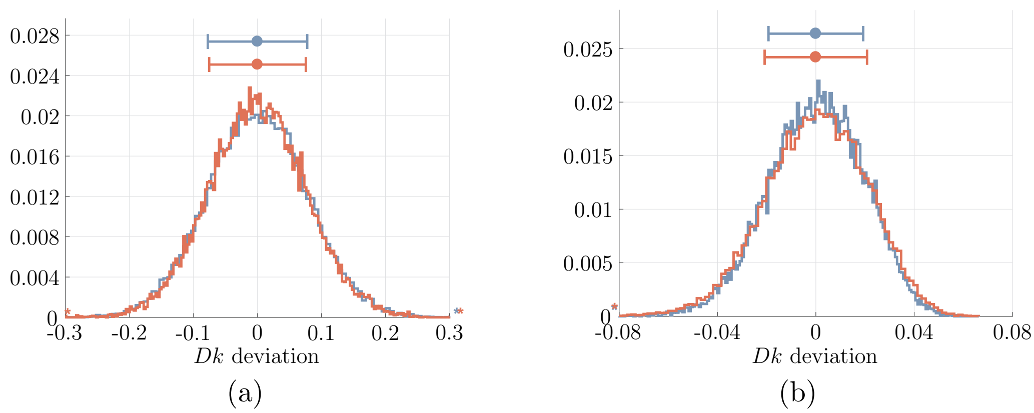


Figure 3.13: Distribution comparison of case 2 and case 3: (a) 2 GHz (b) 20 GHz

### 3.7.4 Case 4: Evaluation of the VNA uncertainties only

The case 4 is aimed to investigate the impact of the VNA uncertainties to the measurement results. All other uncertainties due to manufacturing and probing are set to zero in this case. In a first glimpse, the maximum line length of the measurement samples of only about 25 mm could be blamed to contribute significantly to the high uncertainty observed at the low frequency range. By taking an averaged dispersionless $Dk_{\text{eff}}$, it turns out that the phase condition needed by the TRL to operate unambiguously is fulfilled for frequencies down to 500 MHz. However, the Monte Carlo results shown in case 1 to 3 had at this frequency already an increased uncertainty.

Fig. 3.14a to Fig. 3.14d display the results when only the uncertainties of the VNA are included. The results show for low frequencies approximately the same results as in case 1 to case 3. However, for the frequencies 20 GHz, 70 GHz, and 110 GHz a significantly smaller standard deviation is observed. It should be kept in mind that the x-axis of the presented plots is kept in the same manner as all plots of case 1 to case 3 to allow an easy qualitatively comparison. The y-axis was extended to accommodate the steep distribution at 110 GHz.

Fig. 3.15 shows the results over the whole frequency range, which shows that the deviation has now a steadily decreasing behavior for increasing frequencies.

## 3.8 Conclusion

Within this chapter an extensive uncertainty analysis was carried out by means of Monte Carlo simulation for the proposed method of dielectric material characterization. Three sources of uncertainty were identified within the measurement procedure: manufacturing, probing, and the VNA measurement equipment. The etch rate of the manufacturing process is assumed to be normally distributed which leads to normally distributed manufacturing tolerances. For the probing, no prominent point could have been identified which is why the probing offset was assumed to be uniformly distributed. For the VNA uncertainties, the uncertainties in magnitude and phase can be found in the specifications of the VNA manufacturer.

The TRL calibration standards was modeled by closed-form transmission lines with the dimensions of the actual launching pads taken from microsections. By combining all uncertainty sources and processing the whole measurement method for 25000 times the uncertainties of the overall method were approximated. In total there were four important cases simulated separately. It turned out that especially the probing offset variations within one measurement run add a significant uncertainty to the overall procedure. Additionally it was shown that

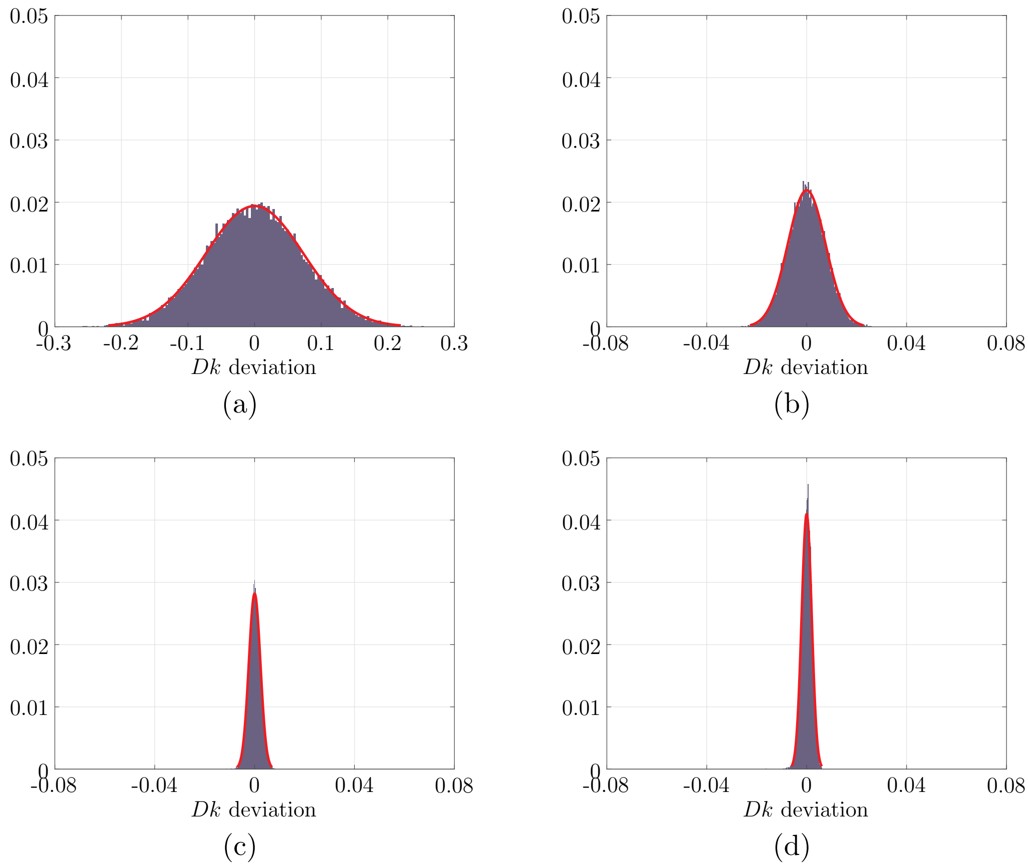


Figure 3.14: Evaluated uncertainties of $Dk$ for VNA uncertainties only (case 4): (a) 2 GHz (b) 20 GHz (c) 70 GHz (d) 110 GHz

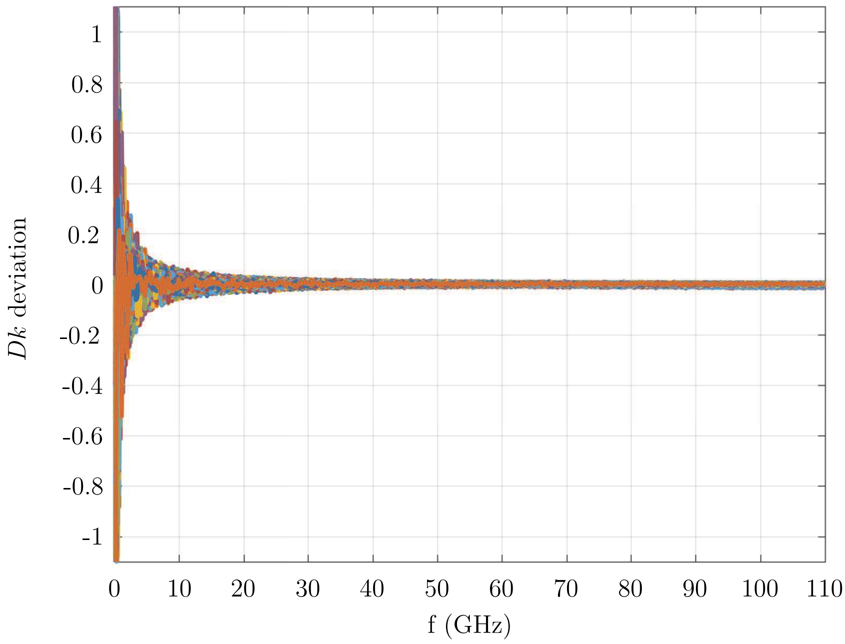


Figure 3.15: Evaluated uncertainty over frequency VNA uncertainty only

variations of the substrate thickness and the copper thickness have negligible impact on the overall uncertainty. The highest deviations occurred at the lowest frequencies. By a separate simulation of the VNA uncertainties alone, it was shown that these high deviations are inherent to the VNA.

# Chapter 4

# Dielectric characterization for two RF-substrate materials

Within this chapter the substrates of the manufactured test boards are characterized with two different approaches: a resonant method and three non-resonant methods (see Sec. 1.3). For both proposed materials all four characterization processes are applied and their results compared. This chapter characterizes first Panasonic Megtron 6 and then Pyralux Tk. The utilized structures are transmission lines of different lengths for the non-resonant methods and ring resonators for the resonant method. The investigated transmission line modes are MS, CBCPW, and SIW. Except for the SIW, all other methods (also the ring resonators) need a compensation of the described dispersion behaviors of Cha. 2. SIW has the advantage that the wave propagates in a homogeneous media, and thus the positive dispersion behavior does not occur (see Sec. 2.2). For cut-off frequencies higher than 20 GHz the negative dispersion is also negligible (see Sec. 2.3).

It should be noted that no evaluation of the loss tangent $LT$ is provided. As already pointed out, both investigated materials are low-loss materials, which means that the impact of dielectric loss (as contained within $LT$) shows only a minute impact on the overall losses. There are scientific publications available that state measurement results for low loss materials, however, these approaches rely usually on assumptions (for the skin-effect and surface roughness) that are not met by the measured structures within this chapter.

## 4.1 Megtron 6: non-resonant methods MS and CBCPW

The first investigation will focus on the non-resonant methods MS and CBCPW. The samples based on MS and CBCPW have all an inhomogeneous stack-up of a dielectric substrate and the surrounding air. The effects and their appropriate ways of understanding and tackling them was outlined in Cha. 2. The discussion will firstly show all steps of the method applied on the mean value of the measurements for all measured lines, and subsequently the confidence boundaries determined in Cha. 3 are applied.

### 4.1.1 Measurements

Fig. 4.1 depicts the measurement results of the measured $Dk$ for MS and CBCPW. These curves are regrouped from Fig. 1.15b and Fig. 1.16b. It should be noted that the measurements were previously normalized by its length to achieve comparable results for all different line lengths. From the length normalized lines the mean was computed and this serves as the basis for the computation of $Dk_{meas} = (\beta_{meas}/\beta_0)^2$. The CBCPW wave propagates approximately 2% more in air than the MS transmission line, as can be concluded by $Dk_{meas}$ for the designed lines for Megtron 6.

### 4.1.2 Dispersion compensation

In the first step the positive dispersion is compensated by all introduced manners of Sec. 2.2. For MS, the different approaches for compensation contain a cross-sectional simulation and two analytical expressions of [21] and [22]. Due to the lack of analytical expressions, for CBCPW it is only possible to achieve a compensation with a simulation. Fig. 4.2 shows the results. It can be seen that for MS the positive dispersion is compensated differently to a different extent for each approach. Most prominently it can be observed that by simulation the positive dispersion is inflected to a slightly falling behavior, whereby for the analytical computation some residual positive dispersion is preserved. For further investigation the analytical compensation according to (2.8) will be taken for MS. The results for the CBCPW show similarity with the simulated MS compensation except for the offset.

### 4.1.3 Measured dielectric constant over frequency

The steps after the positive dispersion compensation until the $Dk$ values of the substrate are processed in a similar manner as shown in Cha. 3. The final results

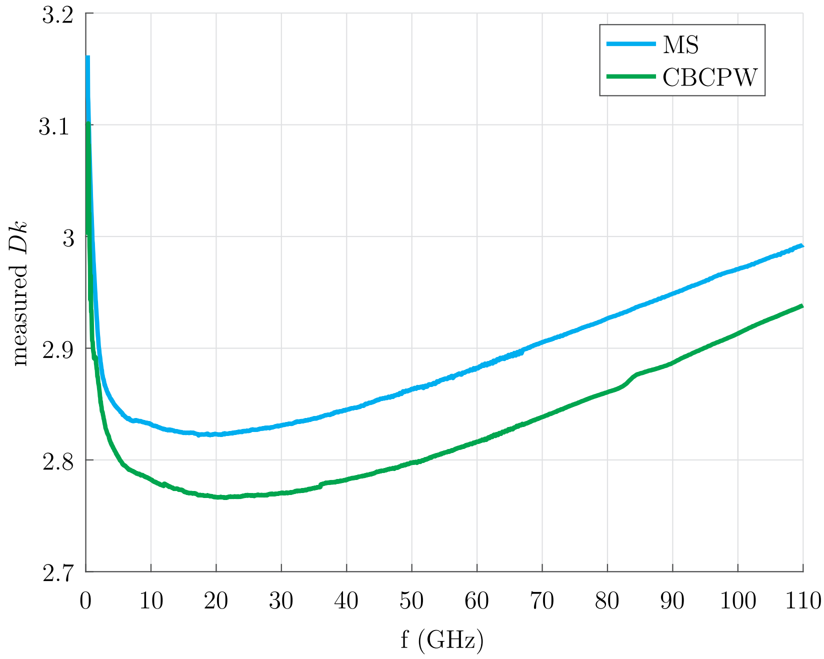


Figure 4.1: Measurements of $Dk$ for Panasonic Megtron 6

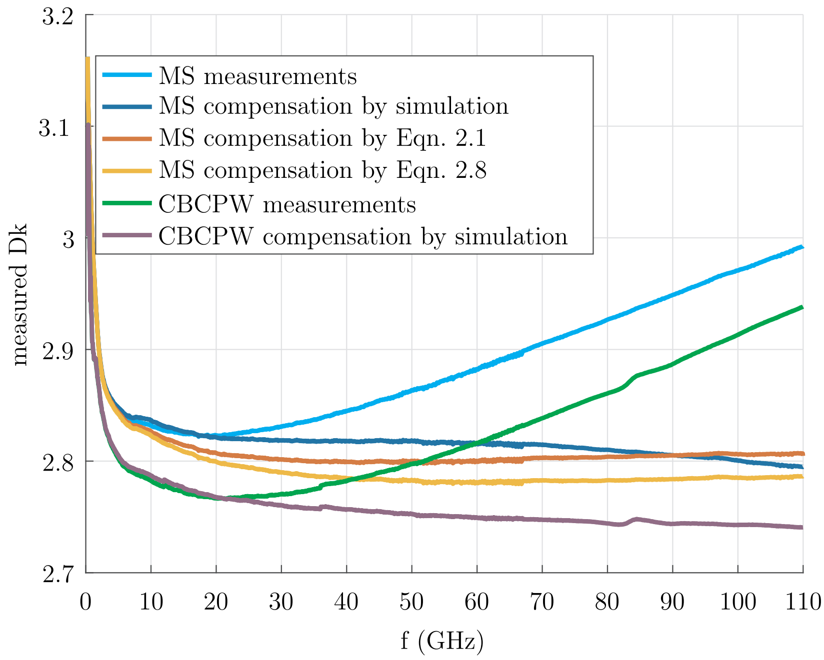


Figure 4.2: Measurements of $Dk$ for Panasonic Megtron 6

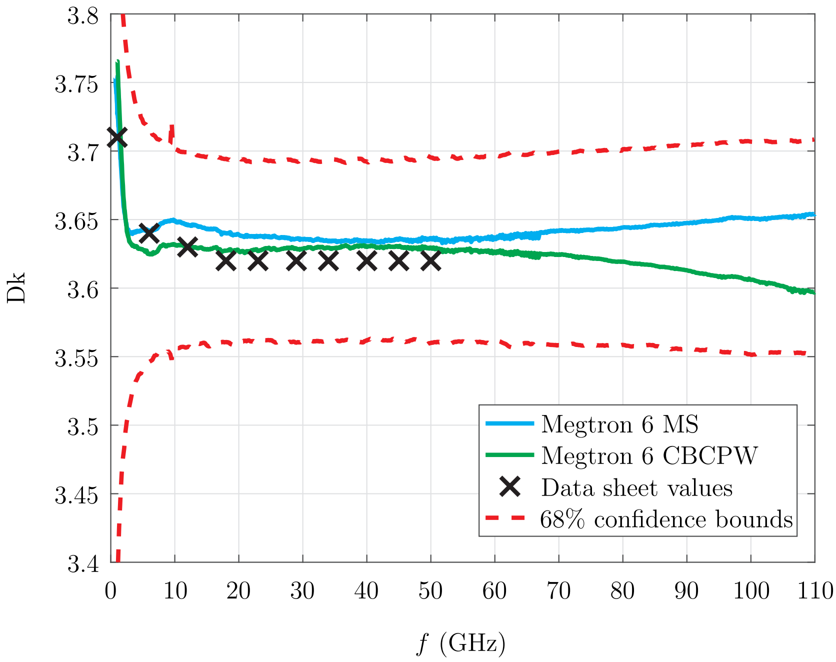


Figure 4.3: Measurement results for Megtron 6 for MS and CBCPW

are shown in Fig. 4.3. It does not only display the obtained values from the measurements but also the data sheet values stated by the manufacturer for the Panasonic Megtron 6 material. It can be noticed that the slightly falling behavior for the CBCPW and the slightly increasing behavior for the MS is preserved even after the compensation of the negative dispersion and the mapping to the substrate. However, the impact is very subtle and lies well within the boundaries presented in Sec. 3.7.2.

## 4.2 Pyralux Tk: non-resonant methods MS and CBCPW

In a similar manner as in Sec. 4.1 the same steps will be taken for the characterization of Pyralux Tk. The samples based on MS and CBCPW all have an inhomogeneous stack-up of an dielectric substrate and the surrounding air. The effects and their appropriate ways of understanding and tackling them was outlined in Cha. 2. The discussion will firstly show all steps of the method applied on the mean of the measurements for all measured lines, and subsequently the confidence bounds determined in Cha. 3 are added.

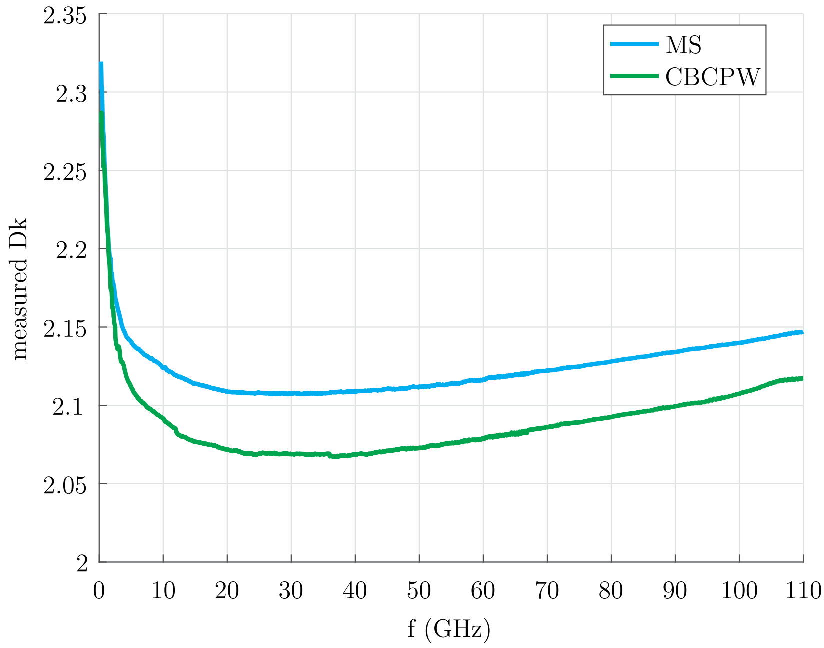


Figure 4.4: Measurements of $Dk$ for Pyralux Tk

### 4.2.1 Measurements

Fig. 4.1 depicts the measurement results for MS and CBCPW. These curves are regrouped from Fig. 1.15b and Fig. 1.16b. It should be noted that the each line measurements was previously normalized by its line length to achieve comparable results. From the length normalized lines the mean was computed and this serves as the basis for the computation of $Dk_{meas} = (\beta_{meas}/\beta_0)^2$. The CBCPW wave propagates approximately 2% more in air than the MS transmission line (same as for Megtron 6), as can be concluded by $Dk_{meas}$ for the designed lines.

### 4.2.2 Dispersion compensation

In the first step the positive dispersion is compensated by all introduced manners of Sec. 2.2. For MS, the different approaches for compensation contain a cross-sectional simulation and two analytical expressions of [21] and [22]. Due to the lack of analytical expressions, for CBCPW it is only possible to achieve a compensation with a simulation. Fig. 4.5 shows the results. It can be seen that for MS the positive dispersion is compensated differently to a different extent for each approach. For Pyralux it is interesting to note that the positive dispersion is turned into a negative dispersive behavior for MS and CBCPW and also for the analytical compensation and the compensation by simulation. The results for

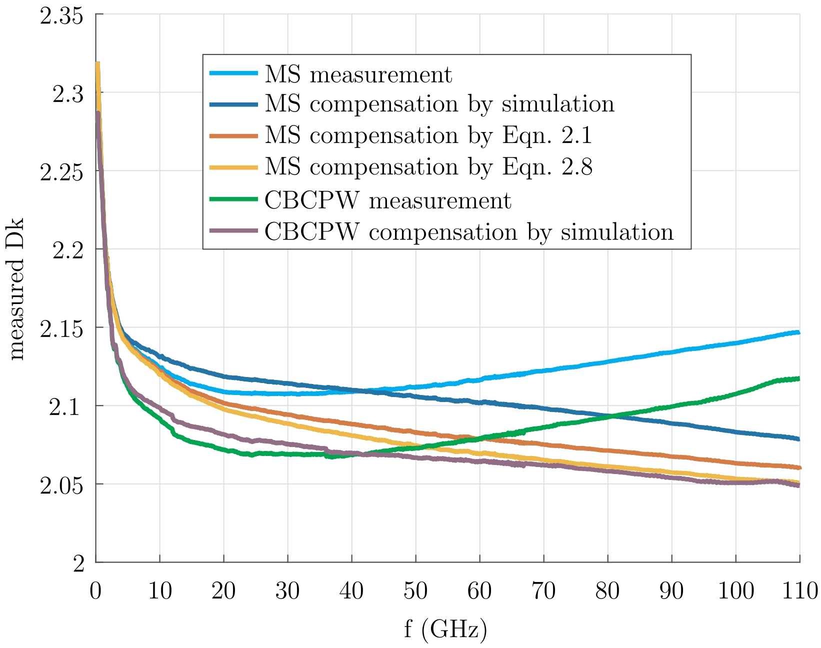


Figure 4.5: Measurements of $Dk$ for Pyralux Tk

the CBCPW show again very similar results to the MS except for the preserved offset.

### 4.2.3 Measured dielectric constant over frequency

The steps after the positive dispersion compensation until the $Dk$ values of the substrate are processed in a similar manner as shown in Cha. 3. The final results are shown in Fig. 4.3. It does not only display the obtained values from the measurements but also the data sheet values stated by the manufacturer for the Pyralux material. It can be noted as well that the decreasing behavior after compensation of the positive dispersion is still present in the final plot of the $Dk$. However, with only a small deviation of a maximum of 2% and well in the stated uncertainty bounds of Cha. 3.

## 4.3 Microstrip resonators

For both of the materials four resonators were manufactured (see also Sec. 1.3.2). The resonators were designed to show multiples of 10 GHz in their resonance frequencies for Megtron 6. The fundamental resonance of the four resonators was chosen as 10 GHz, 20 GHz, 30 GHz, and 40 GHz. When the resonance peaks are

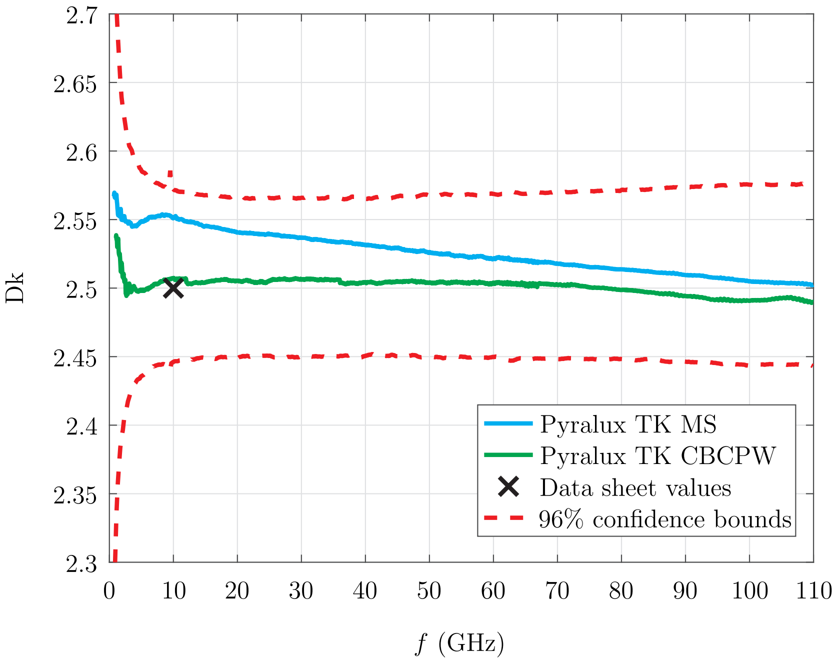


Figure 4.6: Measurement results for Pyralux TK for MS and CBCPW

in close proximity they tend to overlap more in the valley regions as the next resonance frequency is about to start. For that reason resonators with higher spacings in between the resonances were manufactured and simulated as well. The nominal dimensions were kept constant for both materials for being able to use the same micro section analysis.

For the characterization of $Dk$ with resonators, the determination of precise resonance frequencies is of utmost importance. During the measurements this was taken into consideration for a frequency spacing of 40 MHz in between measured frequency points over the whole frequency range. This spacing was taken as a trade off between high precision and time efficient measurements. In the next section the measurements as well as the peak search algorithm is explained, to show which values for the resonances were taken for the characterization.

### 4.3.1 Measurements and peak search

For the peak search several steps were implemented to achieve an automated and reliable determination of the resonance peaks. Because some resonance peaks were distorted in measurements, a more complex approach was necessary. This distortion can be noticed in measurements as one prominent resonance frequency shows small peaks next to each other instead of one unambiguous one. The cause of these resonances was investigated in detail in two ways, a time domain transmission analysis and a field simulation of the asymmetric feeding of the ring resonator structures. The time domain transmission analysis was carried out to check if a minute mismatch by the cables used to connect the wafer prober and the VNA is the cause. However, in the time domain it was not possible to distinguish any superimposed resonance, and therefore no filtering could be done to alleviate this effect. In a second attempt the coupling of the resonator was simulated, but the simulation results have also not shown promising results for explaining this effect.

One example for a resonance with multiple peaks is shown in Fig. 4.7. Fig. 4.8a and Fig. 4.8b show the results of the implemented algorithm for Megtron and in Fig. 4.9a and Fig. 4.9b for Pyralux. These plots show the results of the peak search algorithm over the whole frequency range. The first step of the algorithm is a peak search for peaks of a prominence of 0.1 dB (shown with blue triangle markers). It can be seen that at some resonances multiple peaks are found, however, also many peaks caused by a superimposed distortion at very low levels of insertion loss. It would not be possible to cut values of the insertion loss simply below a constant level over frequency, because for increasing frequencies the quality factors of the resonances are decreasing which leads to less prominent valleys. To overcome this shortcoming the first peak is filtered individually. The initial resonance shows in all measurements a high prominence. With this steep prominence the first resonance can be found easily. In the next step the overall maximum of the measurement data is searched. With the peak value of the first resonance and the overall maximum a decision boundary is calculated and a margin of -3 dB is added. The decision boundary is shown as a dashed black line. All peaks above that decision boundary are considered to be valid resonance peaks. However, there may still be manifold peaks at one main resonance. For that, the peaks are investigated by their width. Peaks with a very low width are considered to be in close proximity to another peak on the same resonance. For two adjacent peaks on one resonance the mean value is calculated in frequency and insertion loss. The peaks determined by the entire algorithm are shown with red circular markers. These peaks are used for subsequent characterization of the substrate.

By closer investigation of Megtron 6 in Fig. 4.8a the behavior of the algorithm can be comprehended. After the initial peak search many candidates are found. In the second step the first resonance peak is filtered by its significant prominence and high q-factor. A line is drawn in between the first peak and the overall maximum (that is also put to the maximum frequency). After adding the 3 dB margin the boundary is set. All peaks above the decision boundary are investigated for manifold solutions of each peak. In Fig. 4.8a, this last step for determining the overall peak out of several small peaks of the resonance can be noticed on above 60 GHz (see also in Fig. 4.8b the resonance at about 85 GHz).

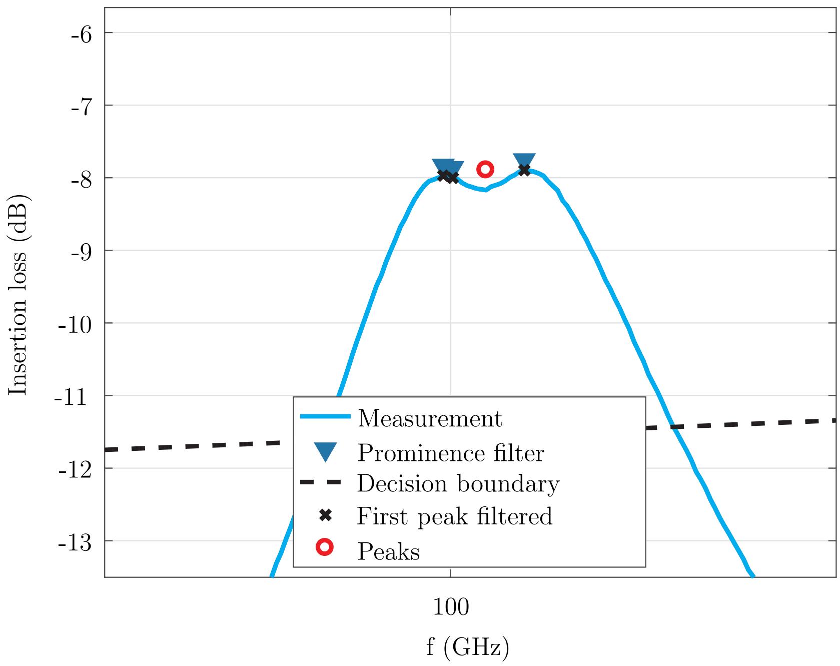


Figure 4.7: Zoomed peak

The results of two resonators for Pyralux are shown in Fig. 4.9a and Fig. 4.9b. Compared with the measurements of Megtron 6, for Pyralux there was no ambiguous resonance for the 10 GHz-resonator, only for the 30 GHz-resonator at the last resonance.

This algorithm was run for both sets of scattering parameters, i.e. $S_{12}$ and $S_{21}$, where both results are used for further analysis of the dielectric constant $Dk$.

Utilizing the dimensions taken from micro sections, the measured S-parameters are mapped to $Dk$. Within this conversion the curvature effect of the ring resonators was taken into account according to [29]. The results are shown in Fig. 4.10a for Megtron 6 and in Fig. 4.10b for Pyralux TK. For all of the determined values of the $Dk$, boxplots were calculated, as well as the mean value, all shown in the plots. It can be noticed that in the whole measurement series there are some peaks that show significantly more spread than others. It should be kept in mind that for some peaks there is a sample size of only four values which is a pair of two values which are not statistically independent ($S_{12}$ and $S_{21}$).

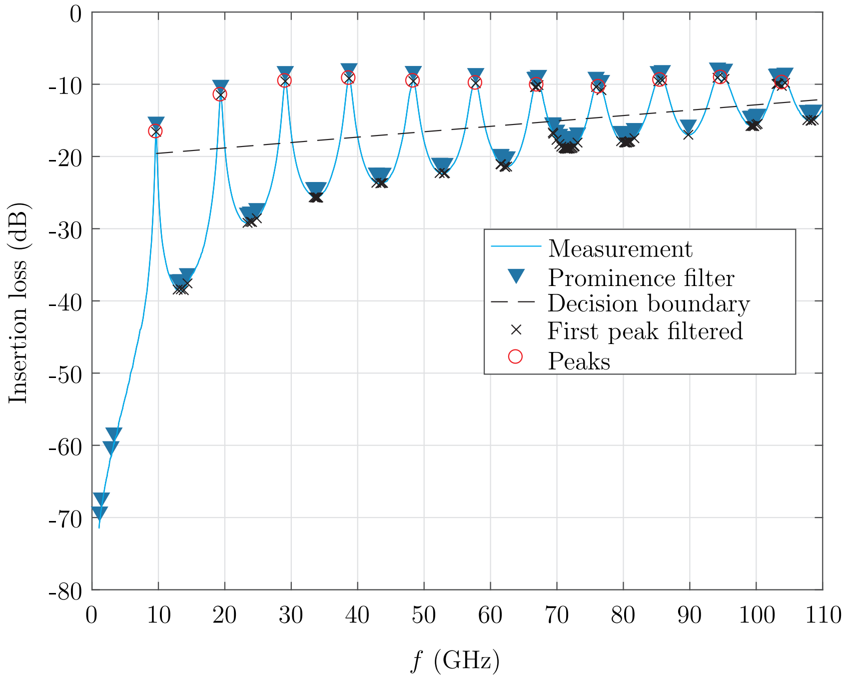


(a)

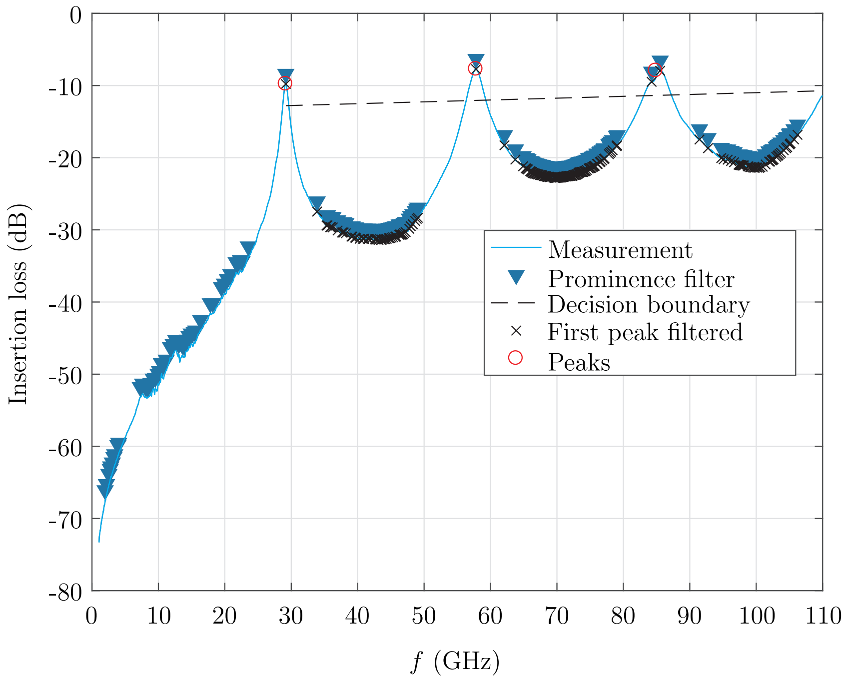


(b)

Figure 4.8: Megtron 6 MS resonator measurements and resonance filtering for resonators of different fundamental resonance: (a) 10 GHz (b) 30 GHz

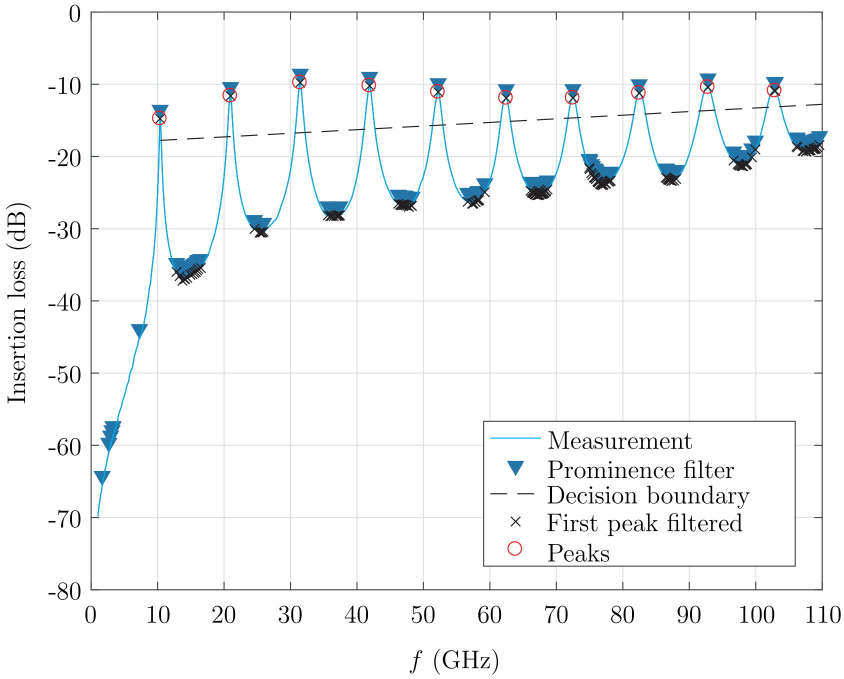


(a)

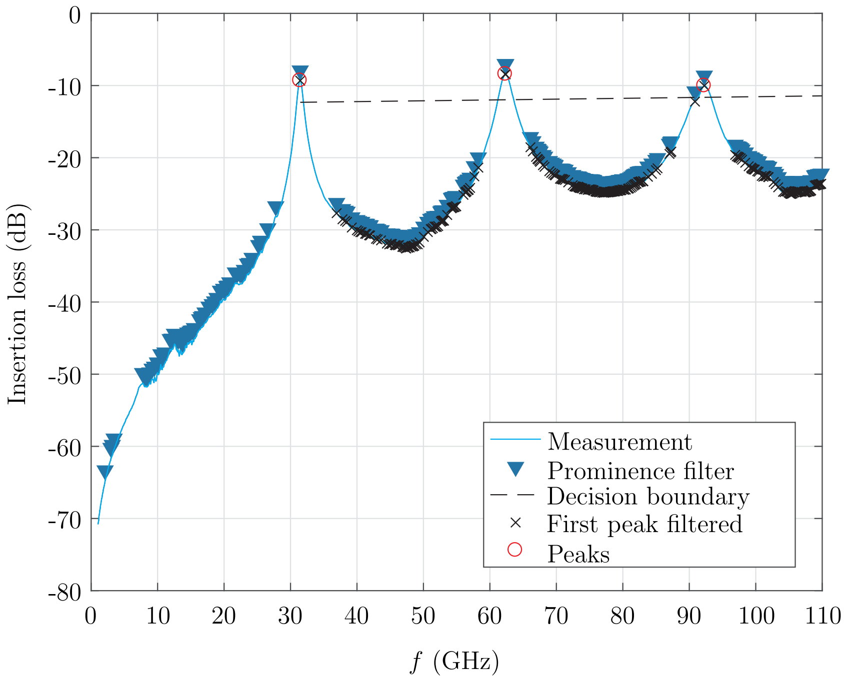


(b)

Figure 4.9: Pyralux 6 MS resonator measurements and resonance filtering for resonators of different fundamental resonance: (a) 10 GHz (b) 30 GHz

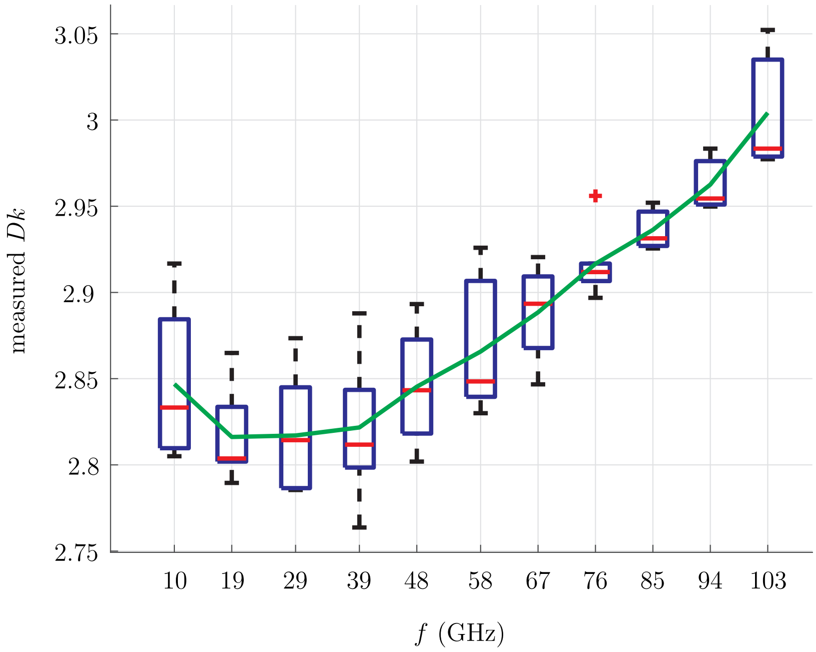


(a)

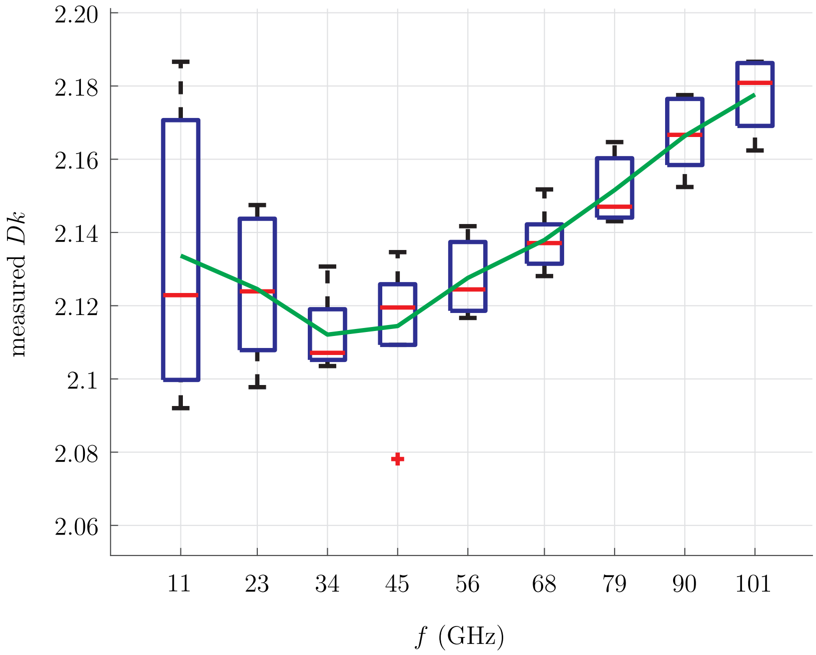


(b)

Figure 4.10: Measured $Dk$ by resonators: (a) Megtron 6, (b) Pyralux

### 4.3.2 Dispersion compensation

The dispersion compensation is carried out in the same manner as introduced in Sec. 2.2. For the positive dispersion compensation, simulations are used to take into account the coupling effects of the resonator that may bias the results. For the negative dispersion the formula presented in (2.32) shows less coefficient of determination for the least square fit (cmp. Fig. 2.8) because only a couple of points for decreasing dispersion can be used compared with the MS or CBCPW data.

### 4.3.3 Dielectric constant over frequency

Fig. 4.10b displays the results that are fully compensated of dispersions and remapped to the substrate. The data sheet values are shown in this plot as well. Compared to the data sheet values, the determined $Dk$ lies within $\pm 0.8\%$ for Megtron 6, and within $+1.6\%$ for Pyralux TK.

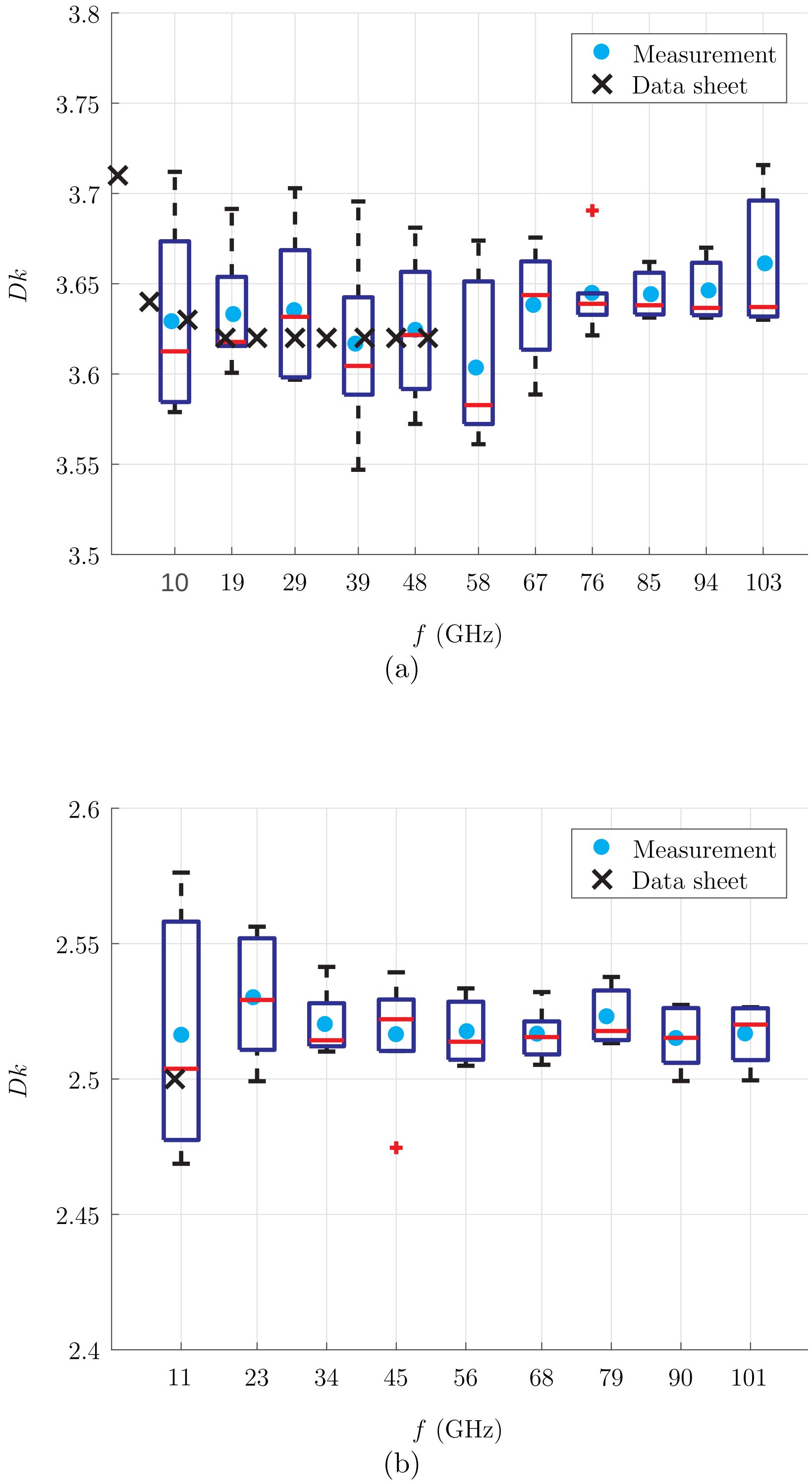


Figure 4.11: Measured *Dk* by resonators: (a) Megtron 6 (b) Pyralux TK

## 4.4 SIW

The characterization with substrate integrated waveguides (SIW) shows significant differences with the former methods by resonators, MS-, and CBCPW lines. The SIW, like a conventional waveguide (e.g. WR-28), has the significant benefit of offering a homogeneous wave propagation i.e. the entirety of the wave propagates exclusively in the MUT. This makes the whole characterization process very straightforward for the $Dk$, as no dispersion effects need to be taken into account (cmp. Cha. 2). Compared with a conventional waveguide, the manufacturing tolerances of an SIW have a more intricate impact. The sidewalls of the SIW are made of microvias i.e. each via is made by a laser beam melting and vaporization (or ablation) of the PCB material. Although the aspect ratio of these drills and the minute diameters that can be achieved are unprecedented, there is also a down side. By looking at microvias with a micro section, it can be seen that they show a conical instead of a cylindrical cross section. The micro vias are placed next to each other so there are unavoidable gaps in the sidewalls. The microvias have a circular footprint, that means also that it is not straightforward which dimensions are used to determine the effective width of the SIW.

Some constraints for dimensioning a SIW is to neglect radiation losses through the sidewalls, as can be found in literature [30] (with the guided wavelength $\lambda_g$, $d$ the via diameter, and $p$ the via pitch or via distance):

$$d = \lambda_g/5 \tag{4.1}$$

$$p \leq 2d \tag{4.2}$$

Megtron 6 is the material with the higher $Dk$ for both investigated materials, and thus the constraints are slightly more challenging for it. As stated by the manufacturer, Megtron 6 has a $Dk$ of 3.62 at 10 GHz. With this $Dk$ the minimum $d$ computes with (4.1) to 1.4 mm and $p$ should be smaller than 2.8 mm according to (4.2). The actual dimensions of the manufacturing were as follows: $p$ of 400 $\mu$m and $d$ of 150 $\mu$m. This shows that the constraints of [30] are more than met for the test structures and the modeling of these SIWs can be carried out like for normal waveguides (as the radiation loss through the sidewalls is negligible).

Another important aspect of the SIW is to decide which width is taken to determine the cut-off frequency of the SIW. In [31] a formula can be found to take into account the width (i.e. center-to-center measurement of the vias that represent the sidewalls), $d$ the via diameter, and $p$ the via pitch of the adjacent vias representing the sidewalls:

$$w_{eff} = w - \frac{d^2}{0.95p} \tag{4.3}$$

The width of the waveguide is nominally $w = 1700\,\mu$m which leads to $w_{eff}$ of 1641 $\mu$m by (4.3). It should be noted that for both materials the same dimensions of the waveguide were taken so $w_{eff}$ stays the same (and not the cut-off frequency). This was done to avoid an excess of micro sections needed to evaluate the manufacturing process.

### 4.4.1 Measurements

Fig. 4.12 shows the insertion loss of the investigated SIWs for both materials. In this plot the difference of the cut-off frequency can be noted due to the constant manufacturing dimensions. It can be seen that the SIW using the Megtron 6 does not only have higher insertion loss but also a slightly falling behavior over frequency, whereas the Pyralux SIW shows constant insertion loss over frequency. This effect can be contributed that the additional losses occurring in the substrate are matched to the reduced conductor losses over frequency. This situation looks different for the Megtron 6 as it shows significantly more dielectric loss than Pyralux. This means that the increase of dielectric losses is not compensated by the decrease of conductor losses over frequency.

A simple computation of $Dk$ can be carried out already with the insertion loss for one single frequency point. By determining the cut-off frequency with an inflection point search, the $Dk$ for Megtron 6 at the cut-off frequency is 3.62 and for Pyralux TK it is 2.43. However, this is not a good approach as it cannot be said that the cut-off frequency is exactly at the inflection point of the insertion loss. Additionally, this provides only information at one frequency.

### 4.4.2 Dielectric constant over frequency

For determining the dielectric constant by means of SIW, phase measurements of SIWs with different lengths were taken. There was also a TRL calibration carried out for taking care of the discontinuities of the launching pads and the MS-tapers to match the wave impedance of the launch to the wave impedance of the SIW. During the evaluation of the measurements it showed that the reference plane taken during the TRL calibration was located too close to the MS-to-SIW discontinuity. When the reference plane is taken at a plane where the $TE_{10}$ mode is not fully established, the subsequent measurements show unphysical behavior. Within this study eight different lengths for each SIW were manufactured, which could be used to overcome the aforementioned problem. As the four longest SIWs had a fully established $TE_{10}$ mode, the phase differences of these lines were taken. All of the six possible variations were used to compute $Dk$.

For waveguides it is important to take into account the contribution of the wave normal to the direction of propagation as well for finding the $\beta$ of the guided

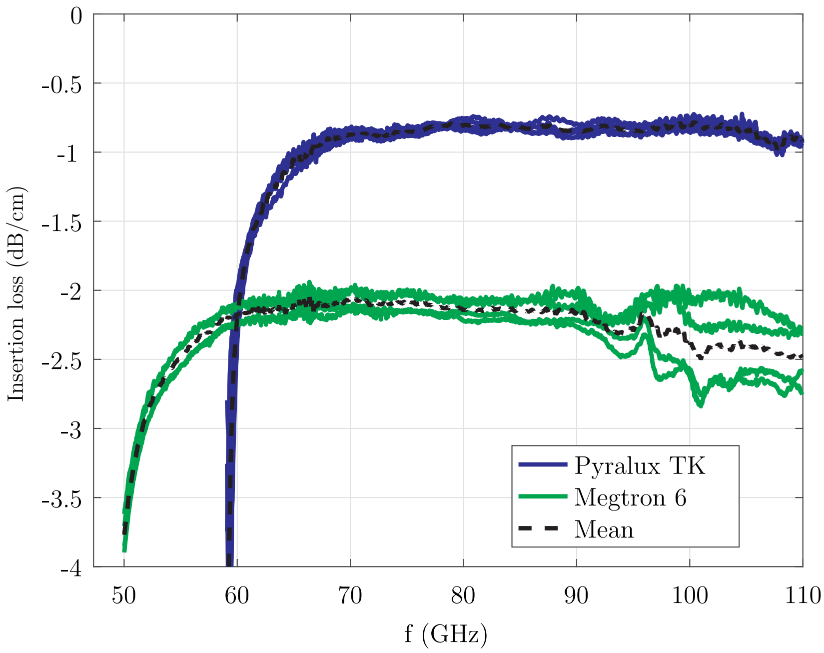


Figure 4.12: Insertion loss SIW

wave only (e.g. [32] for conventional waveguides). The $Dk$ can then be readily computed (with $mu_0$ the permeability of vacuum and $Dk_0$ the permittivity of vacuum):

$$Dk = \frac{\beta^2_{SIW,meas} + \left(\frac{\pi}{w_{eff}}\right)^2}{\omega^2 \mu_0 Dk_0} \tag{4.4}$$

The width of a conventional waveguide was substituted for the SIW by $w_{eff}$. It should be noted that up to the maximum measured frequency the waveguide can be assumed single mode, and thus the shown representation suffices.

Fig.4.13a and Fig.4.13b depict the results. Generally a very flat behavior over frequency can be observed. Close to the cut-off frequency the determined $Dk$ shows high variation, but as soon as the waveguide acts as a transmission line a close to constant behavior can be seen. It should be noted that the data sheet values were not plotted for these results as they are only available for frequencies much below the cut-off frequencies of the SIWs. Within the figures there is also the mean value plotted of all six measured $Dks$. This mean value will be compared to the results of all other characterization methods in the next section.

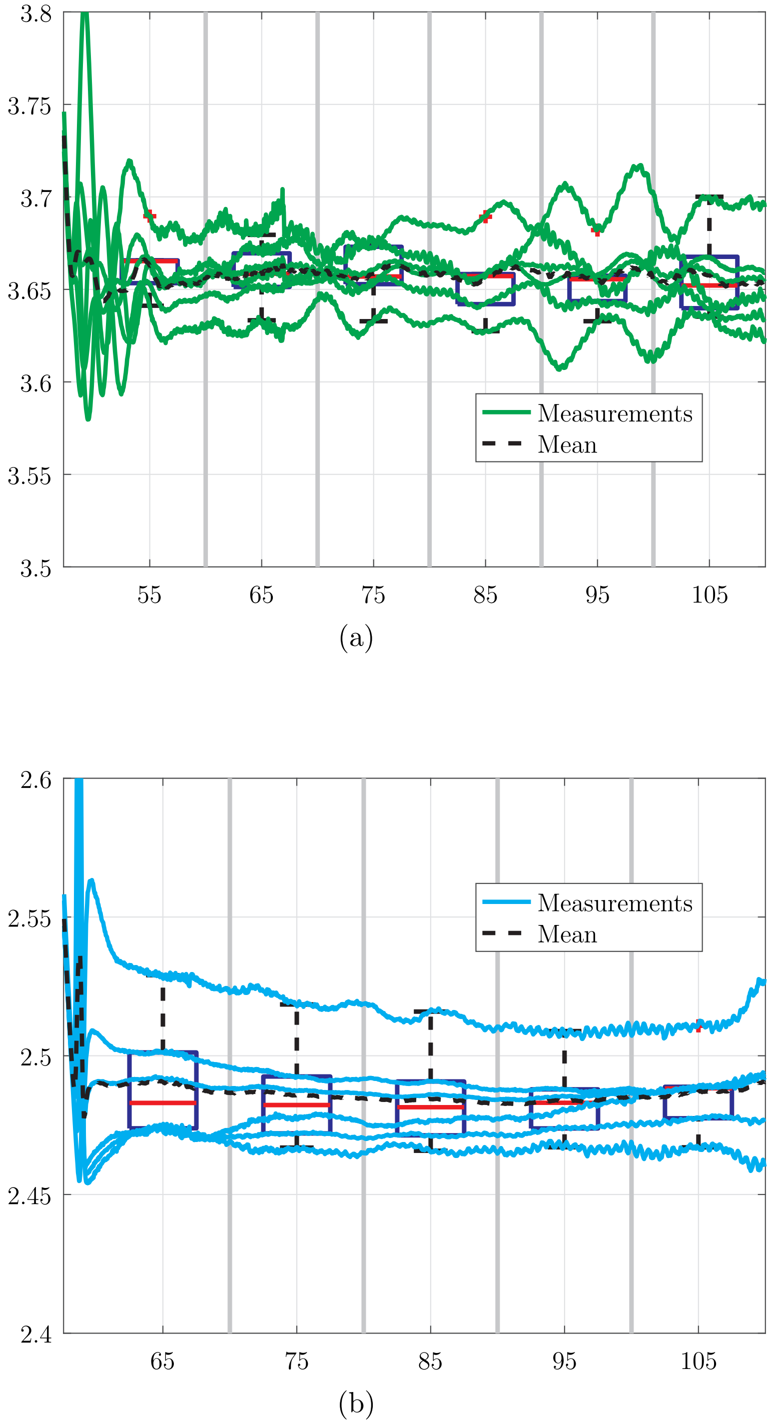


Figure 4.13: Measured *Dk* by SIW: (a) Megtron 6 (b) Pyralux TK

## 4.5 Measured $Dk$ comparison and conclusion

In Fig. 4.14a and Fig. 4.14b the results of all introduced characterization methods for the $Dk$ are plotted together for easier comparison. It can be concluded that all four investigated measurement procedures for determining the $Dk$ of a PCB substrate material have similar results. All computed results lie within a range of 0.07 of $Dk$ for Megtron 6 and Pyralux. This range maps to an overall variation of approximately $\pm 1\%$ for Megtron 6 and $\pm 1.4\%$ for Pyralux. This shows that the overall variation was within very close range for all investigated characterization methods. For example, a targeted $50\,\Omega$ MS transmission line with Megtron 6 would change within $\pm 0.2\,\Omega$ for the stated variation. This emphasizes that in terms of accuracy all methods show good results for even very stringent requirements on wave impedance. However, the effects that have to be taken into account to end up with the $Dk$ can vary significantly. With the straight forward method introduced within this thesis, it now makes the characterization of inhomogeneous transmission lines straight forward and easy to apply, so that no additional method needs to be applied for circuits that are already designed with MS or CBCPW lines.

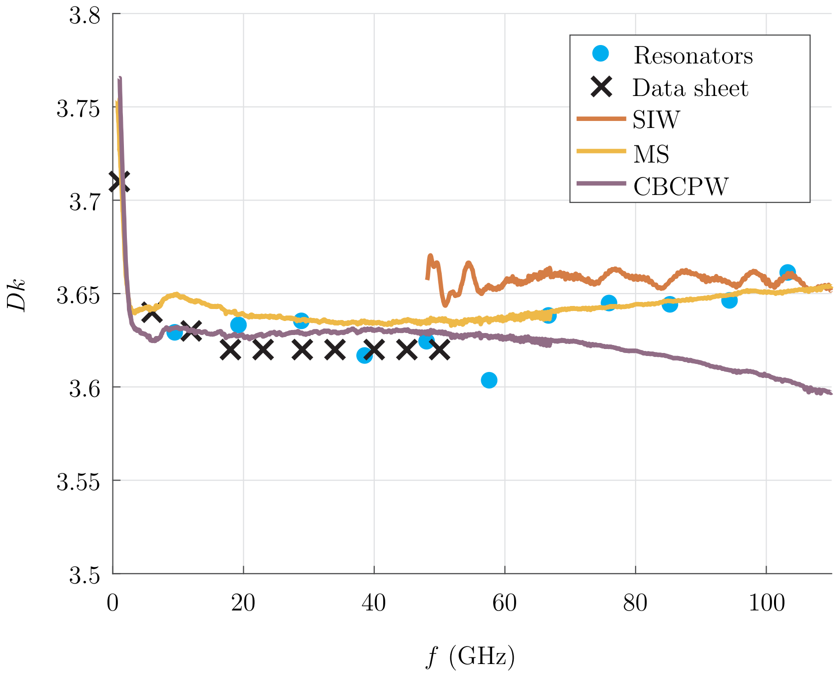

(a)

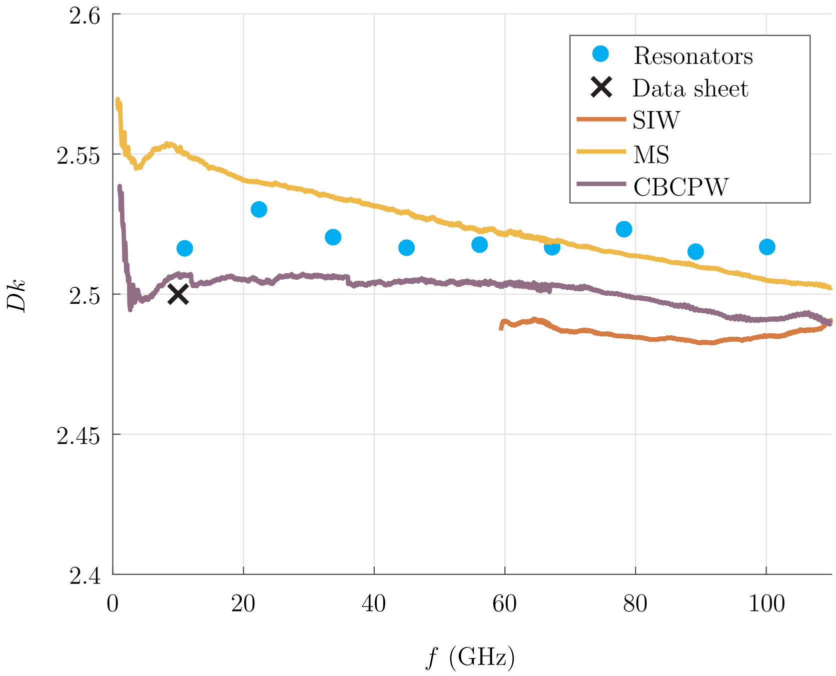

(b)

Figure 4.14: Measured *Dk* comparison: (a) Megtron 6 (b) Pyralux TK

# Chapter 5

# Conclusion

Within this thesis a straight forward method was introduced for transmission lines with inhomogeneous stack-ups to be used for dielectric characterization for a continuous frequency range up to 110 GHz. Although there are many effects to be taken into account within a reliable characterization, the whole compensation process is based on analytic formulas which can readily be computed. The crucial benefit of this characterization method is that microstrip (MS) and conductor-backed coplanar waveguides (CBCPW) are widely used transmission lines and can now serve simultaneously for reliable characterization of the material up to 110 GHz.

The increasing frequency demands of state-of-the-art applications, at this point they have already reached the upper two-digit gigahertz range, needs thinner printed circuit boards (PCBs) for avoiding multimode propagation. Thinner PCBs still have the same copper thickness as thicker PCBs as the manufacturing processes does not need to be adjusted depending on different substrate thicknesses. This constant copper thickness means that the internal inductance (inside of the conductor) of the transmission lines stays constant for different thicknesses of PCBs. However, for thinner PCBs the external inductance (in the dielectrics) is evidently smaller as for a thicker one. This relative increase of internal inductance over external inductance impacts the measured dielectric constant for frequencies up to several gigahertz (for the investigated samples it was approximately 20 GHz). However, as shown in this thesis there is a straightforward manner to take care of this effect for low loss substrate materials by least square fitting the apparent $Dk$ to $\hat{X}_\beta/\sqrt{f} + \hat{Y}_\beta$ and compensating the $\hat{X}_\beta/\sqrt{f}$-term in the measurements.

The proposed method was also investigated to its overall uncertainties. Three sources of uncertainty were identified: the measurement equipment, the manufacturing tolerances, and the probing offsets. All of them contribute to the overall uncertainty involved for the method. After investigation by Monte Carlo simulation of different scenarios with 25000 runs each, it can be said that the measurement equipment impacts the overall uncertainty of the measured $Dk$ mainly at lower frequencies up to approximately 20 GHz with a steeply decreasing behavior. The probing offsets and the manufacturing tolerances show significant impact at frequencies above 10 GHz with an approximately linearly increasing behavior up to the maximum frequency of 110 GHz.

The determined $Dk$ with the proposed method shows good agreement to data sheet values and to two other characterization approaches for both investigated substrate materials, Panasonic Megtron 6 and Pyralux TK. The comparison with two other characterization methods was essential as data sheet values are only available up to a very limited frequency range. The proposed method was applied to MS and CBCPW transmission lines and its results were compared with the results of one resonant-method based on ring resonators, and a non-resonant method utilizing substrate integrated waveguides (SIWs). All of the investigated methods lie within a range of approximately $\pm 1\%$ for Megtron 6 and $\pm 1.4\%$ for Pyralux.

# References


[1] L. F. Chen, C. K. Ong, C. P. Neo, V. V. Varadan, and V. K. Varadan, *Microwave Electronics: Measurement and Materials Characterization.* Wiley, 2007.

[2] Eggyal, "Wall mount intercom," 2017 [Online]. Available: https://electronics.stackexchange.com/questions/58310/wiring-a-1920s-intercom-to-a-contemporary-door-entry-phone/. [Accessed: 26-06-2017].

[3] Science Museum / Science & Society Picture Library, "PCB made by eisler in 1942," 2017 [Online]. Available: http://www.ssplprints.com/image/132030/hills-jennie-radio-with-the-first-printed-circuit-board-by-paul-eisler-1942/. [Accessed: 23-06-2017].

[4] G. M. Fasching, *Werkstoffe für die Elektrotechnik.* Springer Vienna, 2005.

[5] E. S. Vera, G. L. Trigg, and W. Greulich, *Combustion to Diamagnetism, Volume 4, Encyclopedia of Applied Physics.* Wiley, 1992.

[6] Farmers Copper, "Copper weathering chart," 2017 [Online]. Available: http://www.farmerscopper.com/blog/coppers-weathering-components/. [Accessed: 12-06-2017].

[7] ARRL, *2014 ARRL Handbook for Radio Communications Softcover.* Amer Radio Relay League, 2013.

[8] B. Bhushan, *Modern Tribology Handbook, Two Volume Set.* CRC Press, 2000.

[9] R. B. Marks, "A multiline method of network analyzer calibration," *IEEE Transactions on Microwave Theory and Techniques*, vol. 39, pp. 1205–1215, Jul. 1991.

[10] M.-Q. Lee and S. Nam, "An accurate broadband measurement of substrate dielectric constant," *IEEE Microwave and Guided Wave Letters*, vol. 6, pp. 168–170, Apr. 1996.

[11] W. R. Eisenstadt and Y. Eo, "S-parameter-based IC interconnect transmission line characterization," *IEEE Transactions on Components, Hybrids and Manufacturing Technology*, vol. 15, pp. 483–490, Aug. 1992.

[12] C. P. Hartwig, D. Masse, and R. A. Pucel, "Frequency dependent behavior of microstrip," in *Proc. G-MTT Int. Microwave Symp*, pp. 110–116, May 1968.

[13] U. Arz, "Microwave substrate loss tangent extraction from coplanar waveguide measurements up to 125 GHz," in *83rd ARFTG Microwave Measurement Conference*, Jun. 2014.

[14] W. Sha, X. Wu, and K. G. Keong, *Electroless Copper and Nickel-Phosphorus Plating*. Elsevier Science, 2011.

[15] D. F. Williams, R. B. Marks, and A. Davidson, "Comparison of on-wafer calibrations," in *Proc. 38th ARFTG Conf. Digest*, vol. 20, pp. 68–81, Dec. 1991.

[16] O. Huber, T. Faseth, H. Arthaber, and E. Schlaffer, "Optimized launching pads for investigating transmission line losses for different surface finishes of RF-pcbs up to 110 GHz," in *Proc. IEEE MTT-S Int. Microwave and RF Conf. (IMaRC)*, pp. 165–168, Dec. 2015.

[17] D. M. Pozar, *Microwave engineering*. Hoboken, NJ, USA: J. Wiley, 3rd ed., 2005.

[18] R. E. Collin, *Foundations for microwave engineering*. New York, USA: IEEE Press, 2nd ed ed., 2001.

[19] J. Coonrod and B. Rautio, "Comparing Microstrip and CPW Performance," *Microwave Journal*, vol. 55, pp. 74–82, Jul. 2012.

[20] O. Huber, T. Faseth, H. Arthaber, and E. Schlaffer, "Characterization of printed circuit board materials and manufacturing technologies for high frequency applications up to 110 GHz," in *Proc. IEEE 16th Annual Wireless and Microwave Technology Conf. (WAMICON)*, pp. 1–4, Apr. 2015.

[21] M. Kirschning and R. H. Jansen, "Accurate model for effective dielectric constant of microstrip with validity up to millimetre-wave frequencies," *Electronics Letters*, vol. 18, pp. 272–273, Mar. 1982.

[22] M. Kobayashi, "A dispersion formula satisfying recent requirements in microstrip CAD," *IEEE Transactions on Microwave Theory and Techniques*, vol. 36, pp. 1246–1250, Aug. 1988.

[23] O. Huber, T. Faseth, G. Magerl, and H. Arthaber, "Dielectric characterization of RF-printed circuit board materials by microstrip transmission lines and conductor-backed coplanar waveguides up to 110 GHz," *IEEE Transactions on Microwave Theory and Techniques*, pp. 1–8, 2017.

[24] C. L. Holloway, E. F. Kuester, A. E. Ruehli, and G. Antonini, "Partial and internal inductance: Two of clayton r. paul 's many passions," *IEEE Transactions on Electromagnetic Compatibility*, vol. 55, pp. 600–613, Aug. 2013.

[25] K. L. Kaiser, *Electromagnetic Compatibility Handbook*. CRC Press, 2004.

[26] T. V. Dinh, B. Cabon, and J. Chilo, "New skin-effect equivalent circuit," *Electronics Letters*, vol. 26, pp. 1582–1584, Sep. 1990.

[27] Joint Committee for Guides in Metrology, "Evaluation of measurement data — guide to the expression of uncertainty in measurement," Sept. 2008.

[28] G. Ghione and C. U. Naldi, "Coplanar waveguides for MMIC applications: Effect of upper shielding, conductor backing, finite-extent ground planes, and line-to-line coupling," *IEEE Transactions on Microwave Theory and Techniques*, vol. 35, pp. 260–267, Mar. 1987.

[29] R. Owens, "Curvature effect in microstrip ring resonators," *Electronics Letters*, vol. 12, no. 14, p. 356, 1976.

[30] D. Deslandes and K. Wu, "Design consideration and performance analysis of substrate integrated waveguide components," in *32nd European Microwave Conference, 2002*, IEEE, oct 2002.

[31] R. Torres-Torres, G. Romo, B. Horine, A. Sachez, and H. Heck, "Full characterization of substrate integrated waveguides from s-parameter measurements," in *2006 IEEE Electrical Performane of Electronic Packaging*, IEEE, oct 2006.

[32] M. Janezic and J. Jargon, "Complex permittivity determination from propagation constant measurements," *IEEE Microwave and Guided Wave Letters*, vol. 9, no. 2, pp. 76–78, 1999.

[33] S. R. Aroor and R. M. Henderson, "Loss performance of planar interconnects on fr-4 up to 67 GHz," *IEEE Transactions on Components, Packaging and Manufacturing Technology*, vol. 3, pp. 2127–2133, Dec. 2013.

[34] M. Cauwe and J. D. Baets, "Broadband material parameter characterization for practical high-speed interconnects on printed circuit board," *IEEE Transactions on Advanced Packaging*, vol. 31, pp. 649–656, Aug. 2008.

[35] G. F. Engen and C. A. Hoer, "Thru-reflect-line: An improved technique for calibrating the dual six-port automatic network analyzer," *IEEE Transactions on Microwave Theory and Techniques*, vol. 27, pp. 987–993, Dec. 1979.

[36] R. H. Jansen, "Unified user-oriented computation of shielded, covered and open planar microwave and millimeter-wave transmission-line characteristics," *IEE Journal on Microwaves, Optics and Acoustics*, vol. 3, pp. 14–22, Jan. 1979.

[37] J. C. Cheng, E. S. Li, W. F. Chou, and K. L. Huang, "Improving the high-frequency performance of coaxial-to-microstrip transitions," *IEEE Transactions on Microwave Theory and Techniques*, vol. 59, pp. 1468–1477, Jun. 2011.

[38] O. Moravek, K. Hoffmann, M. Polivka, and L. Jelinek, "Precise measurement using coaxial-to-microstrip transition through radiation suppression," *IEEE Transactions on Microwave Theory and Techniques*, vol. 61, pp. 2956–2965, Aug. 2013.

[39] D. Staiculescu, J. Laskar, J. Mendelsohn, E. Sweetman, D. Rudy, and I. Anaki, "Ni-au surface finish effects on RF performance," in *Proc. IEEE MTT-S Int. Microwave Symp. Digest (Cat. No.99CH36282)*, vol. 4, pp. 1909–1912 vol.4, Jun. 1999.

[40] D. C. Thompson *et al.*, "Characterization of liquid crystal polymer (lcp) material and transmission lines on lcp substrates from 30 to 110 GHz," *IEEE Transactions on Microwave Theory and Techniques*, vol. 52, pp. 1343–1352, Apr. 2004.

[41] E. Topak, J. Hasch, and T. Zwick, "Compact topside millimeter-wave waveguide-to-microstrip transitions," *IEEE Microwave and Wireless Components Letters*, vol. 23, pp. 641–643, Dec. 2013.

[42] B. C. Wadell, *Transmission line design handbook*. The Artech House microwave library, Boston: Artech House, 1991.

[43] H. A. Wheeler, "Transmission-line properties of a strip on a dielectric sheet on a plane," *IEEE Transactions on Microwave Theory and Techniques*, vol. 25, pp. 631–647, Aug. 1977.

[44] J. Zhang *et al.*, “Reconstruction of dispersive dielectric properties for PCB substrates using a genetic algorithm,” *IEEE Transactions on Electromagnetic Compatibility*, vol. 50, pp. 704–714, Aug. 2008.

[45] Z. Zhou and K. L. Melde, “A comprehensive technique to determine the broadband physically consistent material characteristics of microstrip lines,” *IEEE Transactions on Microwave Theory and Techniques*, vol. 58, pp. 185–194, Jan. 2010.

[46] B. Curran, G. Fotheringham, C. Tschoban, I. Ndip, and K.-D. Lang, “On the modeling, characterization, and analysis of the current distribution in PCB transmission lines with surface finishes,” *IEEE Transactions on Microwave Theory and Techniques*, pp. 1–8, 2016.

[47] Y. Tao and F. Scharf, “Revisiting the effect of nickel characteristics on high-speed interconnect performance,” *IEEE Transactions on Microwave Theory and Techniques*, vol. 64, pp. 2447–2453, aug 2016.

[48] O. Huber, G. Magerl, and H. Arthaber, “Impact of different surface finishes on insertion loss for microstrip resonators up to 110 GHz,” in *2017 IEEE Radio and Antenna Days of the Indian Ocean (RADIO)*, IEEE, sep 2017.

# Appendices

# Appendix Chapter A

# Appendix

## A.1 Derivation of $\beta$ for low loss materials by factor decomposition

In this section a different approach is presented for ending up at the proposed formula of (2.32) that is repeated here as well:

$$Dk_{app} \stackrel{!}{=} \frac{\hat{X}}{\sqrt{f}} + \hat{Y} \tag{A.1}$$

$\mathrm{Dk_{app}}$ has close relation with the imaginary part of the propagation constant $\gamma$ and by utilizing an RLCG-model, it can be expressed as the sum of three factors *I-III* (the frequency dependence is omitted to improve readability):

$$\begin{aligned} Dk_{app} = \left(\frac{\beta}{\beta_0}\right)^2 = \left(\frac{\mathrm{Im}\{\gamma\}}{\beta_0}\right)^2 \\ = \left(\frac{\mathrm{Im}\{\sqrt{(R' + j\omega L')(G' + j\omega C')}\}}{\beta_0}\right)^2 \\ \vdots \end{aligned} \tag{A.2}$$

$$= \frac{c_0^2}{2}\Bigg(\underbrace{\sqrt{\left(\frac{R'G' - \omega^2 L'C'}{\omega^2}\right)^2 + \left(\frac{R'C' + L'G'}{\omega}\right)^2}}_{I}$$

$$\underbrace{-\frac{R'C'}{\omega^2}}_{II} + \underbrace{L'C'}_{III}\Bigg) = \frac{c_0^2}{2}\Big(I + II + III\Big)$$

Inserting Eqns. 2.19a to 2.19d into Eqn. A.2 the factors *I*-*III* can further be evaluated:

$$I^2 = \underbrace{\left(\frac{2}{f_0}\left(\frac{R'_{DC}}{2\pi}\right)^2\left[C'^2 + \left(\frac{k'_G}{2\pi}\right)^2\right] + \frac{k'_G G'_{DC} L'^2_{ext}}{2\pi^2}\right)\frac{1}{f}}_{I_A}$$

$$+ \underbrace{\frac{R'_{DC} L'_{ext}}{\sqrt{f_0}\pi}\left[C'^2 + \left(\frac{k'_G}{2\pi}\right)^2\right]\frac{1}{\sqrt{f}}}_{I_B} \tag{A.3}$$

$$+ \underbrace{L'^2_{ext}\left[C'^2 + \left(\frac{k'_G}{2\pi}\right)^2\right]}_{I_C} + \mathcal{O}\left(\frac{1}{\sqrt{f^3}}\right)$$

$$II = -\frac{R'_{DC}}{(2\pi)^2}\left[\underbrace{k'_G\left(\frac{1}{f} + \frac{1}{\sqrt{f_0 f}}\right)}_{II_A} + \underbrace{G'_{DC}\left(\frac{1}{f^2} + \frac{1}{\sqrt{f_0 f^3}}\right)}_{II_B}\right] \tag{A.4}$$

$$III = \frac{R'_{DC} C'}{2\pi}\left(\frac{1}{f} + \frac{1}{\sqrt{f_0 f}}\right) + C' L'_{ext} \tag{A.5}$$

A frequency constraint with $f \gg f_0$ aids in simplifying the above expressions, as it allows the negligence of $1/f$ in terms $II_A$ and $III$. Term $II_B$ can be disregarded entirely.

For $f \gg f_0$ :

$$II = -\frac{R'_{DC} k'_G}{(2\pi)^2}\frac{1}{\sqrt{f_0 f}} + \mathcal{O}\left(\frac{1}{f}\right) \approx \frac{X_{II}}{\sqrt{f}} \tag{A.6}$$

$$III = \frac{R'_{DC} C'}{2\pi}\frac{1}{\sqrt{f_0 f}} + C' L'_{ext} + \mathcal{O}\left(\frac{1}{f}\right) \approx \frac{X_{III}}{\sqrt{f}} + Y_{III} \tag{A.7}$$

Now terms *II* and *III* comply with Eqn. A.1 by having only a $1/\sqrt{f}$-behavior and a constant term. Expression *I* needs further investigation if a similar frequency behavior can be assumed. A perfect curve progression would occur for:

$$\sqrt{\frac{I_A}{f} + \frac{I_B}{\sqrt{f}} + I_C} \overset{!}{=} \frac{X_I}{\sqrt{f}} + Y_I \tag{A.8}$$

$$\sqrt{\left(\frac{\sqrt{I_A}}{\sqrt{f}} + \frac{I_B}{2\sqrt{I_A}}\right)^2 \underbrace{-\frac{{I_B}^2}{4I_A} + I_C}_{\xi}} = \frac{X_I}{\sqrt{f}} + Y_I \tag{A.9}$$

$$\xi = L'^2_{ext}\left(C'^2 + \left(\frac{k'_G}{2\pi}\right)^2 - \frac{2(\pi R'_{DC})^2\left[C'^2 + \left(\frac{k'_G}{2\pi}\right)^2\right]^2}{k'_G G'_{DC} f_0 (2\pi L'_{ext})^2 + (2\pi R'_{DC})^2\left[C'^2 + \left(\frac{k'_G}{2\pi}\right)^2\right]}\right) \tag{A.10}$$

If $\xi = 0$ the equality holds for several solutions. Even by disregarding the trivial solution $L'_{ext} = 0\,\mathrm{nH/m}$ in the above formulation, there are still four solutions to achieve perfect agreement by solving for $k'_G$:

$$\begin{gathered}\text{if } \xi = 0\\ \Rightarrow X_I = \sqrt{I_A} \text{ and } Y_I = \sqrt{I_C}\\ \text{which is only true for } I_B = 2\sqrt{I_A I_C}\\ \Rightarrow k'_{G_{1,2}} = \pm j2\pi C'\end{gathered} \tag{A.11}$$

$$\begin{gathered}\Rightarrow k'_{G_{3,4}} = -G'_{DC} f_0 \left(\frac{2\pi L'_{ext}}{R'_{DC}}\right)^2\\ \pm\sqrt{(G'_{DC} f_0)^2 \left(\frac{2\pi L'_{ext}}{R'_{DC}}\right)^4 - (2\pi C')^2}\end{gathered} \tag{A.12}$$

Noteworthy is that for negligible $G'_{DC}$ the four solutions are reduced to $k'_{G_{1,2}}$.

As an equality as in Eq. A.8 is unlikely to be achieved in practical examples the following approximation aids in assessing if an $\hat{X}/\sqrt{f} + \hat{Y}$ approximation would still hold:

$$\sqrt{\frac{I_A}{f}+\frac{I_B}{\sqrt{f}}+I_C} \overset{?}{\approx} \frac{\hat{X}_I}{\sqrt{f}}+\hat{Y}_I \tag{A.13}$$

$$\text{for } \frac{2}{f_0}\left(\frac{R'_{DC}}{2\pi}\right)^2\left[C'^2+\left(\frac{k'_G}{2\pi}\right)^2\right] \gg \frac{k'_G G'_{DC} L'^2_{ext}}{2\pi^2} \tag{A.14}$$

$$\Rightarrow I_\delta^2 = \left[\frac{2}{f_0 f}\left(\frac{R'_{DC}}{2\pi}\right)^2+\frac{R'_{DC}L'_{ext}}{\sqrt{f_0 f}\pi}+L'^2_{ext}\right]\underbrace{\left[C'^2+\left(\frac{k'_G}{2\pi}\right)^2\right]}_{I_c} \tag{A.15}$$

The simplification in Eqn. A.14 of $I_A$ in Eqn. A.3 can be assumed for low loss materials to be always satisfied. If a rectangular trace is anticipated, the term $I_\delta^2$ can be evaluated as there are expressions for $R'_{DC}$ and $f_0$ readily available. The "break-point" frequency $f_0$ is represented as $4/(\pi\mu\sigma t^2)$ at which the skin depth equals half of the conductor thickness [26] (with the permeability $\mu$ and the conductivity $\sigma$ of the conductor). In this case $R'_{DC}$ is simply $1/(\sigma w t)$ and $I_\delta^2$ simplifies to dimensional properties of the trace only, except for the external inductance which is tied to the selected transmission line mode:

$$I_\delta^2 \approx \left[\frac{\mu}{8\sigma\pi w^2}\frac{1}{f}+\sqrt{\frac{\mu}{4\pi\sigma}}\frac{L'_{ext}}{w}\frac{1}{\sqrt{f}}+L'^2_{ext}\right] I_c \tag{A.16}$$

If exemplarily a MS line is assumed with a ratio of $u = w/h$ for $10^{-1}\ldots10^{1}$, $L'_{ext}$ varies in between $10^{-6}\ldots10^{-7}\,\mathrm{H/m}$. Furthermore, for a good conductor, a nonmagnetic substrate, and dimensions in the range of millimeters there is only a minute variation around the constant $L'^2_{ext}$ term. Thus, for MS, as well as CBCPW, a linear approximation is valid and $\sqrt{I_A/f+I_B/\sqrt{f}+I_C} \approx \hat{X}_I/\sqrt{f}+\hat{Y}_I$ can be utilized for term $I$ too.

The final result can now be expressed as a linear combination as follows:

$$Dk_{\text{app}} \approx \frac{\hat{X}_I+X_{II}+X_{III}}{\sqrt{f}}+\hat{Y}_I+Y_{III} = \frac{\hat{X}}{\sqrt{f}}+\hat{Y} \tag{A.17}$$

The approximation error $err_{approx}$ for $Dk_{app}$ by focusing on the crucial $1/f$-term, can be estimated by $\Delta$ as follows (with $f \gg f_0$):

$$Dk_{\text{app}} \approx \frac{\hat{X}}{\sqrt{f}} + \hat{Y} + \frac{\Delta}{f} \tag{A.18}$$

$$\Rightarrow err_{approx} = \frac{2\hat{Y}\Delta}{f} + \mathcal{O}\left(\frac{1}{\sqrt{f^3}}\right)$$

$$\Rightarrow \Delta = \frac{R'^2_{DC}}{2L'_{ext}f_0} \tag{A.19}$$

$$\cdot \frac{\frac{1}{\pi}\left[C'^2 + \left(\frac{k'_G}{2\pi}\right)^2\right] + \left(2\pi\left[\sqrt{C'^2 + \left(\frac{k'_G}{2\pi}\right)^2} - C'\right] + k'_G\right)^2}{2\pi\left[\sqrt{C'^2 + \left(\frac{k'_G}{2\pi}\right)^2} - C'\right]}$$

It should be kept in mind that $\Delta$ decreases with $1/f$.

## A.2 Impact of top surface finishes on insertion loss

This section shows the results for an investigation of different top surface finishes applied on MS and CBCPW and ring resonators utilizing the Megtron 6 substrate material. The first investigation of the transmission lines was also published in [16] and the second investigation about resonators in [].

### A.2.1 Transmission lines (MS and CBCPW)

All samples were manufactured with a low $Dk$ material and the MS and CBCPW transmission lines were designed to a 50 Ω wave impedance. The utilized material has a $Dk$ of 3.63 and a loss tangent ($LT$) of 0.004 at 10 GHz, according to the manufacturer's data sheet. The fabrication process is panel plating, whereby the process tolerances for narrow dimensions are stated with ±20%. One board was manufactured twice in the same manner with an ENEPIG-plating for comparison purposes of the manufacturing tolerances. It has to be emphasized that in between the first and the second manufacturing run sufficient time elapsed that the impact of the chemical processes can be assumed to be independent.

#### A.2.1.1 Impact of manufacturing tolerances onto insertion loss

The insertion loss of the two manufacturing runs of samples with the nominally same dimensions are shown in Fig. A.1. In the figure the insertion loss of four MS-

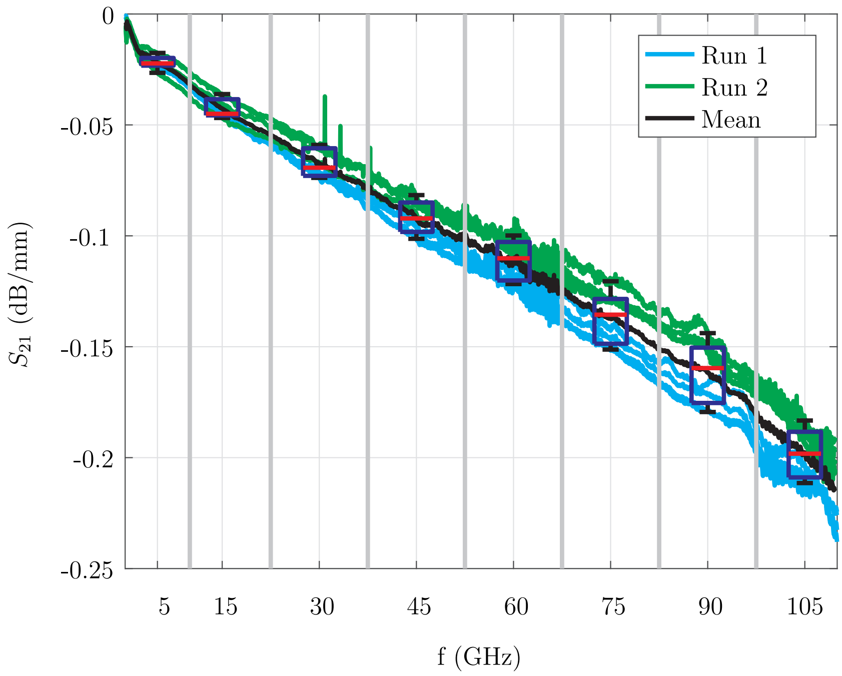


Figure A.1: Manufacturing tolerance analysis

lines, 10, 15, 20, and 25 mm is plotted. Each line measurement was normalized by the respective lengths to show comparable results. Generally, a rather linear behavior over frequency can be observed, however with a crucial loss shift between both manufacturing runs. For further elaboration, the overall is displayed, and box plots are calculated for eight specific frequencies in between 5 and 105 GHz. By evaluating the box plots, a pretty asymmetric probability distribution function is computed. However, the symmetry gets better over frequency, so that for 105 GHz the PDF is roughly symmetric. Not only the shape of the PDF changes but also the width, which indicates a clear trend to higher uncertainties for higher frequencies. The measurements have shown a deviation of approximately −10 % and 14 % in insertion loss for 105 GHz of the overall mean.

#### A.2.1.2 Surface finish analysis for MS and CBCPW

This section describes the measurement results for four different surface finishes, which are ENIG, gold, ENEPIG, and Immersion Tin. It was not possible to fabricate all platings at the same time, therefore, the presented data cannot be compared directly due to process tolerances, as it was shown in the preceding section Sec. A.2.1.1.

Fig. A.2 illustrates $S_{21}$ for ENIG and gold as well as plain copper. For shorter MS-lines, e.g. $l = 5$ mm, the plating has basically no impact at all. However,

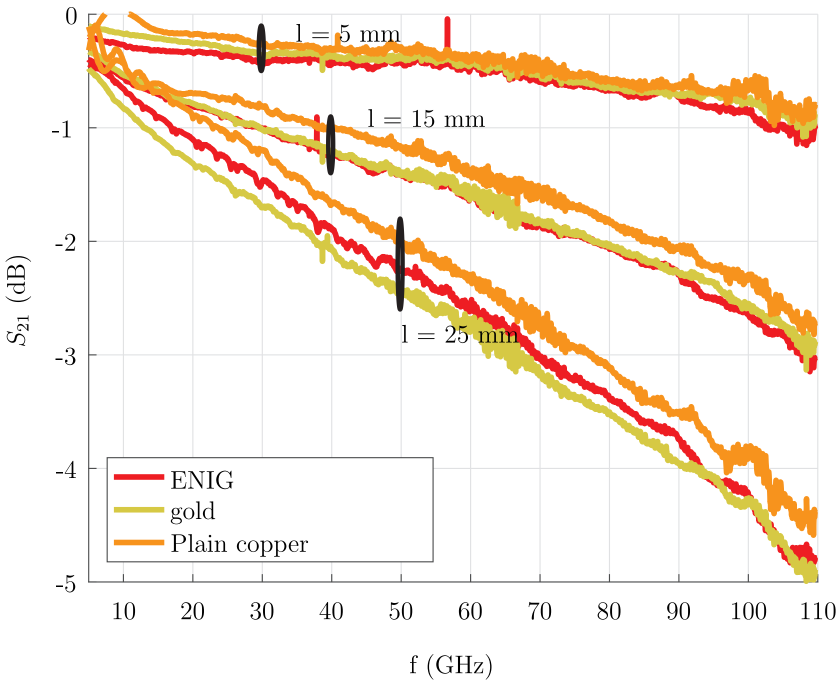


Figure A.2: ENIG, gold, and copper surfaces

for longer lines (e.g. 15 mm and 25 mm), copper features the lowest losses in the investigation. ENIG and gold show similar results. In the plot some degradation effects of copper are already present in the results, as can be seen by contacting problems during conducting the measurements (see plain copper for frequencies up to 20 GHz).

Fig. A.3a and Fig. A.3b displays the insertion loss for ENEPIG and Immersion Tin for MS and CBCPW. For evaluating tolerances of the plating process on the same fabrication panel, two Immersion Tin plated test boards located in close proximity were measured as well. Except for the contacting issues of l = 5 mm with Immersion Tin at position 2 for MS, basically no difference could be noted. It should be noted that these results also apply for the CBCPW transmission line mode (except for some contacting issues of l = 8 mm with Immersion Tin at position 1).

#### A.2.1.3 Conclusion

The investigated platings vary significantly in utilized materials, process characteristics, and price, however, from an RF-perspective no crucial difference could be shown. It was shown that the process tolerances in manufacturing can have more impact on the measured insertion loss than the different plating. The tolerances for two runs of the same nominal dimensions of transmission lines with

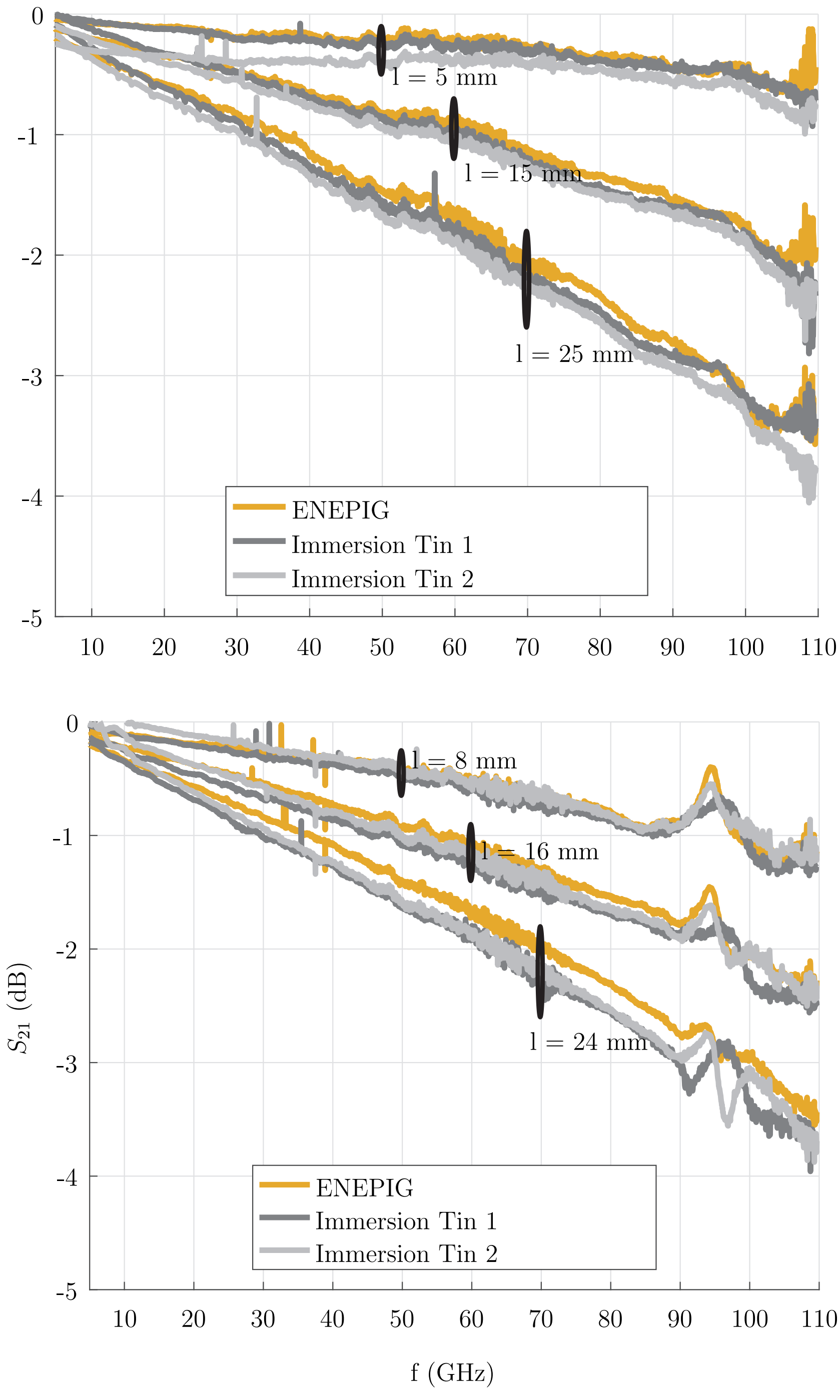


(b) CBCPW

Figure A.3: Immersion Tin position 1 & 2 and ENEPIG for MS and CBCPW

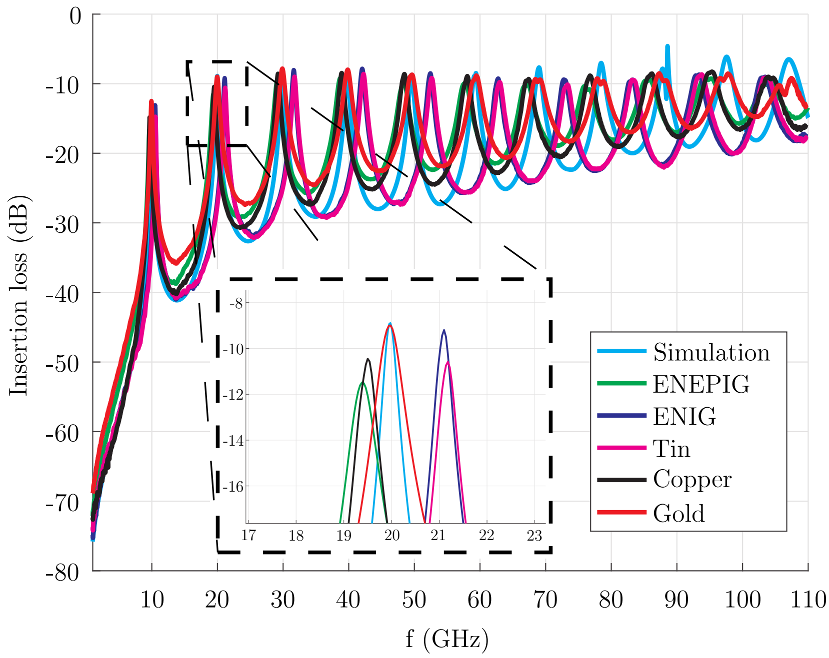


Figure A.4: Insertion loss of 10 GHz MS resonator

the same platings were measured at approximately −10 % and 14 % in insertion loss.

### A.2.2 Microstrip resonators

Fig. A.4 shows measurement results of insertion loss and simulation results of the MS ring resonators with a fundamental resonance at 10 GHz. The simulations were carried out in NI AWR Microwave Office with the conductor being pure copper. For the substrate, data sheet values were taken. The dimensions were determined by microsections. In general, the resonator shows steep resonances with high Q factor up to about 60 GHz. For higher frequencies, the resonator peaks are becoming wider because multiple wavelengths can fit on the circumference of the resonator. The line width for the resonators was designed for 50 Ω, so smaller resonators with higher fundamental frequency were manufactured to overcome this peak widening effect. Fig. A.5 shows the results of the MS ring resonator with a fundamental resonance at 40 GHz. The peak widening is reduced significantly compared to Fig. A.4 for the 80 GHz resonance. The curvature effects were taken into account and compensated for all presented measurement results (see [29]). Please compare for this investigation also the discussion in Sec. 4.3 and in [48].

In Fig. A.4 there is also a magnified plot added to emphasize the differences in insertion loss, in this case at 20 GHz. ENIG and gold show approximately the same attenuation. By adding electroless palladium to the ENIG has a crucial impact on insertion loss. ENEPIG has the worst results of all investigated platings. Tin and the partly oxidized copper same losses and have significantly less loss than the ENEPIG surface finish. Tin has a similar problem like copper that it may corrode over time. Copper has oxidation and deterioration issues. The results are summed up in Tab. A.1. The highest loss difference is measured for ENEPIG and gold at 10 GHz with about 30%. This difference decreases over frequency as more and more current is guided through the top coating that is for both platings gold. At 105 GHz the difference between ENIG and ENEPIG has decreased to $\approx 7\%$.

The simulation shows similar results for lower frequencies, but much lower insertion loss for the upper frequency range in comparison with measurements. Immersion gold platings have typically a thickness of approximately $0.1\,\mu$m. This may be the reason the simulations with pure copper show resembling insertion losses like the gold plating measurements. The reason would be that for lower frequencies a crucial amount of current is propagating in copper and not in the plating. For higher frequencies, a significant amount of current is lead through the surface finish, which maximizes especially close to the coupling gap. The coupling gap is geometrically only a small area, wherein the lower conductivity of the plating compared occurs. However, it still shows a crucial impact in the overall insertion loss. In a former investigation [16], it was shown that the plating has negligible impact on the MS lines. This means that the feed and the resonator should have negligible impact on the difference in insertion loss for the ring resonators.

Table A.1: Measurement results

| **Surface finish** | **frequency (GHz)** | | | | | | | | | |
|---|---|---|---|---|---|---|---|---|---|---|
| | 10 | 20 | 30 | 40 | 50 | 60 | 70 | 80 | 90 | 100 |
| Simulation | -12.7 | -9 | -8 | -8.1 | -8.7 | -8.6 | -7.7 | -7.1 | -6.8 | -6.2 |
| ENEPIG | -16.6 | -11.5 | -9.6 | -9.2 | -9.6 | -9.9 | -10 | -10.4 | -9.4 | -9.1 |
| ENIG | -13.1 | -9.2 | -8 | -7.9 | -8.5 | -9.3 | -9.4 | -9.4 | -8.7 | -9.1 |
| Tin | -14.7 | -10.6 | -9 | -8.6 | -9.2 | -9.8 | -10.1 | -9.5 | -8.7 | -9 |
| Copper | -14.8 | -10.5 | -8.6 | -8.5 | -8.6 | -8.9 | -9.3 | -8.8 | -8.3 | -8.3 |
| Gold | -12.5 | -9 | -7.9 | -8 | -8.7 | -8.8 | -9.3 | -9.25 | -8.5 | -8.5 |

### A.2.3 Conclusion

For the investigated platings it was shown that there are significant impacts on insertion loss for resonant structures, as in this case ring resonators. For the wide range of investigated surface platings, the results showed negligible differences on

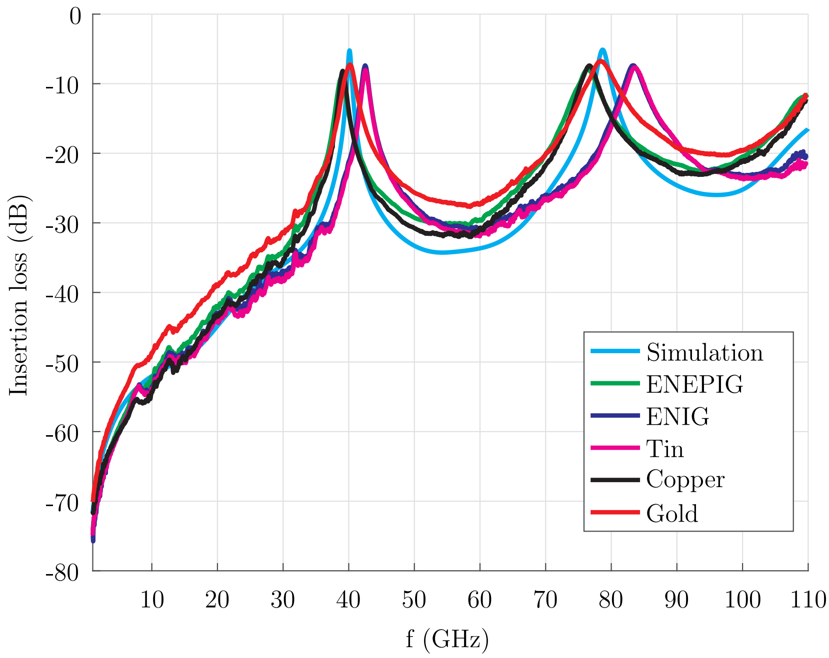


Figure A.5: Insertion loss of 40 GHz MS resonator

insertion loss comparing gold and ENIG plating for frequencies up to 110 GHz. However, the price varies significantly in between these two finishes. The widely used ENEPIG plating shows crucially more losses compared with gold or ENIG at lower frequencies, i.e. ≈ 33% at 10 GHz. For higher frequencies, a diminishing impact of this behavior was measured, e.g. only ≈ 7% at approximately 100 GHz.